UNIVERSITEIT VAN PRETORIA
UNIVERSITY OF PRETORIA
YUNIBESITHI YA PRETORIA

Self-assembled mycolic acid antigens on gold electrode as an impedimetric immunosensing platform for active tuberculosis

by

Nsovo Samuel Mathebula

Submitted in fulfilment of the requirements for the degree of

Master of Science (Chemistry)

In the Faculty of Natural and Agricultural Sciences,

University of Pretoria

November 2009

Supervisor: Dr K I Ozoemena

Co-supervisor: Prof J A Verschoor

DECLARATION

I declare that the Thesis/Dissertation, which I here by submit for the degree MSc (Chemistry) at the University of Pretoria, is my own work and has not previously been submitted by me for a degree at this or any other tertiary institution.

SIGNATURE:

DATE:

DEDICATION

I would like to dedicate this Thesis to my parents, Sarah Basani and Selby Shirilele Mathebula, for their invaluable support throughout the long and difficult, but rewarding journey.

ACKNOWLEDGEMENTS

I would like to express my sincere appreciation and gratitude to the following people and Institutions. Special thanks goes to my promoter, Dr Kenneth Ozoemena for his assistance, understanding, immense dedication and encouragement throughout my studies. My co-promoter, Prof Jan Verschoor, for his expert opinion in Tuberculosis diagnosis. Dr Gianna Toschi, for believing in me and always willing to assist with anything about the project. Prof T. Von Moltke for giving me access to the XPS equipment as well as assist me in interpreting the results. Fellow students at Chemistry and Biochemistry for team work. The National Research Foundation of South Africa for the financial support and the University of Pretoria for the time given to me to finish my studies.

Abstract

Tuberculosis (TB) is well recognized as one of the most life-threatening infectious diseases in the world with about 2 million deaths and 8 million new cases per year. It is also the major cause of death in Human Immunodeficiency Virus/ Acquired Immune Deficiency Syndrome (HIV/AIDS) co-infected individuals, for whom no fast, affordable accurate TB test is available. There is therefore an urgent need for the rapid diagnosis of TB especially in Sub-Saharan Africa where the population is most burdened by the HIV/AIDS pandemic. In this study, an electrochemical impedimetric immunoassay of TB is proposed that is based on the detection of surrogate marker anti- mycolic acid (MA) antibodies that was previously shown not to be affected by patients co-infected with human immunodeficiency virus (HIV). It uses mycolic acid (MA) antigens integrated into a self-assembled monolayer (SAM) of N-(2-mercaptoethyl) octadecanamide (MEODA) on a gold electrode (Au). The integrity and properties of the Au-MEODA-MA layer were first investigated using cyclic voltammetry (CV) and electrochemical impedance spectroscopy (EIS). EIS data showed that Au-MEODA and Au-MEODA-MA behave as microelectrode arrays, with pinholes acting as the microelectrodes that permit electron transport between a redox-active probe in solution and the underlying gold surface. The average radii of the pinholes (r_a) and half the distance between the centres of the neighbouring pinholes

(r_b), were estimated from EIS using the pore size model and discussed. Anti-MA antibodies present in a patient with active tuberculosis strongly interacted with Au-MEODA-MA showing a quite compact and stable bio-complex structure that is virtually defect-free. The electrochemical impedimetric properties associated with the ability of the Au-MEODA-MA to discriminate between TB positive and negative human sera are also discussed. This thesis proves that the Au-MEODA and Au-MEODA-MA electrodes, as well as the MA–anti-MA antibody interactions, are characterized with time-constant dispersion occurring mainly along the area of the electrode (2-D distribution) with some contributions from the axis normal to the plane of the electrode surface (3-D distribution), typical of microstructures with grain/grain boundary phases. These crucial physico-electrochemical insights into the behaviour of surface-confined MA-antibody complexes could provide a useful basis for the design and development of potential impedimetric immunosensors for the diagnosis of active tuberculosis.

Table of contents

List of Figures and Tables

List of Abbreviations

A	Area of the electrode surface in cm3
AE	Azide EDTA
AFM	Atomic force microscopy
Ag	Silver

AgCI	Silver chloride
AIDS	Acquired immune deficiency syndrome
Au	Gold
Au-S	Gold bound sulfur
C_{dl}	Double layer capacitance
	Characterisation of the clean bare gold for use in an equation
CFM	Chemical force microscopy
c_o	Concentration in mol cm^{-3}
-COOH	Carboxylic acid
CPC	Cetyl pyridinium chloride
CPE	Constant phase element
CV	Cyclic voltammetry
D_o	Diffusion coefficient
D	Diffusion coefficient of the Redox couple
dc	Direct current
DCC	Dicyclohexylcarbodiimide
DMF	Dimethylformamide
E	Potential

E^0	Standard reduction potential
E_{pc} - E_{pa}	Positions of peak voltage at the anode and cathode
EDTA	Ethylenediaminetetraacetic acid
EIS	Electrochemical impedance Spectroscopy
ELISA	Enzyme linked immunosorbent assay
f	Faraday constant (96.485 C/equiv)
H_2SO_4	Sulphuric acid
H37Rv	American type culture collection 27294
HAART	Highly active anti-retroviral therapy
HIV	Human immunodeficiency virus
I	Resulting current
I/A	Current in amperes
i_p	Peak current in amps
i_{pa} and i_{pc}	Positions of peak currents of voltage at the anode and cathode
IAsys	Interaction analysis system
IRIS	Immune reconstitution inflammatory

	syndrome
$K_3Fe(CN)_6$	Potassium ferrocyanide
$K_4Fe(CN)_6$	Potassium ferricyanide
K_{app}	Apparent electron Transfer rate
KCl	Potassium chloride
k_{et}	Electrode-solution interface
KH_2PO_4	Answer potassium dihydrogen
K—K	Krame Kronig
k^o	Heterogeneous electron transfer
k_o	Rate of reaction
m	*Slope*
M. tuberculosis	*Mycobacterium tuberculosis*
MA	Mycolic acid
MEODA	N-(2-mercaptoethyl) octadecanamide
MTB	*Mycobacterium tuberculosis*
n	Number of electrons transferred
Na_2HPO_4	Sodium phosphate
NaN_3	Sodium azide
NaOH	Sodium hydroxide

O	New material; due to oxidation
pa	Peak anode
PBS	Phosphate buffer saline
pc	Peak cathode
PC	Phosphatidylcholine
PCR	Polymerase chain reaction
PO_4	Phosphate
PPD	Purified protein derivative
q	Transition radial frequency
Q	Frequency independent constant
R	Molar gas constant (8.314 J mol $^{-1}$)
R_{Ag}	Electrode polarization resistance
R_{ct}	Charge transfer resistance
R^{AuE}_{ct}	Charge transfer resistance of the bare gold substrate
R_s	Electrolyte resistance
R^{SAM}_{ct}	Charge transfer resistance of a self assembled monolayer modified substrate

R_p	Polarization resistance
Sam	Self-Assembled Monolayer
T	Absolute temperature in Kelvin
t	Time
TB	Tuberculosis
TDM	Trehalose Dimycolate
TOA	Take Off Angle
w	Radial Frequency
W	Warburg coefficient
WHO	World health organization
XPS	X—ray photoelectron spectroscopy
Z	impedance
ZCPE	Impedance of Constant Phase Element
Z_w	Warburg Impedance

List of symbols

α	Transfer coefficient
ΔE	Voltage separation between the currents
σW	Warburg Coefficient calculated from the anodic and cathodic peaks respectively between the voltage and the current
r_a	Radius of the pinholes
r_b	Half the distance between the centers of two adjacent pinholes
v	scan rate in Vs^{-1}
β	Electron tunnelling coefficient
Ω	Ohms
Θ	Time lag
Θ^{p}_{IS} or Θ^{R}_{IS}	Fractional surface coverage

Chapter 1

Introduction

1.1 A General Overview of Thesis

Tuberculosis (TB) is well recognized as one of the most life-threatening infectious diseases in the world with 2 million deaths and 8 million new cases per year [1]. TB is the major cause of death in HIV/AIDS co-infected individuals [2]. It has been estimated that a delay in the diagnosis and treatment of TB of more than three weeks after its presentation is the cause of 45 to 85% of deaths of TB/HIV co-infected patients [3]. There is therefore an urgent need for new surrogate markers for the rapid diagnosis of TB especially in Sub-Saharan Africa where the population is most burdened by the HIV/AIDS pandemic.

Mycolic acids have been shown with enzyme-linked immunosorbent assay (ELISA) [4] and optical biosensor [5] to be promising mycobacterial antigens in serodiagnosis of active pulmonary TB in HIV infected populations. However, these methods are still in need of optimization to improve accuracy and reliability before they can be tried for any clinical application. A strategy proposed in this thesis is an electrochemical technique known as *"electrochemical impedance spectroscopy (EIS)"* using as a working electrode (sensor) a gold disc electrode modified with a self-assembled monolayer (SAM) of long chain alkanethiolate (N-(2-mercaptoethyl) octadecanamide) (MEODA) incorporating mycolic acids as the active antigens for the recognition of anti-mycolic acid antibodies in

human serum from TB patients co-infected with human immunodeficiency virus (HIV).

Aim of thesis

(i) To modify bare gold electrode with a self-assembled monolayer of an alkanethiolate incorporating mycolic acid (MA) antigens (Au-MEODA-MA) for use in a TB sensor;

(ii) To evaluate the integrity and properties of the Au-MEODA-MA using cyclic voltammetry (CV) and electrochemical impedance spectroscopy (EIS);

(iii) To establish, using CV and EIS, the ability of SAM-confined MA antigens to discriminate between a TB-positive and a TB-negative serum.

This introduction chapter will provide an overview of tuberculosis and its impact on society, the causative agent of TB, *Mycobacterium tuberculosis* (*MTB*), mycolic acids and their potential role in the strategies for serodiagnosis of TB, overview of electrochemistry (notably cyclic voltammetry and electrochemical impedance spectroscopy) as well as microscopic techniques used in characterising Self Assembled Monolayers (SAMs). In chapter 2 the experimental procedures used in this project are discussed. Chapter three is a discussion of the results obtained.

1.2 An Overview of Tuberculosis and Its Impact on Society

Tuberculosis (TB) is an infectious disease mostly caused by *Mycobacterium tuberculosis* (MTB), and rarely caused by *Mycobacterium bovis* and *Mycobacterium africanum.* MTB infection occurs when individuals inhale bacteria aerosolized by persons already infected. Upon inhalation the bacilli are deposited into the distal respiratory alveoli. Subsequently the alveolar macrophages phagocytose the inhaled bacilli. However, if these macrophages are unable to kill the mycobacterium, the bacilli continue to multiply unimpeded [6]. MTB is slow growing and tolerates the intracellular host environment; thus it can remain metabolically inert for a long time before reactivation and disease.

TB is a major health problem affecting one-third of the world population, of which approximately 8 to 9 million people develop it and approximately 2 million people are killed annually as reported by the World Health Organization (WHO) [1,2], making it the leading cause of death from a single infectious agent [7]. In the last decade there has been a rise in the incidences of TB due to co-infection with HIV [8], because HIV decreases immune control of latent MTB infection; thus greatly increasing the risk of reactivation of the latent to active disease [9]. In addition the emergence of drug resistant and multiple drug resistant TB has been on the rise even in developed countries [10], due to co-infection with HIV.

The ability to accurately diagnose TB in HIV co-infected patients depends on the stage of HIV infection and the associated degree of immunodeficiency. In early HIV, MTB infection with mild to moderate immunodeficiency has features that have characteristics of post-primary TB because of reactivation or re-infection, while in more advanced immunodeficiency the features are associated with an increased frequency of pulmonary disease, similar to both primary pulmonary and extrapulmonary TB [11]. It is therefore easier to diagnose TB at an early stage, since there is a higher proportion of patients with sputum smear-positive pulmonary TB than in later HIV infection.

It has been estimated that a delay in the diagnosis and treatment of TB of more than three weeks after its presentation is the cause of 45 to 85% of deaths of HIV patients [3]. Furthermore the treatment of HIV patients, who are co-infected with TB, with highly active anti-retroviral therapy (HAART) could result in the triggering of an inflammatory reaction, causing immune reconstitution inflammatory syndrome (IRIS)[12]. IRIS occurs within the first few weeks after the commencement of therapy when an undiagnosed latent or sub-clinical infection was present at baseline.

Since TB is not easily diagnosed in HIV co-infected TB patients, there is a need for an accurate, rapid, sensitive, simple and cost effective test that can diagnose TB even in HIV infected patients.

1.2.1 Mycobacterium tuberculosis

Mycobacterium tuberculosis (figure 1.1) is an aerobic, gram positive, non-spore forming, non-motile, and slow growing bacillus with a curved and beaded rod-shaped morphology, that can survive under adverse environmental conditions due to its hardiness [13]. The cell wall of MTB is extremely hydrophobic and forms an exceptionally strong permeability barrier rendering it naturally resistant to a wide variety of antimicrobial agents. It is composed mainly of three layers, namely; peptidoglycan complex, arabinogalactan complex and mycolic acids. The peptidoglycan layer is linked to arabinogalactan (D-arabinose and D-galactose) which is then linked to high-molecular weight mycolic acids. The arabinogalactan-mycolic acid layer is overlaid with a layer of polypeptides and mycolic acids consisting of free lipids, glycolipids, and peptidoglycolipids. Like the outer membrane of the gram-negative cell wall, porins are required to transport small hydrophilic molecules through the outer membrane of the acid-fast cell wall. The lipids of the MTB cell envelope are unique in composition [14] and are associated with mycobacterium virulence.

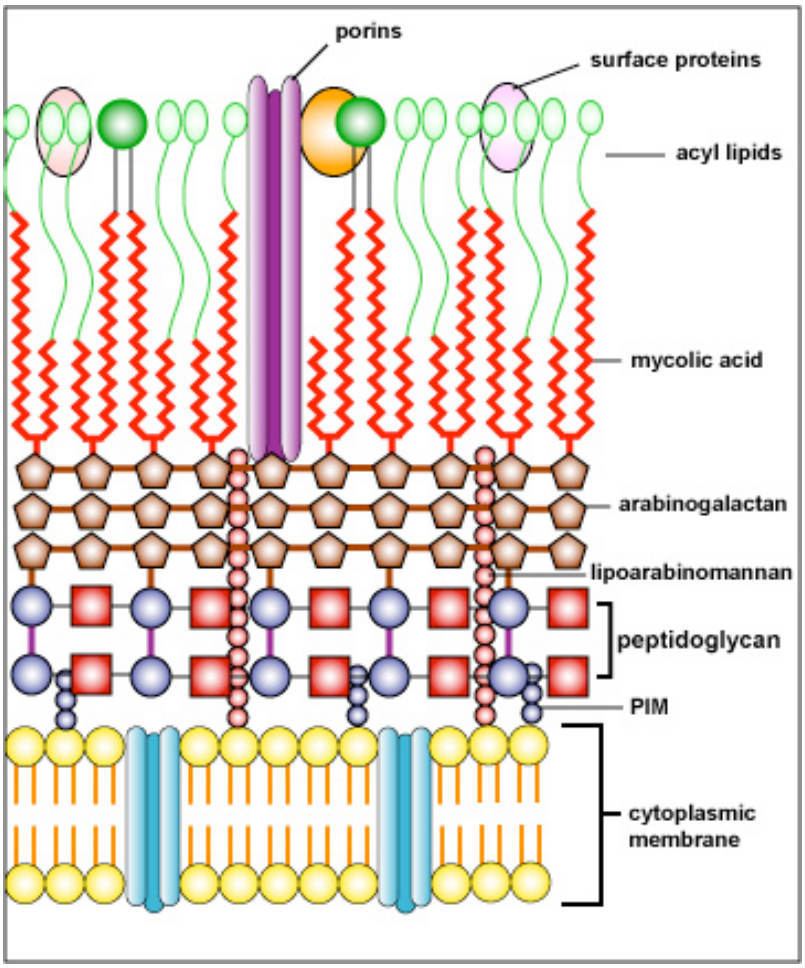

Figure 1.1: A model structure of the cell wall of the MTB [15].

1.2.2 Mycolic acid structure

Mycolic acids are very long chain (C_{60}-C_{90}), high molecular weight alpha-alkyl-beta-hydroxyl fatty acids comprising about 30% of the dry weight of MTB [16]. They are the major lipid constituent of the MTB envelope, responsible for resistance to drugs and to oxidative stress [17, 18]. They exist in the MTB cell envelope mainly covalently bound to the cell wall

peptidoglycan via the arabinogalactan (figure 1.1 and 1.3), but also as cord factor, consisting of trehalose dimycolate (TDM) [19 – 21].

Mycolic acids consist of two characteristic parts, namely the long fatty part called the meromycolate chain and the saturated carboxylic part called the mycolic motif [22] (figure 1.2). The meromycolate chain from pathogenic mycobacteria varies in nature of the functional groups in the meromycolate chain and the different spacing between these groups. On the basis of these differences on the functional groups on the meromycolate chain, mycolic acids are divided into subclasses (figure 1.2) [22]. In *MTB,* these are alpha-, keto- and methoxy- MA.

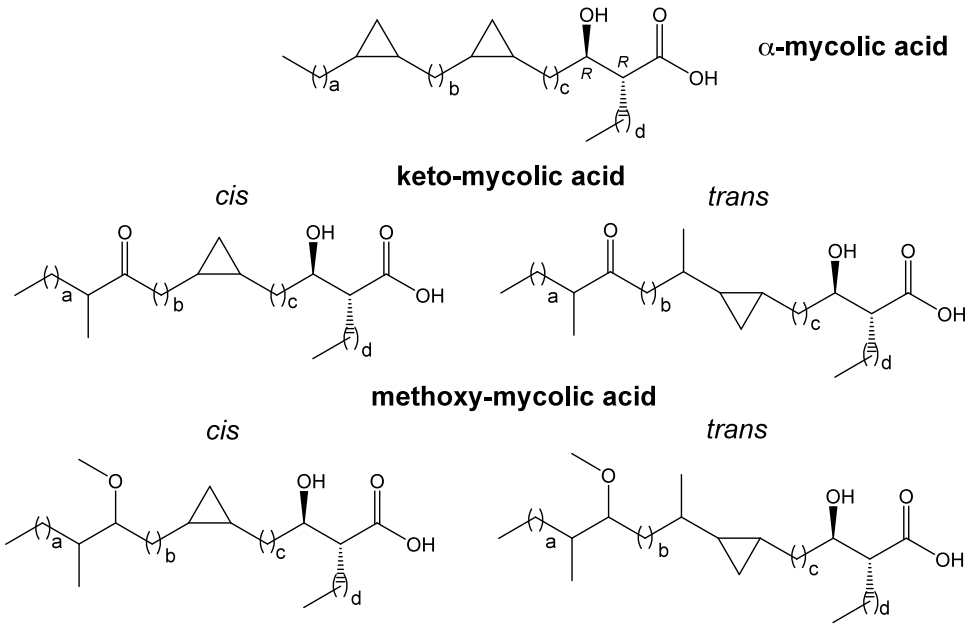

Figure 1.2: Structural formula of mycolic acids subclasses from *M. tuberculosis*. The letters a (15-19), b (10-16), c (11-21), d (21 or 23) depicts the inter-chain lengths, which vary within and amongst mycolic acid of different mycobacterial species.

Mycolic acids from MTB are categorized into three structural classes (figure1.2), namely: alpha-whose mero-chain contains no oxygen, methoxy- and ketomycolate whose distal group has either a methoxy or a keto group respectively and both have methyl branches next to the oxygenated functional groups. None of these subclasses is characteristic only of *Mycobacterium tuberculosis,* they are all present in other organisms some of which are pathogenic while others are non-pathogenic mycobacteria. The alphamycolate, which is not oxygenated, is the most widely distributed among other mycobacteria. Ketomycolate is the most widely distributed of the two oxygenated mycolates and occurs in various combinations with the alphamycolate, whereas the methoxymycolate always occur in combination with the ketomycolate [21]. The mycolic acid chains are arranged parallel to each other and perpendicular to the plane of the cell envelop (figure 1.3) [23- 25].

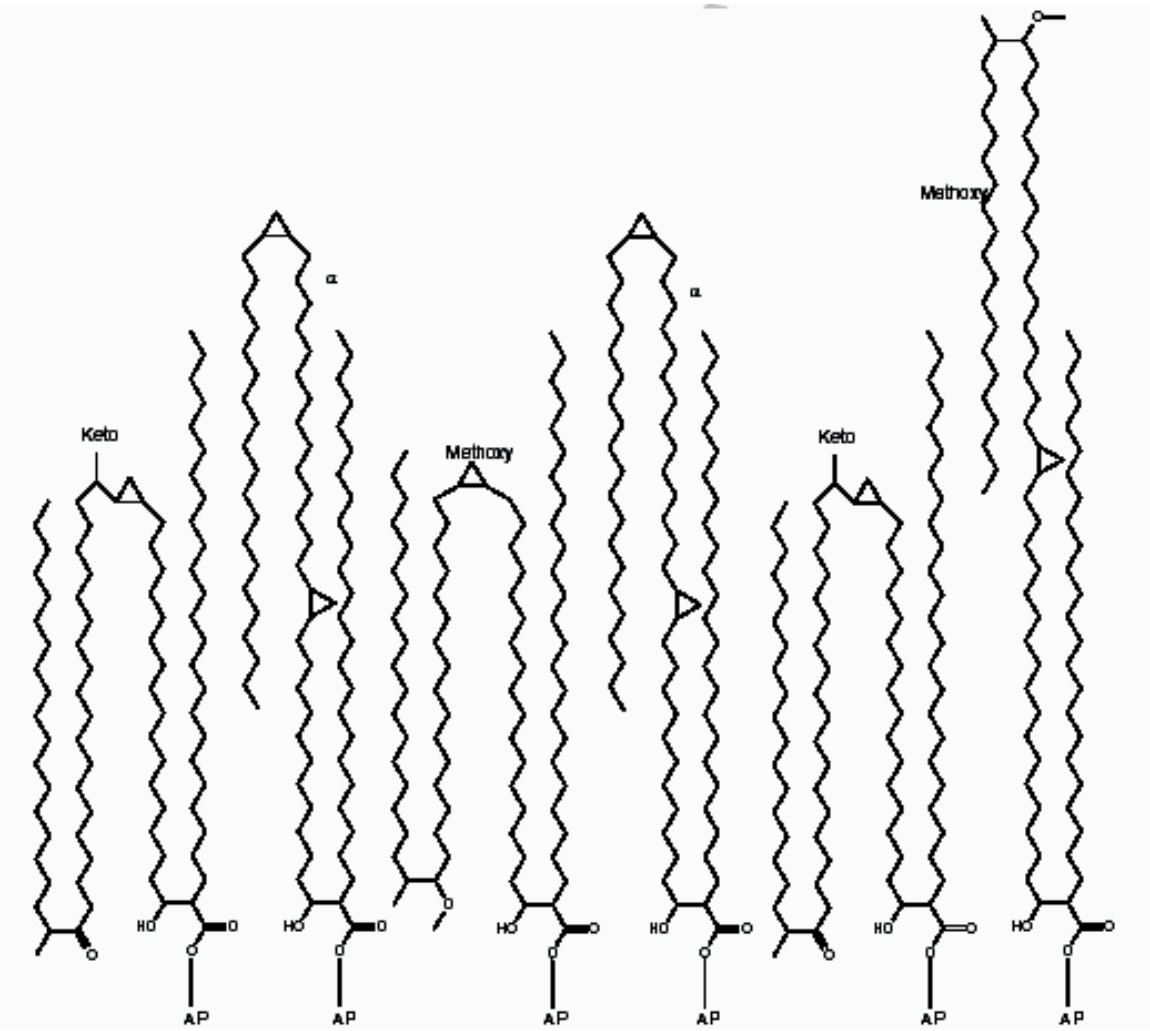

Figure 1.3: Structure showing the possible arrangement of the mycolic acid [37].

1.3 Methods of Diagnosis of Tuberculosis

In the last decade there has been a rise in the incidences of TB due to co-infection with HIV [8]. Currently, available methods for the diagnosis of TB are not effective in HIV burdened populations. These methods include:

i. **Culture method**. Culture analysis of sputum is the gold standard for TB detection. It usually takes 4-8 weeks for completion of analysis [38], leading to delayed diagnosis, patient care and TB control.

ii. **Sputum microscopic methods and lung X-rays.** These tests are the routinely employed methods of TB diagnosis. They are not effective in TB-HIV co-infected patients, because these patients often produce limited numbers of mycobacterial colony-forming units in sputum [28] and less radiographic evidence of pulmonary disease [37].

iii. **DNA and RNA amplification.** Nucleic acid-based polymerase chain reaction (PCR) technology has also been described for testing TB. However, PCR-based assay is laborious, and some components of the specimen and chemicals demand selective enrichment of cells, which may cause inhibitory effects, thus negatively impacting on the efficiency of the PCR [32] These methods cannot distinguish between live and/or dead bacteria, thus can not be used for patients receiving treatment and for extra-pulmonary TB cases, [32].

iv. **The purified protein derivative (PPD) skin test**. Although used throughout the world, it is not optimal in terms of both specificity and sensitivity. The low specificity is due to the PPD which contains proteins extensively common among mycobacteria. It cannot

distinguish from previous BCG vaccination, latent TB, active TB or infection by other mycobacteria other than *Mycobacteria tuberculosis* [33, 34]. The sensitivity of the skin test is substantially reduced in TB-HIV co-infected patients.

Although the lungs are the primary site of disease in approximately 84% of TB positive-HIV negative patients, it has been estimated that half of the TB-HIV positive co-infected patients have extra-pulmonary TB [27, 29]. The diagnosis of extra-pulmonary TB is often difficult even when using standard methods, because the mycobacteria can be present in low numbers at inaccessible sites [28]. In addition to the practical criteria such as sensitivity, specificity, speed, reproducibility and being able to diagnose TB even in HIV infected patients; a TB diagnostic test should also be able to deal with accompanying complications such as latent tuberculosis and extrapulmonary tuberculosis, which can subsequently develop into an active disease.

1.3.1 Mycolic acids in serodiagnosis of tuberculosis

Serodiagnosis is an immunological method which does not require specimen from the site of infection, but measures humoral and cellular responses of the host to detect the presence of infection and disease. Technically, serological tests can be uncomplicated, rapid and relatively inexpensive

depending on the technique used [35]. Interestingly, since serological tests do not require a specimen from the site of infection, they are able to detect extra-pulmonary tuberculosis [35, 26]. Unfortunately serodianostic assays for TB have generally shown suboptimal results, including inadequate sensitivity and specificity when compared to culture method [4, 5] Importantly due to the increase in the incidences of TB-HIV co-infected cases [31], it is clear why interests in serodiagnosis remain high, more especially in extra-pulmonary TB cases [26′ 30].

It has been reported that anti-mycolic acid antibodies are elevated in TB infected patients [39, 40]. Schleicher *et al.* [4] showed with ELISA that the anti-MA antibody binding signal is not affected by the stage of HIV infection. Regrettably, one of the factors that conspire against the use of free MA in this serodiagnostic ELISA of TB is low accuracy (57%) [4], which doesn't meet the required level as stated by the WHO. These low accuracies have been reported in most ELISA based serodiagnosis [36]. Moreover, ELISA assay requires extra enzyme-labelled antibodies and intense sample clean-up to operate, thus restricting its application for on-site testing.

Verschoor's research group has demonstrated that serodiagnosis of TB using antibodies to free mycolic acid as surrogate markers with an optical biosensor has great potential for solving the TB diagnosis problem. This was shown using an Interaction Analysis system (IAsys) biosensor, which is a double channel system that is based on wave-guide technology [**5**]. The

technique involves activating the cuvette's surface with cetyl pyridinium chloride (CPC). Mycolic acids encapsulated in liposomes are then immobolised on the CPC activated surface. The surface is then blocked with saponin to prevent non-specific binding of antibodies. To diagnose a patient as TB positive or negative, an antibody-antigen interaction study is performed using the patient's serum. This is achieved by first adding a high dilution of serum in PBS/AE in both the cells in order to compare the response of the two cells. A solution containing pre-incubated lower dilution of serum in either liposomes containing mycolic acid or empty liposomes is then added at room temperature in the two cells. The degree to which the antibody binding signal is inhibited by means of pre-incubation with MA-liposomes, relates to the amount of anti-MA antibodies in the sample and thus toTB. Unfortunately the accuracy of this serodiagnosis test (85%) [5], although significantly better than that observed when using ELISA, does not fall within the required % accuracy as stipulated by WHO for a serodiagnostic assay.

As already stated, for the first time, this thesis is aimed at employing electrochemical strategy in the serodiagnosis of TB by using antibodies to free mycolic acid as surrogate markers. The next section gives a broad overview of electrochemical techniques employed in this thesis.

1.4 Electrochemistry: A Brief Overview

Electrochemistry is defined as the study of chemical reactions to produce electric power or the use of electricity to effect chemical processes [47]. It is the study of electron transfer processes, i.e. redox reactions that accompany the passages of current. It is the electrons performing an electrochemical reaction that are used for electro-analysis. These electrons are transferred away from the electro-active probe in solution through the phase boundary that separates the electrode and the solution containing the electro-active probe to the electrode during oxidation. During reduction this process is reversed (figure 1.4).

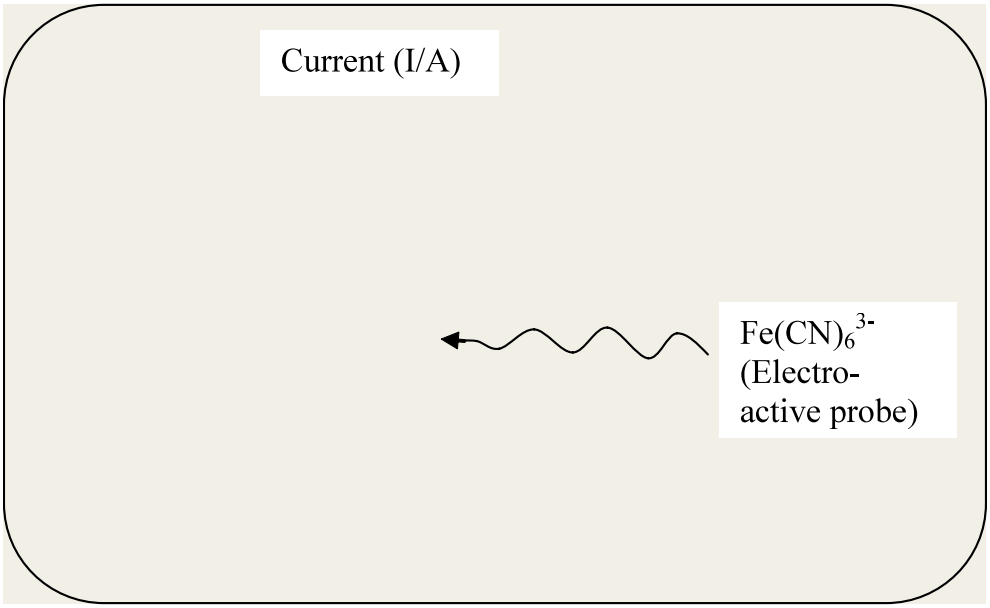

Figure 1.4: A schematic diagram showing the process of electro-analysis.

The rate of this electron transfer to and/or from the electrode is dependent on the electronic conductivity of the material used to craft the electrode. Solid electrodes based on metal materials, such as gold, platinum, silver and copper, are currently the most extensively used in electro-analysis. This is owed to their broad potential window, low background current, rich surface chemistry, low fabrication cost and applicability to a wide range of sensing and detection applications [41]. One of the rate limiting steps during electro-analysis is the rate of the electron movement across the electrode-solution interface ($\mathbf{k_{et}}$), which is directly proportional to the experimental electrode potential. The other rate limiting step during electro-analysis is the mode at which the electro-active probe moves from the solution to approach close enough to the electrode for electron transfer to occur. There are three ways in which the electron from the electro-active probe moves, namely:

(i) Migration. This is the movement in response to an electric field. Its rate depends on the charge on the ion, the size of the ion and the strength of the interaction between the ion and the field [47]. A stronger field will form at an electrode bearing a larger potential (i.e. a more negatively or positively charged electrode). Thus it is very important to note that migration will not occur if the electrode has no potential. The effect of a migration can be minimised if a liquid electrolyte like aqueous un-reactive ionic salt solution (e.g. KCl and KNO_3) is employed, which contains an approximately 100 times excess

concentration of electrolyte other than that of the electro-active probe. This excess un-reactive, so-called swamping electrolyte induces the phenomenon of electrode polarisation, with a build-up of oppositely charged electrolyte ions at the electrode solution interface.

(ii) **Convection.** The charged particles from the electro-active probe can move as a result of the physical movement of the solution in which the electro-active probe is dissolved. This mode of ions movement is called convection. This can occur due to mechanical stirring, or it can be induced when the amount of charge passed through an electrode creates localized heating of the contact solution with concomitant convective stirring, because the density of the solvent decreases with an increase in temperature. The degree of convection can be minimised by not stirring the solution of the electro-active probe and by avoiding physical disturbance that will cause movement of the solution.

(iii) **Diffusion.** This is simply the flux of the electro-active probe which is in direct proportion to the change in concentration of the electro-active probe as a function of the distance away from the electrode surface [47].

Electrochemical techniques are popular choices in analytical biosensing because of their ability to deliver targeted information such as the distribution of defects, properties of the linked redox probe, the kinetics and

mechanistic information about the monolayer formation processes and surface coverage in a fast, simple and cost effective manner [42-45].

The advantages of electrochemical techniques over other analytical techniques such as ELISA include:

i. A high sensitivity with a very large useful concentration range for both organic and inorganic application;

ii. Large variety of useful solvents and the electrolyte/probing species;

iii. A wide range of temperatures;

iv. Rapid analysis time;

v. Offers the ability to determine kinetic and mechanistic parameters;

vi. Well developed theory which offers the probability of estimating the values of unknown parameters; and simultaneous determination of several analysts.

Some of the common disadvantages of electrochemical techniques, are that the electro-active probe used must be able to undergo reduction or oxidation in the range were the solvent and the electrode remain electrochemically inert, samples must be dissolved first and the technique provides very little or no information on the identity of the binding species.

There are many different types of electrochemical techniques. For this study only cyclic voltammetry (CV) and electrochemical impedance spectroscopy (EIS) were used and will be discussed.

1.4.1 Cyclic voltammetry (CV)

Cyclic Voltammetry is the most popular electrochemical technique. Like all voltammetric techniques, CV involves the application of a potential (E) to an electrode and the monitoring of the resulting current (*i*) flowing through the electrochemical cell. In most cases the E is varied or *i* is monitored over a period of time (*t*). Voltammetric techniques are said to be electro-active techniques because the applied potential forces a change in the concentration of the electro-active probe at the electrode surface by electrochemically reducing or oxidizing it. The reduction or oxidation of a substance at the surface of the working electrode at the appropriate applied potential, results in the mass transport of new material to the electrode surface and the generation of a current.

The applied potential controls the concentration of the electro-active (redox) species at the electrode surface and the rate of the reaction (k_o), as described by the Nernst and Butler-Volmer equations, respectively. In the case where the mode of electron movement in solution is through diffusion, then the resulting current from the redox process (faradaic current) is

related to the material flux at the electrode-solution interface- Fick's law. In a reversible electrochemical reaction (O + ne^- ↔ R), the application of a potential (E) forces the respective concentrations of the species in the anode (O) and cathode (R) at the surface of the electrode to a ratio in compliance with the Nernst equation;

$$E = E^0 - \frac{RT}{nF} In \frac{c_R^0}{c_O^0} \qquad 1.1$$

where *R* is the molar gas constant (8.314 *J* mol^{-1} K^{-1}), *T* is the absolute temperature in Kelvin, *n* is the number of electrons transferred, *F*= the Faraday constant (96,485 C/equiv), and E^0 is the standard reduction potential for the redox couple. The ratio of Cr/Co is dependent on the applied potential. If the potential is made more negative the ratio becomes larger (i.e. O is reduced). Conversely if the potential is made more positive the ratio becomes smaller (i.e. R is oxidized), and it is expressed with the Randles-Sevcik equation;

$$\frac{i}{nFA} = k^0 \{c_0^o \exp[-\alpha\theta] - c_R^0 \exp[(1-\alpha)\theta]\} \qquad 1.2$$

where $\theta = nF(E - E^0)/RT, k^0$ is the heterogeneous rate constant, α is known as the transfer coefficient, and A is the area of the electrode. This equation relates/links the variables for current, potential and concentration, which makes it possible to obtain the values of two important parameters, namely *i* and K^0. In most cases, the current flow is also directly (proportional) dependent on the flux of material to the electrode surface. For instance,

when O or R is destroyed the decreased concentration promotes the diffusion of new material from solution. The resulting concentration gradient and mass transport is described by Fick's law;

$$\phi = -AD_0(\partial c_0 / \partial x\} \qquad 1.3$$

where D_0 is the diffusion coefficient of the new material due to oxidation (O) and x is the distance from the electrode surface. An analogous equation can be written for R. The flux of O or R at the electrode surface controls the rate of reaction, and thus the faradic current flowing in the cell. In the bulk solution, concentration gradients are generally small and ionic migration carries most of the current. The current is a quantitative measure of how fast a species is being reduced or oxidized at the surface of the electrode. The actual value is dependent on factors such as: concentration of the redox species; size, shape and material of the electrode; the solution resistance; and the number of electrons transferred.

Cyclic voltammetry has become an important electro-analytical technique mostly used for the study of redox processes, understanding reaction intermediates and determining the stability of reaction products. It is based on varying the applied potential at a working electrode in both the forward and reverse directions while monitoring the current. Depending on the analysis, one reversible or irreversible cycle can be performed. The important parameters in a cyclic voltammogram are the peak potentials (E_{pa}

and E_{pc}) and the peak currents (i_{pa} and i_{pc}) of the cathodic and anodic peaks (Figure 1.5).

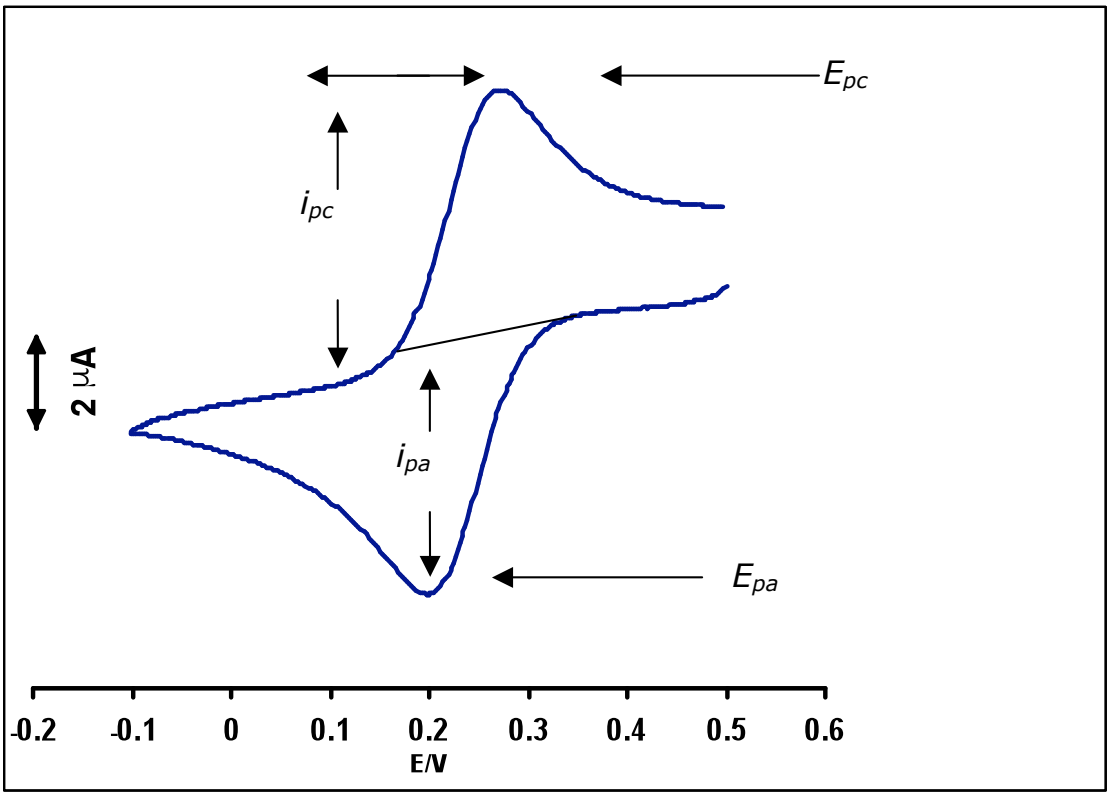

Figure 1.5: A typical reversible cyclic voltammogram plot for a cleaned bare gold electrode. E_{pa} and E_{pc} are the positions of peak voltage at the anodic and cathodic peaks respectively; and i_{pa} and i_{pc} are the peak currents of the anodic and cathodic peaks respectively.

For a fast electron transfer process, i.e. a process not limited by diffusion, migration and convection, the reaction is said to be **electrochemically reversible** (Table 1.1), and the peak current and potential separation is;

$$\Delta E = E_{pa} - E_{pc} = \frac{59}{n} mV \qquad 1.4$$

Where ΔE is the voltage separation between the current peaks, and E_p^a and E_p^c are the positions of peak voltage at the anode and cathode. In a normal cyclic voltammogram (CV) of a surface characterization of a bare gold electrode, it can be observed that when the voltage sweeps past a potential that is related to an active electrochemical reaction the resultant current will increase, creating a peak (this is either the anodic or cathodic peak depending on the direction of the applied potential).

After this first peak, the current will stabilize once the available reactants have been consumed almost completely (this is equilibrium). On the reverse voltage scan, the reverse electrochemical reaction may be observed (Figure 1.5) [46]. At room temperature, for a reaction with n electrons transferred, ΔE should theoretically be 0.0592/n, but experimentally it is usually slightly greater than this, because of external factors such as cell resistance.

Table 1.1: Reversible and irreversible cyclic voltammograms compared.

Parameter	**Reversible voltammogram**	**Irreversible voltammogram**
I_{pc} and I_{pa}	I_{pc} equals or approximately equals I_{pa}	There is a significant difference between I_{pc} and I_{pa}
E_{pc} - E_{pa} at room temperature	The difference between E_{pc} and E_{pa} is 59mV/n.	Not applicable. Because there is only one peak potential.
E_{pc} and E_{pa}	Independent of the scan rate (v)	Dependent on the scan rate (v)
I_p and $v^{1/2}$	I_p is proportional to $v^{1/2}$	I_p is proportional to $v^{1/2}$

Key: I, current; E, potential; pc, peak cathode; pa, peak anode; n, electrons involved in the reaction; v, scan rate.

For a reversible reaction the concentration is related to the peak current by the Randles –Sevĉik expression;

$$i_p = 2.686x10^5 n^{3/2} Ac^0 D^{1/2} v^{1/2} \qquad 1.5$$

Where i_p is the peak current in amps (A), A is the area of the electrode surface in cm^{-2}, D is the diffusion coefficient, c_o is the concentration in $mol.cm^{-3}$, and v is the scan rate in $V.s^{-1}$.

For an electrochemically **irreversible process** (Table 1.1), either the oxidation or reduction peak is observed, but at times with a weak reverse

peak. This process is usually due to slow electron exchange or slow chemical reactions at the electrode surface [48]. The Nernst equation is not applicable in this case since the rate of electron transfer is insufficient to maintain surface equilibrium and thus the oxidized and reduced species are not in equilibrium. The peak current, I_p for an irreversible process is given by the equation:

$$I_p = (2.99 \times 10^5)\, n\, [(1-\alpha)n]^{1/2}\, A\, c\, (Dv)^{1/2} \qquad 1.6$$

where α is the rate of electron transfer and c is the concentration of the active species in mol cm^{-3}. The rest of the symbols are as identified before and as listed in the Table of Symbols.

For a totally irreversible system, ΔE_p is calculated from the equation:

$$\Delta E_p = E^{o'} - RT/\alpha nF\, [0.78 - \ln(k^o/D^{1/2})\, \ln(\alpha nF/RT)^{1/2}] \qquad 1.7$$

k^o = heterogeneous electron transfer coefficient ($cm.s^{-1}$).

The electrode system

Typically an electrochemical cell has two or three electrodes; the type employed solely depend on the sample (i.e. type or amount of sample), Cyclic voltammetry employs a three electrode system, namely **(i) a working electrode,** which can be gold, platinum, mercury, etc., **(ii) a**

reference electrode, against which the potential is measured; e.g. a standard calomel electrode (SCE) or silver|silver chloride (Ag|AgCl) and **(iii) a counter electrode,** such as platinum wire, loops or foil.

1.4.2 Electrochemical impedance spectroscopy (EIS)

Electrochemical impedance spectroscopy (EIS) is a well-developed branch of alternating current (ac) techniques that describes the response of a circuit to an alternating current or voltage as a function of frequency. Unlike other electrochemical techniques that employ direct current, in EIS a small alternating perturbing potential (~5 mV) is applied across a cell or sample at a certain frequency, which results in the generation of an alternating current (figure 1.6) with time.

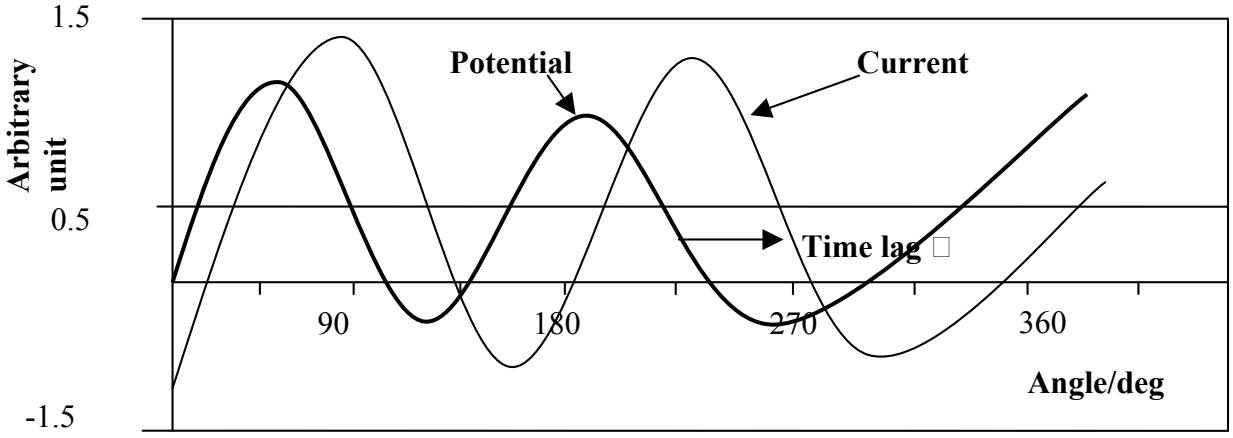

Figure 1.6: A typical impedance analysis showing what happens to the potential and current during analysis.

The current induced in response to the varying potential will be out of phase, by time lag θ, and of a different magnitude. The term impedance denotes an opposition to flow of electrons or current- resistance. In alternating current (ac) theory, the resistance is defined by Ohm's Law:

$$E = I Z \qquad 1.8$$

Where E is the potential and it is directly proportional to the current (I) and the impedance (Z), the ac equivalent of resistance measured in ohms (Ω). Resistors, capacitors and inductors similarly impede the flow of electrons in ac circuits. In an electrochemical cell, slow electrode kinetics, preceding chemical reactions and diffusion can all impede electron flow, and can be considered analogous to the resistors, capacitors, and inductors that impede the flow of electrons in an ac circuit.

Advantages of EIS over dc techniques

i. EIS techniques use very small excitation amplitudes, often in the range of 5 to 10 mV peak-to-peak, which causes only minimal perturbation of the electrochemical test system, thus reducing errors caused by the measurement technique;

ii. EIS experiments provide data on both electrode capacitance and charge-transfer kinetics, these techniques can provide valuable mechanistic information;

iii. Because the technique does not require a potential scan, one can make measurements in low conductivity solutions where direct current (dc) techniques are subject to serious potential-control errors;

iv. The main advantage of EIS is that one can use a purely electronic model to represent an electrochemical cell. This is because an electrode boundary undergoing an electrochemical reaction is typically equivalent to an electronic circuit consisting of a specific combination of resistors and capacitors.

The Nyquist plot

The Nyquist plot (Figure 1.7) is a popular format of representing EIS data. It is a plot of the imaginary impedance component (Z”) versus the real impedance component (Z') at each excitation frequency. As seen in figure 1.7 at high frequencies, the impedance of the Randles cell was almost entirely created by the uncompensated resistance of the solution between the working and reference electrodes (ohmic resistance, RW). The frequency reaches its high limit at the leftmost end of the semicircle, where the

semicircle touches the x-axis. The frequency reaches its low limit at the rightmost end of the semicircle.

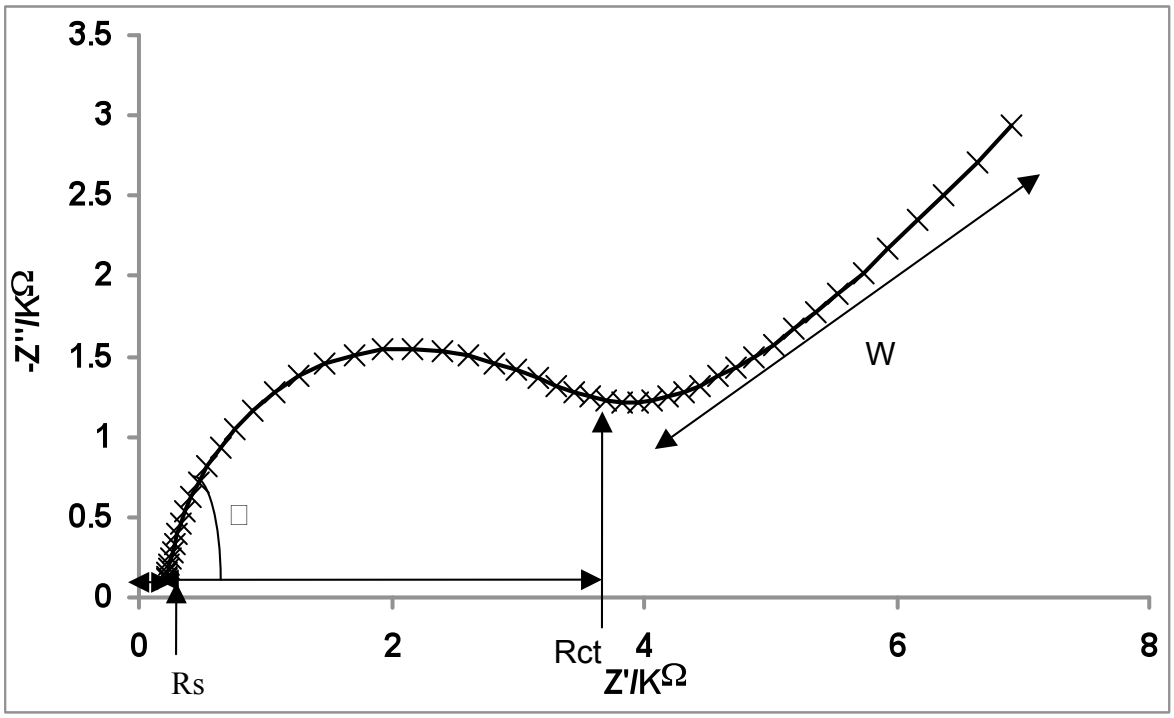

Figure 1.7: A simple Nyquist plot for a one electron transfer process. R_s, solution resistance; R_{ct}, Charge transfer resistance; W, Warburg coefficient, □, the time lag experienced between the voltage and the current.

The Nyquist plot format makes it possible to determine the effect of the R_s, by extrapolating the semicircle toward the left, down to the X-axis. By using this plot it is possible to compare two experiments that differ in the position of the reference electrode, because the shape of the curve is not affected by the changes in the electrolyte resistance (R_s). The Nyquist has some drawbacks which includes that the frequency does not appear openly; although the ohmic resistance and charge-transfer resistance at the

electrode/solution interface (polarization resistance, Rp or R_{ct}) can be easily read directly from the Nyquist plot, the electrode capacitance can be calculated only after the frequency is known.

The bode plot

The Bode plot is a useful alternative to the Nyquist plot. The plot format makes it possible to determine the absolute impedance, |Z|, as a function of frequency. In this plot the frequency appears in one of the axes, thus it is easy from these plots to understand how the impedance depends on the frequency.

The log |Z| vs. log *w* curve yield values of Rp and R_s. At the highest frequencies (Figure1.8), the R_s dominates the impedance and log (z) can be read from the high frequency horizontal plateau. At the lowest frequencies, polarization resistance also contributes, and the log (R_s + Rp) can be read from the low frequency horizontal plateau. At intermediate frequencies, this curve should be a straight line with a slope of -1. If this line is extrapolated back to the log |Z| axis at w = 1 yields the value of C_{DL} from the relationship:

$$|Z| = 1/C_{DL} \qquad 1.9$$

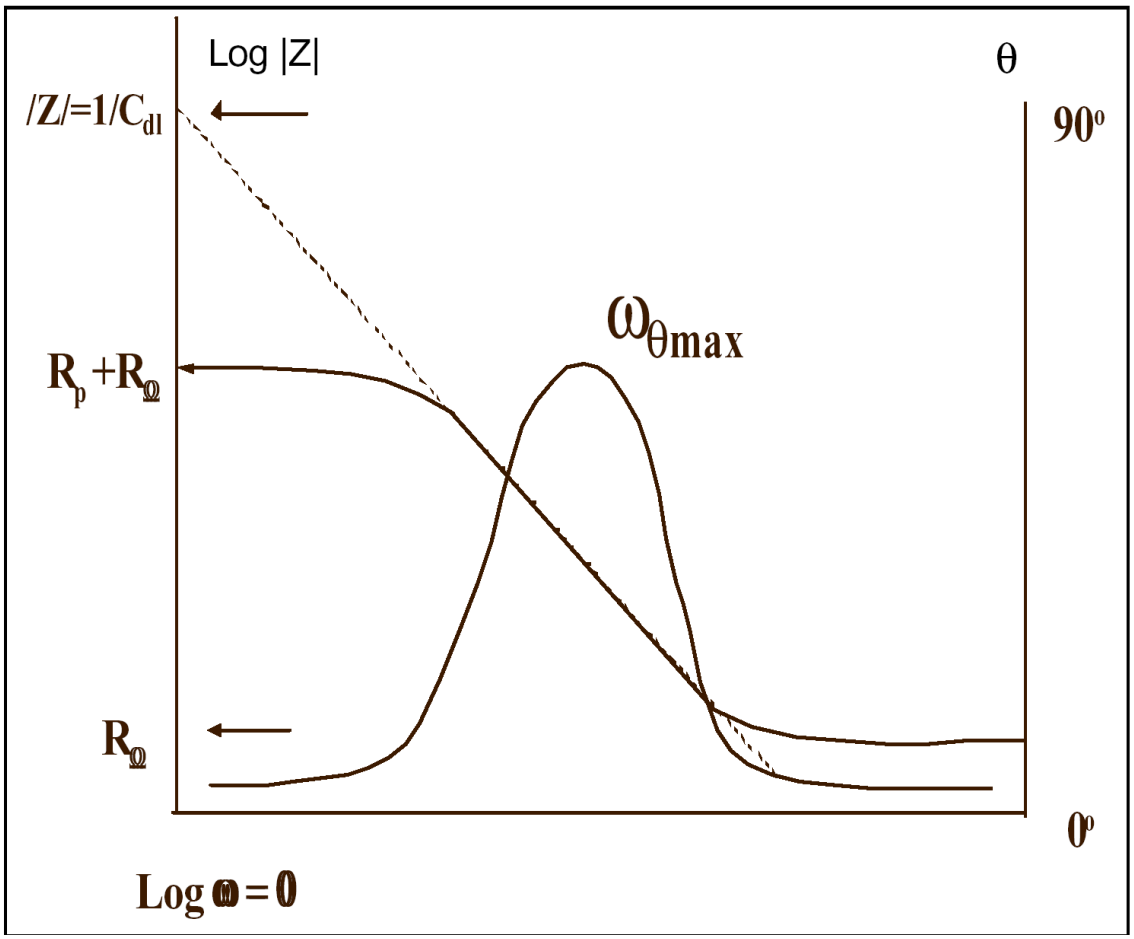

Figure 1.8: Bode plot for a simple electrochemical system

Bode plot Versus the Nyquist plot

The Bode plot allows one to avoid the longer measurement times associated with low frequency Rp determinations. It is also advantageous when data scatter prevents adequate fitting of the Nyquist semicircle. In general the Bode plot is a useful alternative to the Nyquist plot as it provides a clearer description of the electrochemical system's frequency-dependent behaviour than does the Nyquist plot, in which frequency values are implicit. In some electrochemical processes there are more than one rate limiting steps, with

their own impedance data which contribute to the overall rate limiting reaction. The greatest disadvantage of the Bode plot over the Nyquist plot is that the shapes of the curves are dependent on the uncompensated resistance (Figure 1.8). Unlike the Nyquist plot, the Bode plot makes it easy to identify the frequency break points associated with each limiting step (Figure 1.9).

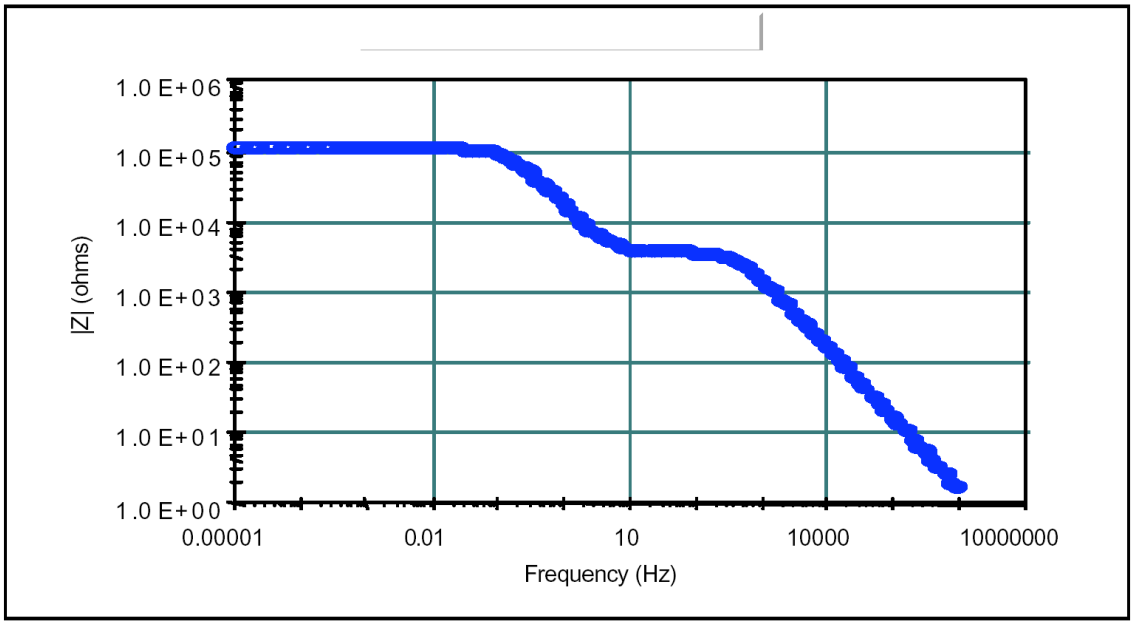

Figure 1.9: Bode plot for a two time rate limiting step (Impedance versus frequency).

To determine whether or not the experimental impedance data (Nyquist and Bode plots) can be fitted to any equivalent circuit, each impedance spectrum should be fit subjected to the Krame-Kronig (K-K) assumptions; which state that:

i. The impedimetric response is only related to the excitation signal and is linear
ii. The system does not change with time, say due to ageing, temperature changes, non-equilibrium conditions, etc; and
iii. The system is finite for all values of ω, including zero and infinity [49, 50].

Apart from visual assessment of the line fittings, two precise ways to establish how well the modelling functions to reproduce the experimental data sets are the relative error estimates (in %) and chi-square functions (χ^2) [62]. χ^2 is the sum of squares of the relative residuals, easily attained from the K-K test. Failure of the K-K test, shown by a large value of pseudo χ^2 is an indication that no good fit can be obtained using the electrical circuits equivalent method.

Experimental impedance data of an electrochemical cell can be straight forwardly fitted to the impedance of a corresponding circuit that primarily consists of resistors and capacitors. This circuit model is the heart of impedance analysis. In such circuits, a resistance superlatively expresses a path that is conductive, like one which is generated by the bulk conductivity of the system or the charge-transfer step due to an electrode response. On the other hand, a capacitor commonly describes space-charge-polarisation regions inside the system similar to modification of an electrode surface due to adsorption processes or polymer-layer deposition. The Randles circuit in

Figure 1.10 is the simplest equivalent circuit that describes an electrochemical cell where a single-step Faradaic process in the presence of diffusion may occur [51].

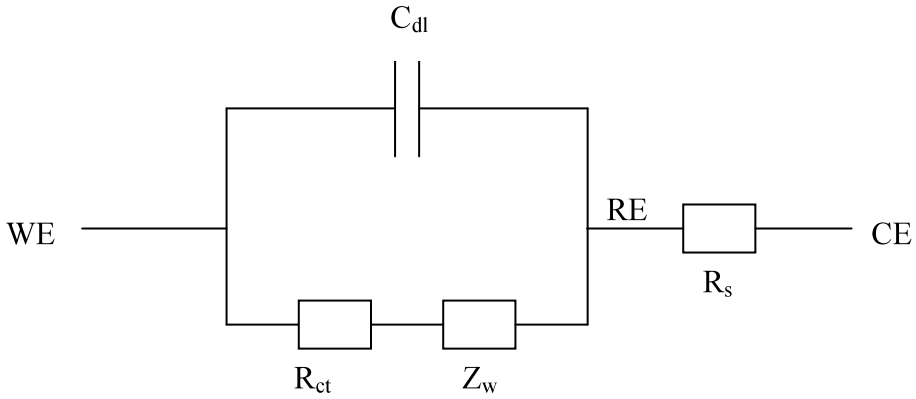

Figure 1.10 Randles equivalent electric circuit (for an ideal situation).WE, Working electrode; RE, Reference electrode; Counter electrode.

It consists of three components, namely the electrolyte resistance between working and reference electrodes, the double layer capacitance (C_{dl}), and the Faradaic impedance consisting of charge-transfer resistance (R_{ct}) at the working electrode-electrolyte interface and the so-called Warburg Impedance (Z_w), which reflects the influence of the mass transport of the electro-active species on the total impedance of the electrochemical cell. Thus, for those diffusion-limited procedures, Z_w becomes dominant, and for the other charge-transfer-controlled processes, only R_{ct} can be obtained.

For a practical condition, the double layer capacitance (C_{dl}) in the Randles equivalent electric circuit is replaced by the constant phase element (CPE) as depicted in Figure 1.11.

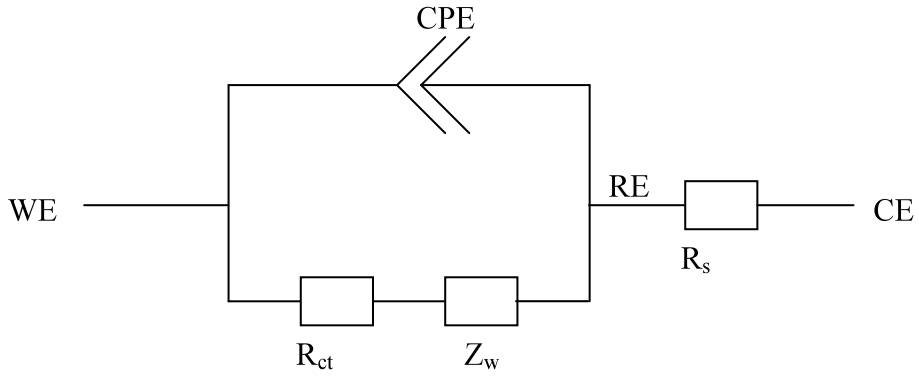

Figure 1.11 Modified Randles equivalent electric circuit (for a real practical situation).

The impedance of the CPE (Z_{CPE}) is a power-law dependent interfacial capacity defined as

$$Z_{CPE} = \frac{1}{[Q(j\omega)^n]} \qquad 1.10$$

where Q is the frequency-independent constant relating to the surface electroactive properties, ω is the radial frequency, the exponent n arises from the slope of log Z vs log f (and has values $-1 \leq n \leq 1$). If $n = 0$, the CPE behaves as a pure resistor. If $n = 1$, CPE works as a pure capacitor, and if $n = -1$ CPE behaves as an inductor. The value of $n = 0.5$ corresponds with Warburg impedance (Z_w) which is related to the domain of mass transport control which takes place from the diffusion of ions to and from the electrode|solution interface. Generally speaking, CPE is influenced by several factors such as:

(i) The nature of the electrode (e.g., roughness and polycrystallinity) [52],

(ii) Distribution of the relaxation times due to heterogeneities existing at the electrode/electrolyte interface [52],

(iii) Porosity and dynamic disorder associated with diffusion [52].

1.4.3 Chemically modified electrodes

There are many well documented methods of electrode modification, which include:

(i) Self-assembled monolayer (SAM) strategy: In this method the desired molecule is spontaneously adsorbed from its solution directly on to the surface of the appropriate substrate [53]. A broad overview of SAM strategy will be discussed in the next section (1.5).

(ii) **Dip-dry or Immersion**: In this method, the electrode is dipped in a solution of the modifier for a period sufficient for spontaneous film formation to occur by adsorption. The electrode is then withdrawn from the modifier's solution and the solvent is allowed to dry.

(iii) **Drop-dry**: In this method, the electrode is coated by depositing droplets of the desired modifier solution on its surface. The droplets are then allowed to dry on the surface.

(iv) **Spin-Coating**: In this method, a few droplets of the modifier solution are deposited on the surface. The droplets are then evaporated by spinning the electrode on a spin coater.

(v) **Electrodeposition or potential cycling**: In this method, the electrode surface is coated by electrochemically running voltammetric scans in the solution of the modifier (i.e. not the electro-active probe).

(vi) **Covalent attachment**: In this method, the modifier is attached to the surface using a coupling reagent. Another monolayer(s) can subsequently be coupled to the one already on the surface by using an appropriate coupling reagent [54, 55].

The choice of the method to use to modify an electrode depends on the molecule to be attached on the surface and the type of surface (i.e. gold, carbon nanotube, etc.). in this thesis, self-assembly was adopted because of its several advantages for the work proposed. The following section is an overview of this important technique.

1.5 Self-Assembled Monolayer (SAM) Strategy

Self-assembled monolayers are 2 Dimensional (2D) polycrystalline organic super-thin films of semi-rigid molecules that are covalently attached to a suitable substrate, thus giving this substrate a new chemical or electrochemical function [56-61]. Self-assembly is characterized by the spontaneous organization of molecules into specific reproducible arrangements. In addition to the high reproducibility of self-assembled

monolayers, SAMs are simple to prepare, versatile, stable and offer the possibility of introducing different chemical functionalities with high level of order at the molecular dimension [62].

The molecules that are capable of self-assembling into a monolayer consist of three chemical entities, each of which plays an important role in the assembly process (figure 1.12), namely:

i. The terminal group that has a high affinity for the substrate, binds the ligand to the substrate [63, 64];

ii. The spacer unit that separates the head and the terminal groups, drives the spontaneous molecular assembly due to intermolecular interactions [64];

iii. And the head group that constitutes the outermost surface of the monolayer film. This group can be of any desired functionality and its properties define the surface properties of the assembled monolayer and, depending on the properties and size of the head group, it can act as a further driving force for ordering or may act to disrupt the assembly process [64].

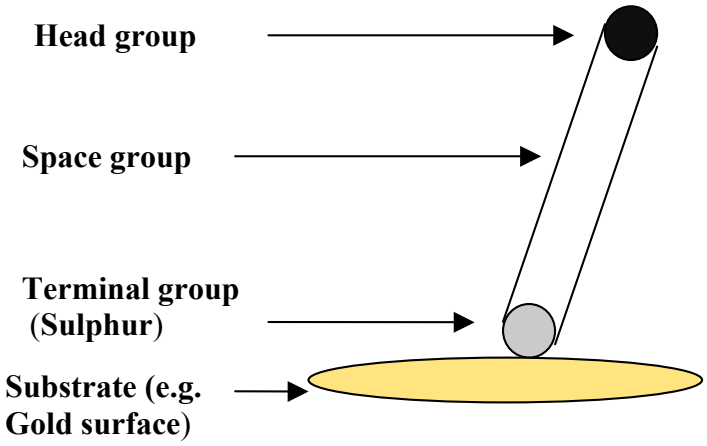

Figure 1.12: Molecules that are capable of forming a self-assembled monolayer.

1.5.1 Self-assembled monolayers of alkanethiols on gold

The study of self-assembled monolayers of alkanethiols and alkyl disulfides on gold was fit reported in 1983 by Nuzzo *et. al.*[65]. Since then, self assembly of thiols on gold substrates have grown to be a powerful tool for surface modification. Their basic structures on gold have been ascertained with quantitative precision [66**]**

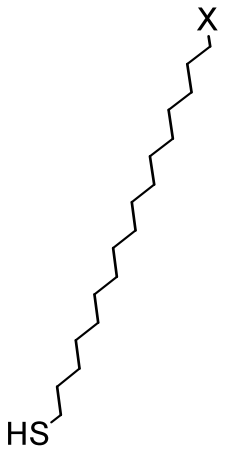

Figure 1.13: A typical structure of an alkanethiol showing its three important entities. X is any functional group (e.g. carboxylic acid, methyl).

The formation of alkanethiol SAMs (figure 1.13) on gold substrates is one of the simplest and fastest self assembly systems [67]. It typically involves immersing a gold coated plate in a solvent, notably ethanolic solution of the desired alkanethiol. At first, within a few seconds to minutes, alkanethiols come down onto the gold surface and form a disordered monolayer (1.14b). As more alkanethiols come to the surface, the layer continues to form and the Van der Waals forces between the hydrocarbon chains of the spacer unit help pack the molecules into a well-ordered structure (figure 1.14c). The rate of this process differs among different alkanethiols. It can take hours to days to get the molecules arranged in their optimal state [68].

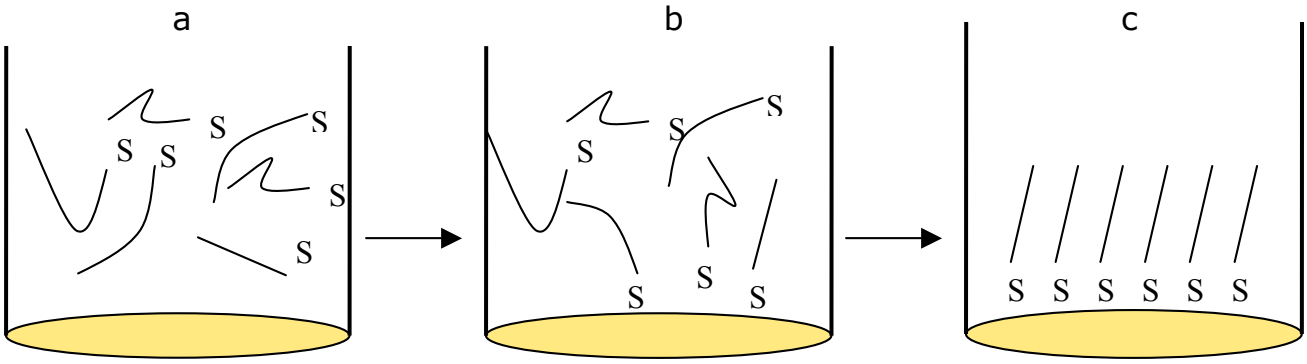

Figure 1.14: Schematic diagram showing the self-assembly process of alkane thiols. (a) Gold coated plate immersed in an ethanolic solution of the desired alkanethiol; (b) after a few seconds to minutes, alkanethiols come down onto the gold surface and form a disordered monolayer; (c) as more alkanethiols come to the surface, the layer continues to form and the Van der Waals forces between the hydrocarbon chains of the spacer unit help pack the molecules into a well-ordered structure.

1.5.2 Advantages of gold-modified alkanethiols SAMs

The advantages of SAM of thiol on gold include:

(i) The simplicity and cost effectiveness of preparation [69-71].

(ii) Sulphur has a high specific affinity for gold, which allows the covalent attachment of sulphur to the gold in the presence of other functional groups on the alkanethiols [69-71];

(iii) The outermost surface properties can be desirably altered by changing the head functional group [69-71].

(iv) In the development of biosensors it is of paramount importance to know the orientation of the immobilized bimolecular component in order to preserve their biological activity, this is possible when using functionalized SAM.

1.5.3 Factors affecting the final and optimal confirmation of the alkanethiol SAM formation

Although the process of a thiol SAM formation is simple and fast, the final optimal configuration is not always achieved. This can be due to one or more of the following factors:

i. **The cleanliness of the gold surface.** This does not affect the attachment of thiols with a head group which is a methyl (figure 1.15A), because the strong driving force between the sulphur and gold interaction will remove the contaminants, unless if the contaminants are oil, contaminated solvent, etc. But in the case of thiols with charged head groups or a bulk functional group along its chain, which reduce the driving force for assembly, removal of the contaminants become difficult;

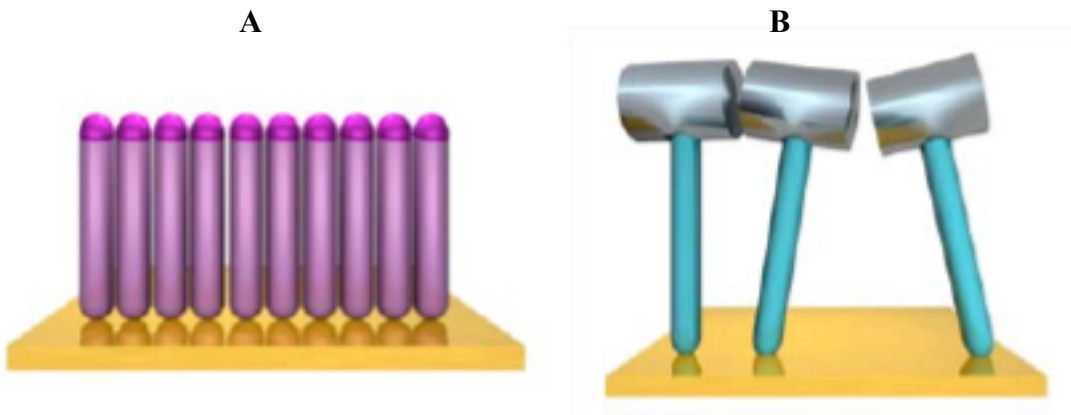

Figure 1.15: A schematic diagram illustrating the effect of head size in the ordering of a SAM pattern. A: Thiol with a small head group (e.g. methyl); B: Thiol with a bulky head group [93].

ii. **Length of the spacer element and type of the head group** (figure 1.15B). It has been reported that the length of the spacer element affects the order/pattern of the SAM of alkanethiol, hence if one is interested in forming a SAM of alkanethiol with an ordered pattern, it is then advisable to use alkanethiols with a longer spacer unit and a small head group [72].

1.5.4 Pinhole parameters

Pinhole defects are known to exist in self-assembled monolayers due to imperfect adsorption leading to disorderly-packed alkanethiol during the assembly process. This disorderly SAM pattern sometimes arises due to loss of adsorbed alkanethiol species during rinsing and use [73], but are mostly

due to collapsed sites on the assembled monolayer which occurs when the packing of the alkanethiols SAM on the substrate is incomplete within localised spots, resulting in the long chain alkyl folding over the defect (Fig. 1.16B) [74]; or from the presence of grain boundaries on the substrate (Fig. 1.16A) and/or monolayer [75, 76] as shown in figure 1.16C. The extents to which these defects occur determine the thickness and degree of molecular order of the immobilised species.

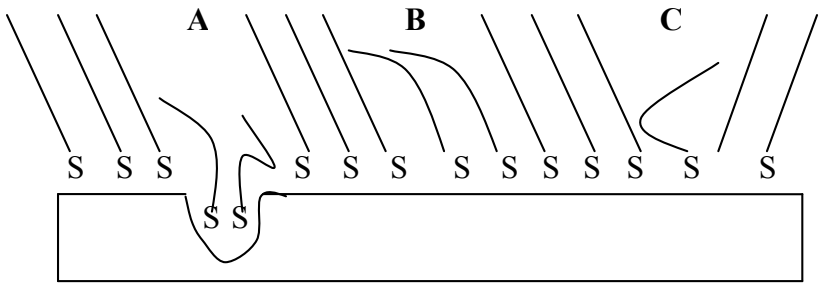

Figure 1.16: Three major causes of pinhole defects. A represent substrate boundary, B: monolayer collapse site and C: monolayer grain boundary.

It is of great importance to determine the presence of pinholes in monolayers. An important parameter to electrochemically probe the presence of pinholes as well as their size is by determining the fractional coverage (θ) of the self-assembled thiol material on the gold electrode. There are many ways to determine this such as:

i. Comparing the charge under the reduction wave corresponding to removal of gold oxide at a monolayer covered electrode versus the respective charge at a bare electrode [77].

ii. Comparing the decrease in the peak current when considering the oxdation/reduction of a monolayer covered electrode with a respective peak current of a bare electrode [78]**.**

iii. And by comparing the magnitude of the charge transfer resistance (R_{ct}.) of the monolayer modified electrode with that of the bare electrode using EIS techniques.

For this study, only the latter method will be discussed.

.

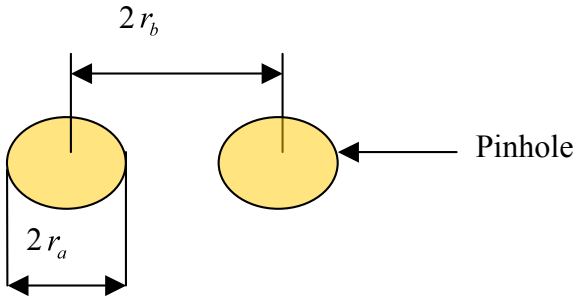

Figure 1.17: Cartoon representation of a pinhole model. The radius of the pinhole is r_a, while r_b is half the distance between the centres of two adjacent pinholes.

Assuming that the electron transfer occurs only at the bare/active sites on the electrode and that diffusion of the sensing redox probe (e.g. $K_3Fe(CN)_6/K_4Fe(CN)_6$)to these active sites is planar [79], then equation one is used to calculate the fractional surface coverage.

$$\theta_{IS}^{R} = 1 - \frac{R_{ct}^{AuE}}{R_{ct}^{SAM}} \qquad 1.11$$

Where θ_{IS}^{R} is the fractional coverage of the surface, R_{ct}^{AuE} and R_{ct}^{SAM} are the charge transfer resistances of the bare gold and the self assembled monolayer modified gold surface respectively. This equation is only applicable to electrodes whose θ_{IS}^{R}less than 0.9 [80]. If that is not the case, equation 1.12 is used to calculate the fractional coverage.

$$\theta_{IS}^{P} = 1 - \frac{\sigma W}{m - \sigma W} \qquad 1.12$$

Where θ_{IS}^{P} is the fractional surface coverage, m is the slope of the linear interval observed in the high frequencies region of the Z'vs $\omega^{1/2}$ function obtained at the respective monolayer modified electrode, and σW is the Warburg coefficient calculated from the characterization of the clean bare gold.

When the fractional coverage of the different electrodes have been calculated, the radius of the pinholes (r_a) and radius of the inactive domain surrounding the electrode (r_b) (Figure 1.17) can be calculated using the model proposed by Amatore C. *et al.* [94], which states that the pinholes are disk-shaped regions with uniform radius and they are homogeneously distributed in the monolayer [81]. Thus, by using equation 1.13 below the r_a and $r_b$can be calculated.

$$\theta_{IS}^{P} = 1 - \frac{\sigma W}{m - \sigma W} = \frac{r_a^{\,2}}{r_b^{\,2}} \qquad 1.13$$

But since there are two unknowns (r_a and r_b) in the equation above, equation 14 is used to determine one of the unknowns.

$$q = \frac{D}{0.36 r_a^2} \qquad 1.14$$

Where D is the diffusion coefficient of the redox couple (7.6×10^{-6} $cm^2 s^{-1}$) [82], q is the transition radial frequency, corresponding to the turning point between the high and low frequency domain in the Z'vs $\omega^{1/2}$ plot, which can be determined from the maximum in the Z''vs $\omega^{1/2}$ plot, as

$$\omega = \text{(maximum in the } Z''\text{vs } \omega^{1/2} \text{ plot)}^2 = \frac{q}{2} \qquad 1.15$$

The pinhole parameters can now be determined using equation 1.13 and 1.14.

1.6 Microscopic and Spectroscopic Characterisation of SAMs

1.6.1 Atomic force microscopy (AFM)

Atomic force microscopy (AFM) belongs to the scanning probe microscopy family. It is a powerful technique used for imaging surfaces; studying their morphology and determining interaction forces between the cantilever and sample [83] (Figure 1.18). These interaction forces are measured by the

cantilever deflection during the AFM tip approach and withdrawal [84]. Atomic force microscopy has been widely used in nanotechnology including nanofabricating [85], imaging [86], force mapping [87], and biosensing [88] applications. In biosensing applications chemical force microscopy (CFM), an AFM derivation, is employed to study inter- and intra-molecular interactions between a modified AFM tip and a sample surface with various molecules and biomaterials [89].

The performance of an AFM is dependent on the physical characteristic of the cantilever and the tip. Due to the small finite size of the tip, AFM relies on raster scanning the tip or the sample to probe an area of the surface in the XY plane to cover a larger surface area. This raster scanning makes it possible to record the tip-sample interaction point by point. Thus the area of the sample surface under study is probed in a time series of measurements, that are then put together point by point and line by line, to synthesize it into a three-dimensional image.

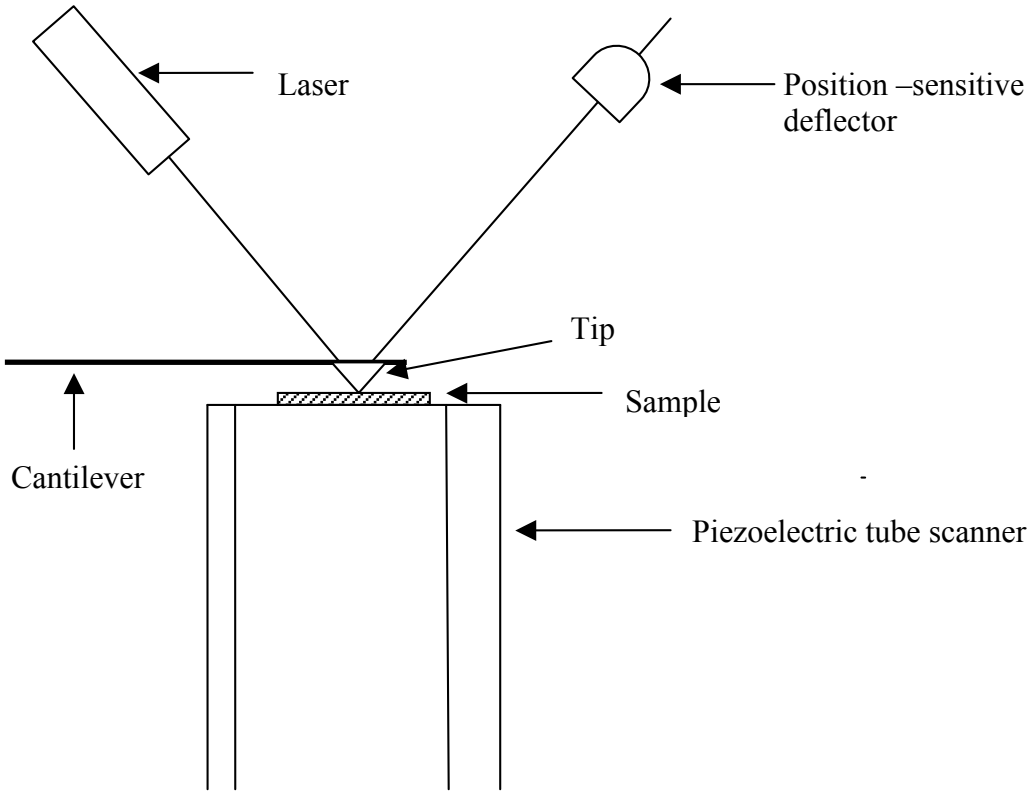

Figure 1.18: Atomic force microscopy: Scheme showing the most common method of detecting the deflection of the cantilever holding the tip.

Raster scanning of the surface area being studied can be done by either a tapping mode or a contact mode operation of the probe (tip). The major disadvantage of the contact mode operation of the tip to scan the surface of the sample is that since the tip is constantly in contact with the surface of the sample, it can cause damage to the sample and alteration of the image, if the downwards force of the tip is not low enough. This phenomenon is usually experienced when scanning surfaces with soft materials, such as biological samples and polymers. It has been reported that this bottleneck can be overcome by using the tapping mode operation of the tip [90]. In the

tapping mode operation the tip is in contact with a specific point on the surface for only a brief time and then it is removed from that surface point to the next point where this processes is repeated.

1.6.2 X-ray photoelectron spectroscopy (XPS)

X-ray photoelectron spectroscopy (XPS) is a powerful technique for the identification of all elements in the periodic table, with the exception of hydrogen and helium. It is commonly used for identifying different elements making up the surface of solids, their oxidation state, type of chemical species to which the element is bonded to and determining their concentrations. Furthermore, the technique also provides information about the electronic structure of molecules [91].

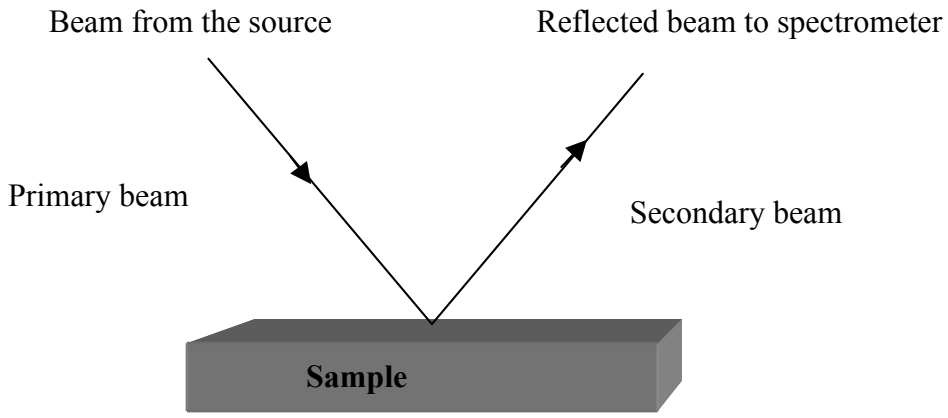

Figure 1.19: General scheme for surface spectroscopy

Solid surface characterization with XPS involves the irradiation of the sample with photons (primary beam). The impact of this beam in the surface results in the formation of a secondary beam, which consists of electrons, whose particles are different from those that make up the primary beam. This secondary beam is then studied with an electron spectrometer (Figure1.19).

A common problem that is usually encountered in XPS based surface analysis is contamination of the surface with atmospheric components such as oxygen or water. These atmospheric gases have been shown to contaminate the surface even if experiments are done under vacuum, for example, when the sample is transferred to the sample holder [92]. Hence it is very important to clean the sample, with either baking the sample at high temperature or sputtering the sample with a beam of inert gas ions in the chamber used for irradiating the sample.

1.7 References

1. WHO report 2009:Global tuberculosis control. *Surveillance, planning, financing.* WHO, Geneva, Switzerland 1.
2. D. Maher, B.G Williams, M.C. Raviglione, C. Dye, E.L. Corbett, C. J. Watt, N. Walker, *Arch. Intern. Med.* 2003, 139, 1009.
3. I. K. R. U. Devi, B. Ramalingam, A. Raja, *J. Diagn. Microbiol. Infec. Disease* 2003, 46,205.
4. G. K. Schleicher, C. Feldman, Y. Vermaak, J.A. Verschoor, *J. Clin. Chem. Lab. Med.* 2002, 40, 882.
5. S.T. Thanyani, V. Roberts, D.G.R Siko, P. Vrey, J.A. Verschoor, *J. Immunol. Methods* 2008, 332, 61.
6. R.C. Hendricks, J. F. Douglas, L.D. Reynold, P.D. Mcneill, D. Carter, S.G. Reed, and R. Houghton, *J. Clin Microbiol*. 2000, 38, 2354.
7. L. Kremer, G.S. Besra, *Expert opin. Invest. Drugs* 2002, 11, 1033.
8. P. Smith, A. Moss. *Epidemiology of Tuberculosis*, 1994: pp. 47.
9. G. Foulon, M. Wislez, J.M. Naccache, F.X. Blanc, A. Rabbat, D. Israël-Biet, D. Valeyre, C. Mayaud, J. Cadranel, *J. Clin. Infec. Diseases* 2004,38, 418.
10. Tuberculosis; Fact sheet No. 104. World Health Organization. Available online at:

http://www.who.int/mediacentre/factsheets/fs104/en(2009). (Accessed on 20 October 2009)

11. J.A. DeSimone, R.J. Pomerantz, T.J. Babinchak, *Ann. Intern. Med.* 2000, 33, 447.
12. R.E. Chaisson, *Clin. Infec. Disease* 2001, 33,1901.
13. S. Khasnobis, V. E. Escuyer, D. Chatterjee, *Expert. Opin. Ther. Targets* 2002, 6, 21.
14. P.E. Kolattukudy, N.D. Fernandes, A.K. Azad, A.M. Fitzmaurice, T.D. Sirakova, *Mol. Microbiol*. 1997, 24, 263.
15. M.J. Pabst, J.M. Gross, J.P. Brozna, M.B. Goren, *J. Immunol.* 1988, 140, 634.
16. M.Rouhi, *Chem. Eng. News* 1999, 77, 52.
17. Y. Yuan, R.E. Lee., G.S Besra, J.T. Belisle, C.E. Barry, 3rd. *Proc. Natl. Acad. Sci.* 1995, 92, 6630.
18. M. Daffe, P. Draper, *Adv. Annu. Rev. Biochem*. 1994, 64, 29.
19. P.J. Brennan, H. Nikaido, *Adv. Annu. Rev. Biochem.* 1995, 64, 29.
20. D. Chatterjee, C.M. Bozic, C. Knisley, S.N. Cho, P.J. Brennan, *Infect Immun*. 1997, 57, 322.
21. K. Mikusova, R.A. Slayden, G.S. Besra, P.J. Brennan, *Antimicrobial. Agents and Chemotherapy*, 199511, 2484.
22. M. Villeneuve, M. Kawai, H. Kanashima, M. Watanabe, D.E. Minnikin, H. Nakahara, *Biochimica et Biophysica Acta*. 2005, 1715, 71.

23. D.E. Minnikin, *Academic press (London)* 1982, 1, 95.
24. D.E. Minnikin, L. Kremer, L.G. Dover, G.S. Besra, *Chem. Biol.* 2002, 9, 545.
25. N. Rastogi, *Res. Microbiol.* 1991, 142, 464.
26. M. A. Attallah, S. Osman, A. Saad, M. Omran, H. Ismail, G. Ibrahim, A. Abo-Nagll, *Clinica Chimica Acta.* 356,2005, 58.
27. S. K. Sharma, A. Mohan , *Indian J Med Res.* 2004,316.
28. E.M. Martin, M.A. Sandra, B. Inger, H.M., A. Ottenhoff Peter, *Infect. Disease* 2001, 183, 175.
29. I.R. Liberato, M.F. de Albuquerque, A.R. Campelo, H.R. de Melo, *Clinica Chimica Acta* 2005, 58.
30. S. Banerjee, S. Gupta, S. Kumar, A.V. Shirikande, M.V. Reddy, B. C. Harinath, *India J. Pathol. Microbiol.* 2003, 46, 261.
31. P. Smith, A. Moss, *Theoretical Population Biology,* 1994, 169.
32. I.C. Shamputa., A.L. Rigouts, F. Portaels, *Apmis*. 2004, 112, 728.
33. E.D Chan, R. Reves, J.T. Belise, P.J., Brennan W.E. Hahn, *Crit. Care Med*. 2000, 161, 1713.
34. T.M. Doherty, A. Demissie, J. Olobo, D. Wolday, S. Britton, T. Eguale, P. Ravan, P. Anderson, *Clin. Microbiol*. 2002, 40, 704.
35. K.P Lyashchenko, M. Singh, R. Colangeli, M.L. Gennaro, *Immunol Methods:* 2000, 242, 91.
36. K. Al Zahrani, H. Al Jahdali, L. Poirier, P. Rene, M.L. Gennaro, D.

Menzies, *Am J. Respir. Crit. Care. Med*. 2000, 162, 1323.

37. G. Toschi, M. Baird, D. Minnikin, J. Grooten, *Expert. Opin. Ther. Patents* 2007, 17, 315.
38. K.M. Samanich, M.A. Keen, V.D. Vissa, J.D. Harder, J.S. Spencer J.T., Belisle, S. Zolla-Pazner, Laal. *Clin. Diag. Lab. Immunol*. 2000, 7, 662.
39. Y. Fujita, T. Doi, K .Sato, I. Yano, *Microbiol.* 2005, 151, 2065.
40. J. Pan, N. Fujiwara, S. Oka, *Microbiol Immunol.* 1999, 9, 863.
41. P. Calvo-Marzal, K. M. Manesh, D. Kagan, S. Balasubramanian, M. Cardona, G. Flechsig, J. Posner, J. Wang, *Chem. Commun.* 2009, 4509.
42. A.P.F. Turner, *Science* 2000, 290, 1315.
43. N. Prabhakar, H. Singh, B. D. Malhotra, *Electrochem. Commun*. 2008, 10, 821.
44. N.K. Chaki, *Proc. Indian Acad. Sci*. 2001, 113, 659.
45. D. Chen, J. Li, Surf. *Sci. Rep*.2006, 61, 445.
46. S. Won Cha, R. O'Hayre, Y. Park, F.B. Prinz, *Journal of Power Sources 2*008, 1735.
47. A.E. Kaifer, M. Gomez-Kaifer, *Supramolecular electrochemistry*, Wiley-VCH, Germany 1999.

48. Hawkridge F. M. (1996). In P. T., Kissinger & W. R., Heineman (Eds.), Laboratory techniques in electroanalytical chemistry (2nd edn.), Marcel Dekker Inc.: New York.W.R. (pp85).
49. G. Láng, K.E. Heusler*, J. Electroanal. Chem.* 1998, 457, 57.
50. V. B. Shikini , I. S. Smirnova, S. S. Nazin*, Chemistry and Materials Science* 2008, 972.
51. G.Z. Liu, T. Böcking, J.J. Gooding, *Electroanal. Chem*. 2007, 335.
52. M. Situmorang, D.B. Hibbert, J.J. Gooding, D. Barnett, *Analyst,* 1999,124, 1775.
53. J.J Gooding, D.B. Hibbert, *TrAC,* 1999, 18, 52.
54. B.F. Watkins, J.R. Behling, E. Kariv, L.L. Miller, *J. Am. Chem. Soc.* 1975, 97, 3549.
55. L. Netzer and J. Sagiv, *J. Am. Chem. Soc*. 1983, 105, 674.
56. A. Ulman, An Introduction to Ultrathin Organic Films: from Longmuir-Blodgett to self-assembly, *Academic Press, San Diego (*1991).
57. A. Ulman, *Chem. Rev*. 1996, 96, 1533.
58. A. Ulman (Ed.), *Academic Press*,1998, 125.
59. F. Schreiber, Prog. *Surf. Sci.* 65, 2000, 151.
60. A. Ulman, *Acc. Chem. Res*. 2001, 34, 855.
61. F. Schreiber, J. Phys: *Condens. Matter* 2004, 16, 881.
62. S. skaa, C. Orlewskab, D. Janssenc, W. Dehaenc, H. Radeckaa, *Electrochim. Acta* 2008,7932.

63. L. H. Dubois; R. G. Nuzzo, *Annu. Rev. Phys. Chem.* 1992, *43*, 437.

64. T. Weidner, K. Rossler , P. Ecorchard , H. Lang, M. Grunze , M. Zharnikov, *J. Electroanal. Chem*. 2008, 621, 159.

65. R. G. Nuzzo; , D. L. Allara, *J. Am. Chem. Soc.* 1983, 105, 4481.

66. J.C. Love, L.A. Estroff, J.K. Kriebel, R.G. Nuzzo, G.M. Whitesides, *Chem. Rev.* 2005, 105, 1103.

67. J. Dai, Z. Li, J. Jin, Y. Shi, J. Cheng, J. Kong, B Shuping, j.jelechem. 2009, doi:10.1016.

68. H. A. Biebuyck, C. D. Bain, G. M. Whitesides, *Langmuir* 1994,10,1825.

69. M. A. Chesters, G. A. Somorjai, *Surf. Sci.* 1975, 52, 21.

70. R. G. Nuzzo, F. A. Fusco, D. L. Allara., *J. Am. Chem. Soc.* 1987, 109, 2358.

71. C. D. Bain, E. B. Troughton, Y.T. Tao, J. Evall, G. M. Whitesides, R. G. Nuzzo., *J. Am. Chem. Soc.* 1989, 111, 321.

72. C. D. Bain, J.Evall, G. M Whitesides., *J. Am. Chem. Soc.* 1989, 111, 7155.

73. S. Campuzano, M. Pedrero, C. Montemayor, E. Fatas, J.M. Pingarron, *J. Electroanal. Chem*. 2006, 586, 112.

74. H.O. Finklea, S. Avery, M. Lynch, T. Furtsch, *Langmuir* 1987, 3, 409.

75. X. Cui, D. Jiang, P. Diao, J. Li, R. Tong, X. Wang, *J. Electroanal. Chem*. 1999, 48, 243.

76. L.V. Protsailo, W.R. Fawcett, *Electrochim. Acta.* 2000, 45, 3497.

77. Y. Yang, S.B. Khoo, *Sens. Actuators B*. 2004, 97,221.

78. E. Sabatini, H.O. Finklea, *J. Phys. Chem*. 1987, 91, 6663.

79. R.P. Janek, W.R. Fawcett, *Langmuir*. 1998, 14, 3011.

80. H.J C. Amatore, J.M. Saveant, D. Tessier, *J. Electroanal. Chem*. 1983, 147, 39.

81. P. Diao, M. Guo, R. Tong, *J. Electroanal. Chem*. 2001, 491, 98.

82. R. G. Compton, C.E. Banks, *ElectroChemica Acta.* 2007, 52, 4305.

83. W.R Bowen, N. Hilal, R.W. Lovitt, P.M. Williams, *J* Membrane Science 1996, 110, 229.

84. K Hyunsook, N. Jaegeun, H. Mashiko, L. Haiwon, *J. Ultramiscropy* 2008, 108, 1140.

85. M.S. Barrow, W.R. Bowen, N. Hilal, A. Al-Hussany, P.R. Williams, R.L. Williams, C. Wright, *Mathematical, Physical and Engineering Science* 2003, 459, 2885.

86. C.-M. Yam: *Med. Microbiol*. 2003, 52, 999.

87. Y. Harada , *Phys. Rev*. 2000, 61, 12854.

88. Y. Dong, *Sensors and Actuators* B. 2005, 108, 622.

89. D.V Vezenov, A. Noy, P. Ashby, *J. Adhesion Sci. Technol*. 2005, 19, 313.

90. Y.E Strausser, T.Y. Wang, H.R. Jen, G.S. Chen, G.B. Stringfellow, *J. Appl. Phys*: 1990, 67, 563.

91. T. A. Brummelaar, B. D. Mason, Jr. Roberts, W. G. Bagnuolo, W. I. Hartkopf, H. A. McAlister, N. H. Turner, *J. Astronomical* 1996, 112, 1180.

92. B. Sclavi, S. Woodson, M. Sullivan, M. Chance, M. Brenowitz, *Methods Enzymol.* 1998, 295, 379.

93. Assemblon, Inc. Self-assembling Molecules. Available online at: WWW.asemblon.com. (accessed on 17/10/2008)

94. C. Amatore, J.M. Saveant, D. Tessier, *J. Electroanal. Chem*. 1983, 147, 39.

Chapter two:

Experimental

2.1 Materials

2.1.1 List of reagents and buffers

Cysteamine (~95% pure) and stearic acid were obtained from Sigma and Hopkin and Williams Ltd, respectively. Dicyclohexylcarbodiimide (DCC 99% pure) used as condensing agent was obtained from Aldrich. Saponin was obtained from Sigma. N, N-Dimethylformamide (DMF) was purchased from Applied Biosystems (a division of Perkin-Elmer, Great Britain) and was dried and distilled within hours/days before use. Phosphatidylcholine (PC) used for preparing liposomes was obtained from Sigma. Potassium Chloride (KCl), Sodium chloride (NaCl), Potassium Dihydrogen Phosphate (KH_2PO_4), Ethylenediaminetetraacetic acid (EDTA), Sodium Phosphate (Na_2HPO_4), and sodium azide (NaN_2) used for preparing the buffer (PBA/AE) were purchased from Sigma. Potassium Ferricyanide ($K_4Fe(CN)_6$) and Sodium Hydroxide (NaOH) were obtained from Bio-zone chemicals. Pottasium Ferrocyanide ($K_3Fe(CN)_6$) was purchased from B.O. Jones LTD. Ethanol and Sulphuric acid (H_2SO_4) were purchased from SAARCHEM. SPR gold disks and Polycrystalline gold electrode (BAS, r = 0.8 mm) were obtained from Metrohm.

Mycolic acids: Mycobacterial mycolic acids (MA) were isolated from a culture of *M. tuberculosis* H37Rv (American Type Culture Collection 27294) as previously described [1].

Source of sera: Human sera consisted of one tuberculosis and Human Immunodeficiency Virus -positive (TB^+/HIV^+) and one tuberculosis and Human Immunodeficiency Virus -negative (TB^-/ HIV^-) as a control, which were part of a collection used for another study [2] and were selected from the general medical wards of the Helen Joseph Hospital, Johannesburg (South Africa). The TB^+/HIV^+ serum was from a patient with newly-diagnosed culture-positive active pulmonary tuberculosis who was not on anti-TB chemotherapy at the time of serum collection. The TB^-/ HIV^-patient had a medical condition other than TB or AIDS.

Phosphate-buffered saline containing sodium azide and EDTA (PBS/AE, pH 7.4): Phosphate-buffered saline containing sodium azide (0.025 %, m/v) and 1 mM EDTA (PBS/AE, pH 7.4) were prepared with appropriate amounts of Na_2HPO_4 (7.5 mM), KH_2PO_4 (1.5 mM), NaCl (0.14 M) and KCl (2.5 mM). The pH of the buffer was adjusted to 7.4 with 1 M sodium hydroxide (NaOH). The PBS/AE was saturated with nitrogen before any experiments were performed.

Ultra pure water of resistivity better than 18.2 MΩcm was obtained from a Milli-Q Water System (Millipore Corp., Bedford, MA, USA) and was used throughout for the preparation of solutions.

Liposomes: Liposomes with and without mycolic acids (MA) were prepared from a phosphatidylcholine (PC)/$CHCl_3$ stock solution (100 mg/ml) as previously reported [3, 4]. Briefly, MA-containing liposomes were prepared by mixing 90 µL of PC/$CHCl_3$ stock solution (100 mg/ml) with 1 mg of dried mycolic acids. Empty liposomes (i.e., without MA) were prepared consisting of only PC/$CHCl_3$ solution. The PC/$CHCl_3$ contents in an amber glass vial were initially vortexed to ensure thorough mixing, dried at 85 ^{0}C (using a heat block) under a stream of pure nitrogen gas for about 10 min. Liposome formation was induced by addition of 2 ml of saline (0.9% NaCl) and placing in a heat block at 85 °C for 20 min, with vortexing every 5 min. The liposomes were then sonicated using a Branson sonifier (Model B-30, Branson Sonifier Co., USA) for 2 min at 30% duty cycle at an output of 3%. Subsequently, the liposomes were divided into 200 µl aliquots, freeze-dried and stored at –70 ^{o}C until ready for use. Before use, the liposomes were reconstituted with 2 ml of PBS/AE (pH 7.4), heated at 80 ^{o}C for 20 min and then sonicated as before. The final liposome concentration was 500 µg/ml.

2.1.2 Apparatus and Operating Procedures

Electrochemical experiments: All electrochemical experiments were carried out using an Autolab Potentiostat PGSTAT 302 (Eco Chemie, Utrecht, Netherlands) driven by GPES and FRA softwares version 4.9. Electrochemical impedance spectroscopy (EIS) measurements were performed between 10 mHz and 10 kHz using a 5 mV rms sinusoidal modulation in PBS/AE solution of 1 mM $K_4Fe(CN)_6$ / $K_3Fe(CN)_6$ (1:1) mixture containing 0.1 M KCl, and at the $E_{1/2}$ of the $[Fe(CN)_6]^{3-/4-}$ (0.27 V vs. Ag|AgCl, sat'd KCl). Polycrystalline gold (BAS, r = 0.8 mm) was used as the working electrode. Ag|AgCl sat'd KCl and platinum rod was used as reference and counter electrodes, respectively. All solutions were de-aerated by bubbling pure nitrogen (Afrox) prior to each electrochemical experiment. All electrochemical experiments were performed at 25±1 °C.

Microscopic and Spectroscopic experiments: AFM images were obtained at SAM-modified and/or bare SPR gold disks (Eco-Chemie) using an AFM 5100 System (Agilent Technologies, AC mode AFM scanner interfaced with a PicoScan controller, scan range 1.25 μm in x–y and 2.322 μm in z, silicon type PPP-NCH-20 (Nanosenso®) of thickness 4.0±1.0 μm, length 125±10 μm, width 30±7.5 μm, spring constants 10 – 130 N m^{-1}, resonant frequencies of 204 – 497 kHz and tip height of 10-15 μm). All images (256 samples/line × 256 lines) were taken in air at room temperature and at scan

rates 0.9–1.0 lines s^{-1}. The X-ray photoelectron spectra (XPS) were obtained at SAM-modified SPR gold disks using a Physical Electronics model 5400 spectrometer system with monochromatic Mg K α radiation at 1253.6 eV at take-off angles of 15° and 45°.

2.2 Methods:

2.2.1 Cleaning of the bare gold electrodes

Before modification the gold electrodes were polished with Al_2O_3 (0.01 µm grain size), rinsed thoroughly with Millipore water and absolute ethanol respectively, then sonicated for 10 minutes (min) in absolute ethanol. After sonication, the gold electrodes were cleaned by dipping in a hot piranha solution (hydrogen peroxide and sulphuric acid; 1:3 v/v). Finally the gold electrodes were electrochemically cleaned by cycling ten times within the potential window -0.5 and 1.5 V at a scan rate of 100 mVs^{-1} in 0.5 M H_2SO_4, in order to remove residual contaminants. This electrochemical cleaning showed an anodic peak current near +1.1 V and a single cathodic peak near +0.9 V, which is characteristic of a clean gold surface [**5**]. The electrodes were finally rinsed with Millipore water and dried with nitrogen gas. Subsequently, the real surface area of the bare gold electrode was determined from the reversible electrochemistry of $K_4Fe(CN)_6/K_3Fe(CN)_6$ as

described before [6, 7]. It was found to be 0.0257 cm^2 giving a surface roughness factor of 1.28 (ratio of real to geometrical surface area). Where applicable the real surface area was used for all calculations.

2.2.2 Fabrication of a SAM Mycolic acid surface

2.2.2.1 Coating of the bare gold substrate with cysteamine

A self assembled monolayer of cysteamine was allowed to form on the gold electrodes' surface, by incubating the electrode in 10 mM 80% ethanolic solution of cysteamine for 24 hours (h) at room temperature. The Au substrates were then rinsed with Millipore water to remove any physically adsorbed cysteamine.

2.2.2.2 Coupling of stearic acid to cysteamine which is already attached to the Au substrate (referred to here as MEODA modified electrode)

In a polystyrene cup 0.013 g stearic acid, 0.014 g DMAP and 0.024 g DCC were dissolved in 5ml dry DMF. In this solution the cysteamine modified electrode was incubated (as in 2.2.2) for 24 h at room temperature under

nitrogen gas. The Au substrates were then rinsed with DMF and Millipore water to remove any physically adsorbed stearic acid.

2.2.2.3 Non-covalent attachment of Mycolic acid to a MEODA modified Au substrate

In a polystyrene cup 1 mg mycolic acid was dissolved in 2 ml dry and freshly distilled DMF. The stearic acid modified electrode was then incubated in this solution for 48 h at room temperature. The Au substrates were then rinsed with DMF and PBS/AE solution (pH 7.4) respectively, to remove the excess of physically adsorbed MA species.

2.2.2.4 Blocking of the Mycolic acid modified Au surface with saponin

In a column cup the mycolic acid modified electrode was incubated in a saponin solution (1.5 mg/ml PBS/AE) for 10 min. The Au substrates were rinsed with PBS/AE solution (pH 7.4) and the surface characterized with EIS and CV using PBS/AE containing the Ferri/Ferrocyanide pair at pH 7.4.

2.2.2.5 Detection of mycolic acid antigen-antibody interactions

Human sera (HIV^+/TB^+ and HIV^-/TB^-) were appropriately diluted in empty liposome diluted in PBS/AE (pH 7.4) (1:2000; 1:1000 and 1:500 v/v, i.e., 0.05, 0.1 and 0.2% serum, respectively). For control experiments, a similar procedure was followed using liposomes containing MA. The modified electrode (working electrode) was incubated in the required serum solution for 10 min, rinsed in a copious amount of PBS/AE (pH 7.4) to remove any physically adsorbed species before performing the EIS experiment in a test solution of 1 mM equimolar $[Fe(CN)_6]^{4-}$ / $[Fe(CN)_6]^{3-}$ (PBS/AE, pH 7.4) at a bias potential of 0.27 V (vs Ag|AgCl, sat'd KCl).

Safety Note: All glassware in contact with human sera (both TB positive and negative) were sterilized by autoclaving for 20 min at 115 ^oC after use. Waste solutions were carefully collected and sterilized before disposal. All students and lecturer who were working in the lab where the antibody-antigen interaction analysis experiments were conducted were vaccinated against hepatitis B.

2.3 References

1. M.A.Goodrum, , D.G.R.Siko, T. Niehues, D. Eichelbauer, J.A. Verschoor, Microbios. 2001, 106, 55.
2. G. K. Schleicher, C. Feldman, Y. Vermaak, J.A. Verschoor, *J. Clin. Chem. Lab. Med.* 2002, 40, 882.
3. S.T. Thanyani, V. Roberts, D. G.R. Siko, P. Vrey, J.A. Verschoor, J. Immunol. Methods, 2008,332, 61.
4. Y. Benadie, M. Deysel, D. G. R. Siko, V. V. Roberts, S. Van Wyngaardt, S.T. Thanyani, G. Sekanka, A.M.C. Ten Bokum, L.A. Collett, J. Grooten, M.S. Baird, J.A. Verschoor, *Chem. Phys. Lipids* 2008, 152, 95.
5. E. Sabatini, H.O. Finklea, J. Phys. Chem. 91, 1987, 6663.
6. B.O. Agboola, K.I. Ozoemena, *Phys.Chem.Chem.Phys.* 2008, 10, 2399.
7. D. Nkosi, K.I. Ozoemena, *Electrochim. Acta* 2008, 53, 2782.

Chapter 3

Results and Discussion

The subsequent publications resulted from the research work presented in this thesis and are not further referenced.

1. **Nsovo S. Mathebula,** Jeseelan Pillay, Gianna Toschi, Jan A. Verschoor and Kenneth I. Ozoemena, "Recognition of anti-mycolic acid antibody at self-assembled mycolic acid antigens on a gold electrode: a potential impedimetric immunosensing platform for active tuberculosis" *Chem. Commun*. 2009, 3345.
2. Kenneth I. Ozoemena, **Nsovo S. Mathebula,** Jeseelan Pillay, Gianna Toschi, and Jan A. Verschoor, "Electron transfer dynamics across self-assembled N-(2-mercaptoethyl) octadecanamide / mycolic acid layers: Impedimetric insights into the structural integrity and interaction with anti-mycolic acid antibodies" *Phys. Chem. Chem. Phys.* 2010, 12, 345.

3.1 SAM Fabrication: XPS and AFM characterization

The immobilization of mycolic acid and subsequent blocking of the surface to avoid non-specific interaction on gold electrodes are summarized in Scheme 3.2. The initial process of *in-situ* synthesis of MEODA using cysteamine and stearic acid via carbodiimide coupling chemistry (Scheme 3.1) was confirmed using XPS.

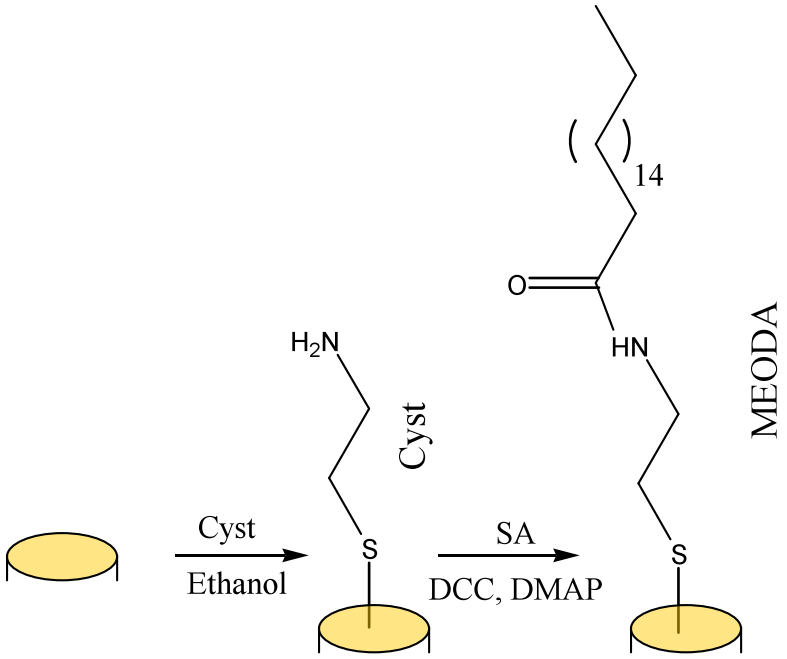

Scheme 3.1: Schematic representation of the synthesis of MEODA using cysteamine and stearic acid via carbodiimide coupling chemistry.

The condensation of the carboxylic acid (–COOH) functional groups of the stearic acid, activated by the DCC, with the amine ($–NH_2$) groups of the cysteamine SAM resulted in the formation of the amide bonds. This type of covalent linkage using the carbodiimide coupling chemistry is well

documented, for example, in linking enzymes and proteins to gold electrodes as SAMs.

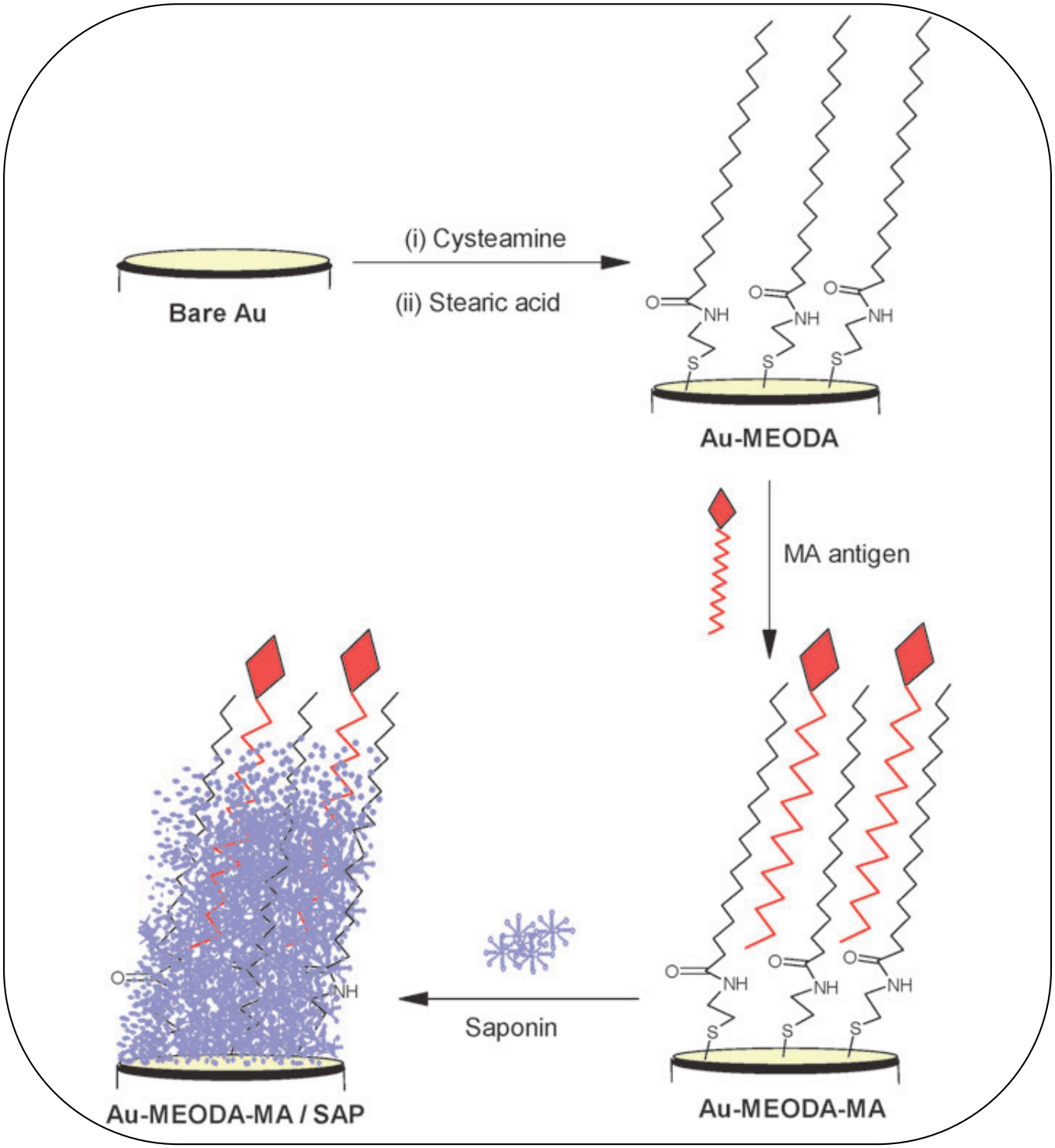

Scheme 3.2: Schematic representation of the Modification of gold electrode with Au-MEODA-MA/SAP.

X-ray photoelectron spectroscopy studies were used to investigate the possible formation of a self assembled monolayer of cysteamine and the subsequent coupling of stearic acid to the cysteamine. Figure 3.1 shows an example of X-ray photoelectron spectra data for Au–Cyst and Au–MEODA obtained at a take-off angle (TOA) of 15^0.

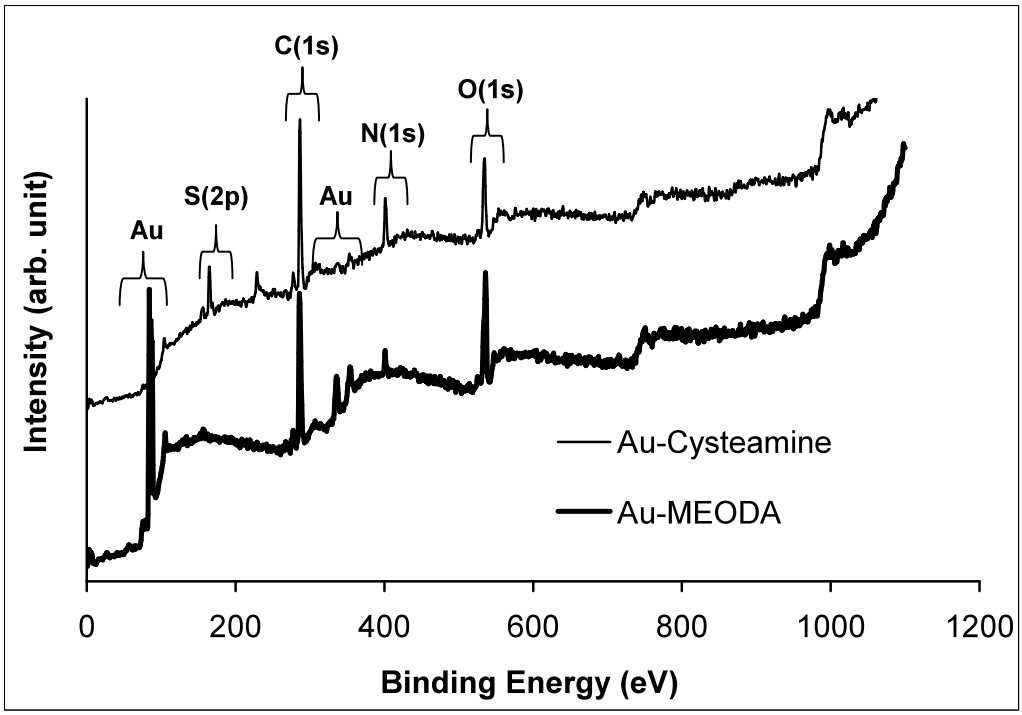

Figure 3.1: Typical comparative X-ray photoelectron spectra Au–Cysteamine and Au–MEODA. The spectrum for the bare Au is omitted for clarity.

The formation of a self-assembled cysteamine monolayer is evident by the gold-bound sulfur (Au–S) peak at 161.5 eV (Fig 3.1) [1, 2]. As can be

seen in figure 3.1, this peak appeared broad for the Au-MEODA, possibly due to reorganization processes in the film brought about by the formation of an amide bond between the gold bound cysteamine and stearic acid. Unlike the bare gold (not shown), the N atom peak is observed at 402 eV, confirming the attachment of the cysteamine and stearic acid via amide bond. In contrast to the bare AU and Au-Cys, the Au-MEODA gave well-resolved peaks at 285.1 eV signifying the presence of sp^3 carbon and 287.7 eV due to $-CH_2-$, $-CH_2-NH-$ and –C-O- species arising from the amide bond (Fig 3.2, Fig 3.1 and Appendix C1).

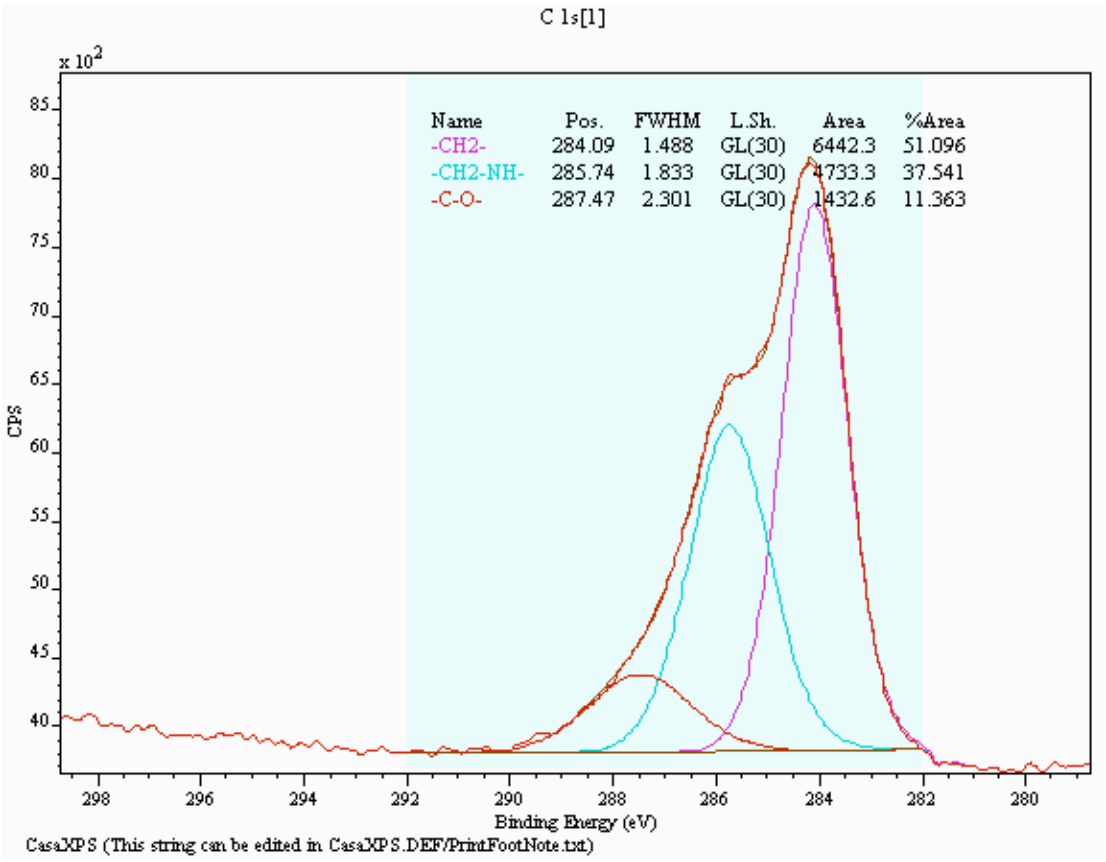

Figure 3.2: Multiplex X-ray photoelectron spectrum for the expanded C1s region of Au-MEODA.

Also, unlike the bare Au and Au-Cys SAM, the Au-MEODA gave an intense oxo-related peaks in the region ranging between 531 to 535 eV due to -CH_2-CO-NH-, H_2O, and -CH_2-O-, further confirming the presence of the amide bond (Fig 3.3, Fig 3.1 and Appendix C2).

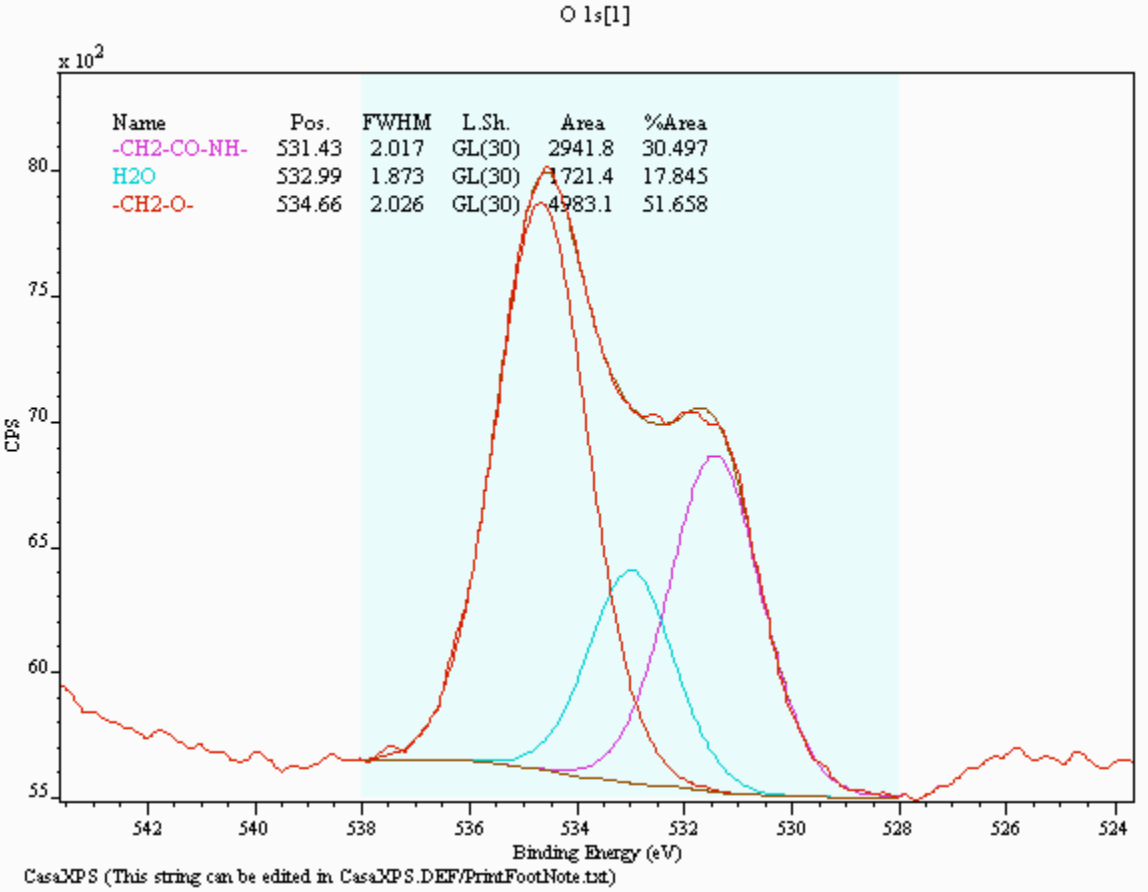

Figure 3.3: Multiplex x-ray photoelectron spectrum for the expanded O1s region of Au-MEODA.

The success of the modification processes was confirmed as well by comparative AFM images of the (a) bare Au, (b) Au–MEODA and (c) Au–MEODA–MA (Fig 3.4). The attachment of MEODA and MA was confirmed by the increase in height from 6.6 nm for the bare Au to 11.8 nm for the Au–MEODA–MA and roughness factor from 0.71 nm for the bare Au to 3.71 nm for the Au–MEODA–MA. From the AFM topography, MEODA–MA appeared as loosely-packed aggregated bundles of species with vertical orientation. MA monolayers are known to exist in differently folded molecular conformations to give a hydrophobic surface [3].

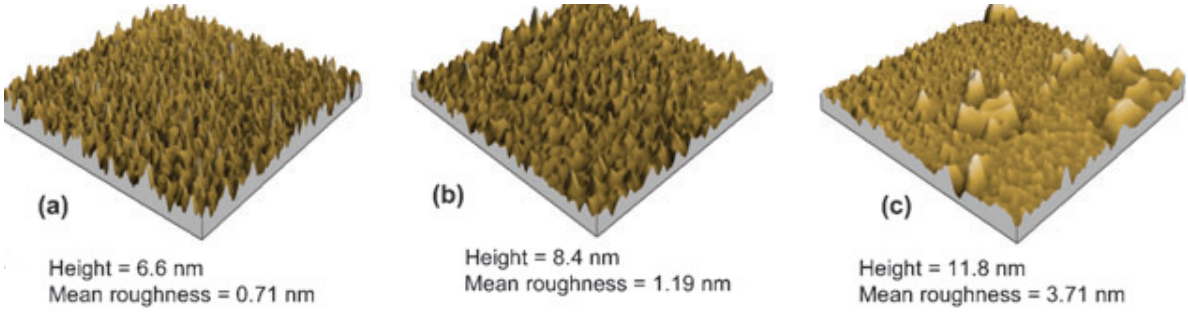

Figure 3.4 Typical comparative AFM micrograph images of (a) bare gold, (b) Au-MEODA and (c) Au–MEODA-MA.

The topography of MA is in close agreement with the work of Hasegawa and co-workers [3, 4], which may be ascribed to the strong Van

der Waal's hydrophobic attractive forces (between the alkyl chains of the MA and MEODA) and some repulsive forces (due to the so-called 'spring-like force' generated by the longer alkyl chain of the MA that has been speculated to be responsible for the highly condensed packing of MA in the cell walls of *M. tuberculosis* [4]). Also, it appears from the comparative 3-D AFM topographies (Figure 3.4.) that the formation of the MEODA-MA created more spaces / pores on the electrode surface, possibly due to the displacement of some of the MEODA. Given the high molecular weight of the MA and the folding behaviour of its long alkyl chains ("W" and "Z" orientations, first referred to by Minnikin and co-workers [5]), it should perhaps not be totally surprising that the pinholes in the MEODA SAM may not be sufficient for the MA to "sit side-by-side" with MEODA without having to either (i) completely detach MEODA from the electrode or (ii) displace or collapse some of MEODA creating defect sites. Given the strong Au-S bond, the latter is the most likely to occur, forming the so-called "collapsed sites" and increasing the distance between the centres of the neighbouring pinholes [6].

3.2 Cyclic voltammetric surface characterisation

Cyclic voltammetry (CV) was first used to establish the extent to which the modifiers (MEODA, MA and SAP) permit electron transport between a

solution redox probe ($[Fe\ (CN)_6]^{4-}$ / $[Fe(CN)_6]^{3-}$) and the underlying gold electrode. Figure 3.5 shows typical comparative CV evolutions of the (i) bare Au, (ii) Au-MEODA, (iii) Au-MEODA-MA and (iv) Au-MEODA-MA/SAP in 1 mM $[Fe(CN)_6]^{4-}$ / $[Fe(CN)_6]^{3-}$ (PBS, pH 7.4). Note that saponin is used to block pinholes or non-specific sites on the Au-MEODA-MA prior to anti-MA antibody detection in TB serum. This is done to avoid non-Mycolic acid antibodies binding to the electrode surface. Each of the steps is expected to form a different surface structure that will increase the thickness of the electrode, blocking the entrance of the test redox probe solution, thereby increasing the resistance to charge-transport.

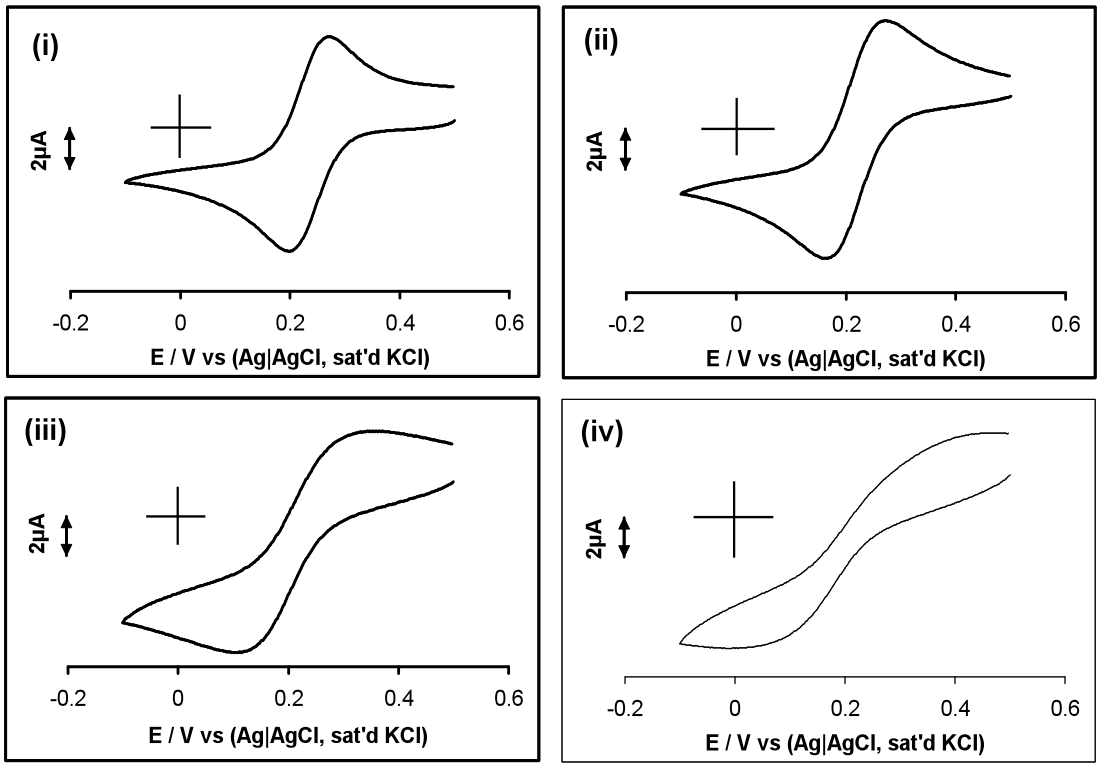

Figure 3.5: Cyclic voltammograms obtained at the (i) bare Au, (ii) Au-MEODA, (iii) Au-MEODA-MA and (iv) Au-MEODA-MA/SAP.

The following need to be emphasized from the data: First, the respective voltammograms did not show any detectable deviations even after 20 repetitive cyclic voltammetric scanning, indicating electrochemical stability. Second, the electrochemical kinetics, demonstrated by the peak-to-peak separation (ΔE_p), decreases as bare Au ($\Delta E_p \approx 56$ mV, typical one-electron transfer kinetics) < Au-MEODA ($\Delta E_p \approx 90$ mV) < Au-MEODA-MA ($\Delta E_p > 160$ mV) < Au-MEODA-MA/SAP ($\Delta E_p > 200$ mV). Ferri/ferro is an outer-sphere redox species with fast electron transport. The decrease in both the ΔE_p and voltammetric peak current densities following the modification of the gold surface clearly indicate that the modifiers provide barrier to electron transfer of the redox species in solution, the barrier increasing with increasing modifier thickness. The changes seen in the CV evolutions may be ascribed to the gradual progression from macro-electrode (planar diffusion) to randomly-spaced microelectrode arrays or sites (radial diffusion). Compton and co-workers elegantly developed a theoretical framework for dealing with voltammetry at spatially heterogeneous electrodes [7-9]. From their work, the voltammogram of the bare Au arises from pure linear diffusion, characteristic of category 1 (naked electrode). The CVs of the modified electrodes describe the behaviour typical of "micro-sized" electro-active zones that are separated with inert blocking materials such that the electrode as a whole behaves like a collection of isolated microelectrodes, each of which experiencing convergent or radial diffusion

that may lead to either type 2 or type 3 phenomenan. In the type 2, the diffusion layer thickness, δ, is larger than the insulating layer but not large enough to permit overlapping of neighbouring diffusion layers. In type 3, the diffusion layer thickness, δ, is larger than the insulating layer such that the neighbouring diffusion layers weakly overlap. Electrochemically, an increase in distance between microscopic sites manifests itself as an increase in the ΔE_p. Third, it is worthy to note here that the long chain MEODA did not effectively block electron-transfer as usually seen of long-chain alkylthiol SAMs. It is well known that long-chain alkanethiol SAMs easily form highly integrated, well packed and pinhole-free SAMs on gold [10, 11]. This weak blockage of the electrode surface by the long-chain MEODA, even after hours-long deposition, is attributed to the spaces / pores created by the presence of the amide bond in its molecular structure, similar to that seen recently by Wilkop *et al.* [12] in their work with the disulfide-terminated hexyl thioctate SAM that contained oxo-containing moieties. Since short-chain alkylthiols SAMs are known for their loose-packing, defects and pinholes, the precursor short-chain cysteamine SAM for the MEODA should be expected to enhance the creation of the pores. These pores within the MEODA SAMs possibly allow for the stable integration of the MA via Van der Waal's attractive forces, typical of long-chain alkane SAMs. Finally, unlike the bare Au and Au-MEODA that gave well defined peaked voltammograms (typical of linear / planar diffusion at macro-electrodes), Au-MEODA-MA and

Au-MEODA-MA/SAP exhibited somewhat sigmoidal-shaped voltammograms (typical of radial diffusion at microelectrodes). The assumption of sigmoidal shapes indicates that electron-transfer processes take place at pinhole sites [6, 13-15], responsible for the diffusion or permeation of the solution species into the underlying electrodes (pinhole analysis is later discussed in section 3.4 below).

3.3 Impedimetric surface characterization

EIS provides important insights into the integrity and properties of electrochemical systems, and is less perturbing (smaller applied potential ≤ 10 mV) than CV, which is particularly very crucial to the soft materials studied in this work. Thus, all subsequent studies, unless otherwise stated, were performed with EIS. The EIS measurements were performed in the $[Fe(CN)_6]^{4-}$/ $[Fe(CN)_6]^{3-}$ solution as in CV experiments (Figure 3.5) at the formal potential ($E_{1/2} \approx 200$ mV). Comparative Nyquist (Figure 3.6) and Bode plots (Figure 3.8) provide a clearer picture of the electron transfer processes than seen in the CV evolutions (Figure 3.5).

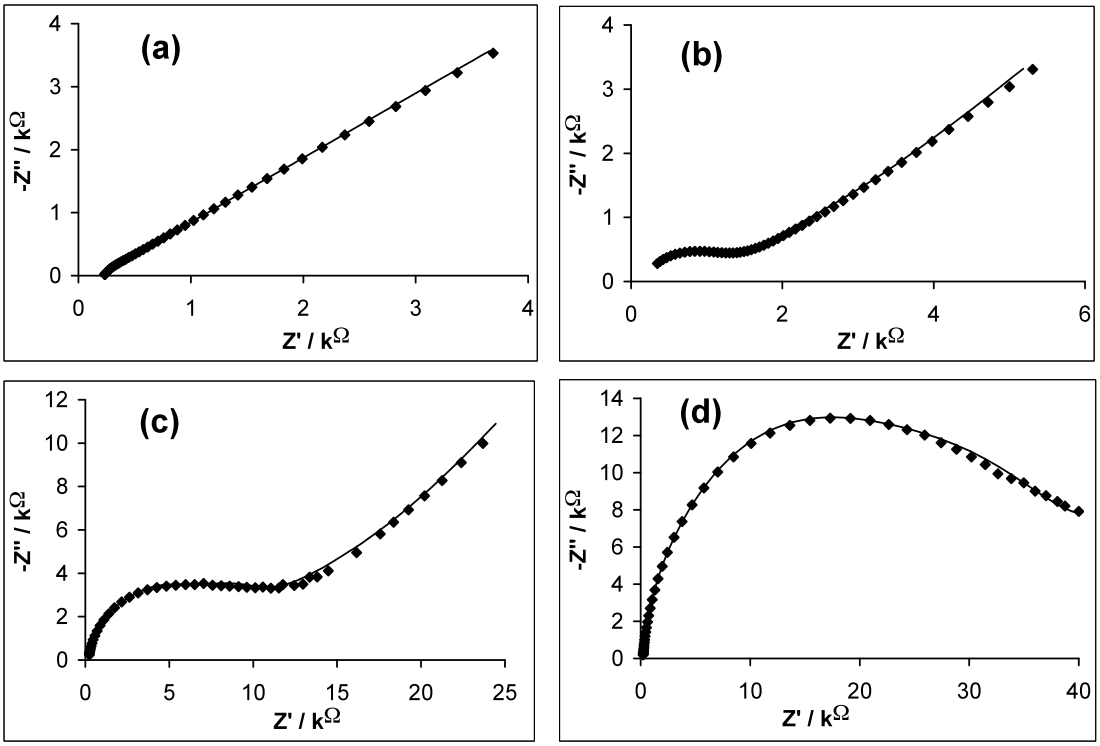

Figure 3.6: EIS Nyquist plots for MA antigen immobilization. Shown are the (a) bare Au, (b) Au-MEODA, (c) Au-MEODA-MA and (d) Au-MEODA-MA/SAP. The symbols represent the experimental data, while solid lines are fitted curves using equivalent circuits shown in Figure 3.7.

An essential aspect of EIS is the ability to fit the spectral data with some theoretical electrical equivalent circuit models. As seen in figure 3.7 and Table 3.1, the bare gold electrode was satisfactorily fitted with the modified Randles equivalent circuit (Figure 3.7a), while the Au-MEODA, Au-MEODA-MA and Au-MEODA-MA-SAP were fitted with Randles circuit incorporating Voigt circuit of two or three RC elements in series, equivalent circuits (Figure 3.7b), (Figure 3.7c) and (Figure 3.7d) respectively. The fitting parameters involve the electrolyte resistance (R_s), electron-transfer

resistance (R_{ct}), constant phase element (CPE) due to the inherent roughness of the electrode (a real system) rather than pure double layer capacitance (C_{dl}) expected for an ideal system, and Warburg-type impedance (Z_w) which is associated with the diffusion of the ions of the redox probe. Generally, the Nyquist plots exhibited the characteristic semicircles at high frequencies and a straight line at low frequencies, corresponding to kinetic and diffusion processes, respectively.

The apparent electron-transfer rate constant (k_{app}) values of the electrodes were obtained from the equation:

$$k_{\text{app}} = \frac{RT}{n^2 F^2 A R_p C} \qquad 3.1$$

where n is the number of electron transferred, A is the experimentally-determined area of the electrode, R_p is effective charge transport resistance or polarization resistance obtained by the summation of the charge-transfer resistances in series connection, C is the concentration of the $[Fe(CN)_6]^{3-}$ (in mol cm^{-3}, the concentration of $[Fe(CN)_6]^{3-}$ and $[Fe(CN)_6]^{4-}$ are equal), R is the ideal gas constant, T is the absolute temperature (K) and F is the Faraday constant. The calculated values are shown in Table 3.1.

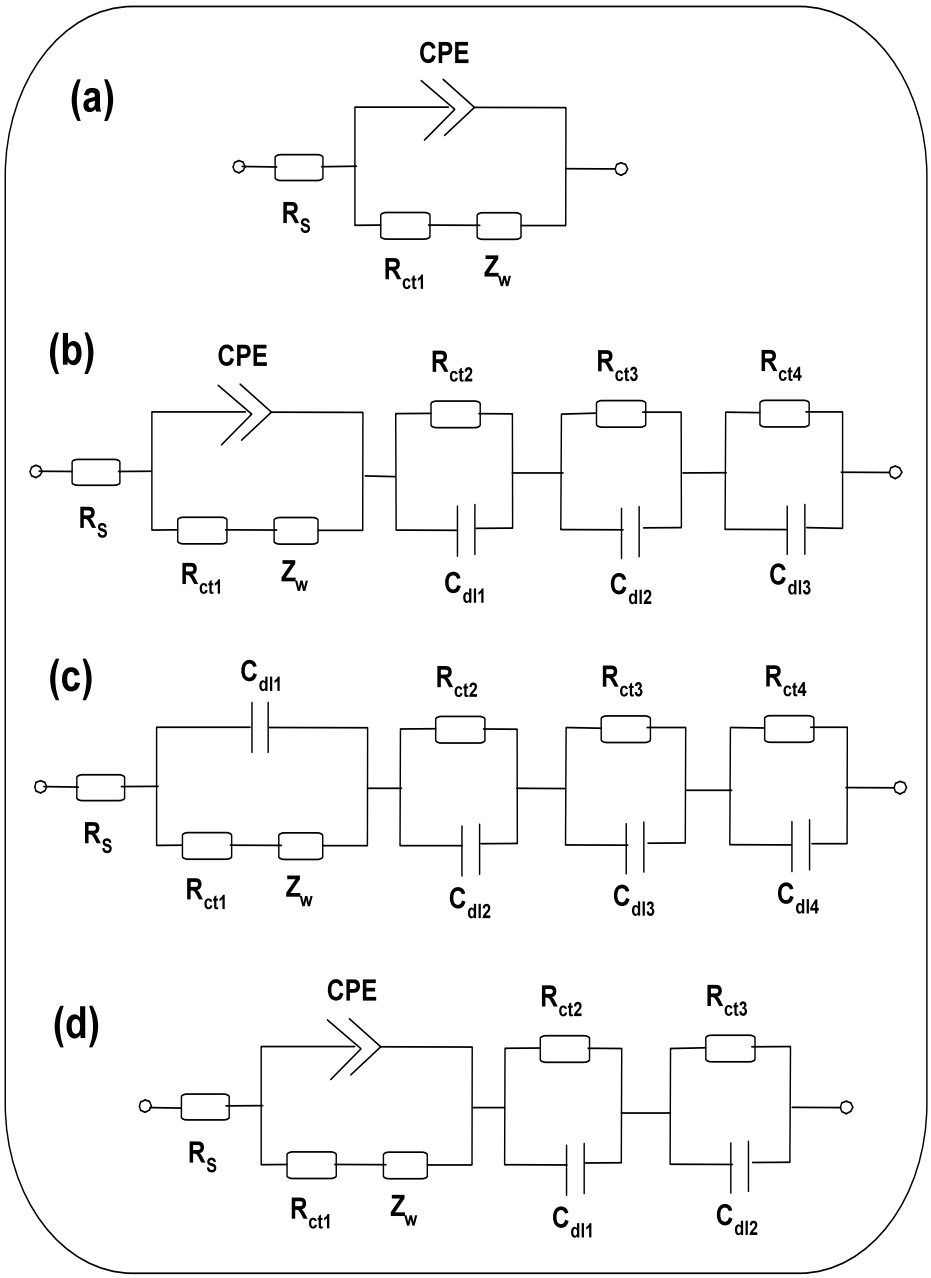

Figure 3.7: Respective equivalent circuit model used to fit the impedance spectrum of (a) bare Au, (b) Au-MEODA, (c) Au-MEODA-MA and (d) Au-MEODA-MA/SAP.

The k_{app} values decreases as: bare Au (4.23 x 10^{-2} cm^2 s^{-1}) < Au-MEODA (5.13 x 10^{-3} cm^2 s^{-1}) < Au-MEODA-MA (7.01 x 10^{-4} cm^2 s^{-1}) < Au-MEODA-MA-SAP (1.85 x 10^{-4} cm^2 s^{-1}) indicating that electron transfer processes between the redox probe and the underlying gold surface are made more difficult with increasing layers of modifier, excellently corroborating the ΔE_p results from the CV experiment. The impedance of the CPE (Z_{CPE}) is defined as (equation 3.2):

$$Z_{\mathrm{CPE}} = \frac{1}{[Q(j\omega)^n]} \qquad 3.2$$

where Q is the frequency-independent constant relating to the interface, j = $\sqrt{-1}$, ω is the radial frequency, the exponent n arises from the slope of log Z vs log f (and has values $-1 \leq n \leq 1$). If $n = 0$, the CPE behaves as a pure resistor; $n = 1$, CPE behaves as a pure capacitor, $n = -1$ CPE behaves as an inductor; while $n = 0.5$ corresponds to Warburg impedance (Z_w) which is associated with the domain of mass transport control arising from the diffusion of ions. Generally speaking, CPE may occur as a result of several factors [16] including (i) the nature of the electrode (e.g., roughness and polycrystallinity), (ii) distribution of the relaxation times due to heterogeneities existing at the electrode/electrolyte interface, (iii) porosity and (iv) dynamic disorder associated with diffusion. From table 3.1, n ≥ 0.78, meaning pseudocapacitive behaviour. From the Bode plots (figure 3.8), the slopes of the log Z vs log f plot at the mid frequency region are less

than the ideal −1.0 for pure capacitive behaviour, which is indicative of pseudocapacitive behaviour. Also, from the other Bode plot (i.e., −phase angle *(ϕ)* vs log f) the phase angles are less than the 90° expected of an ideal capacitive behaviour, confirming the pseudocapacitive behaviour.

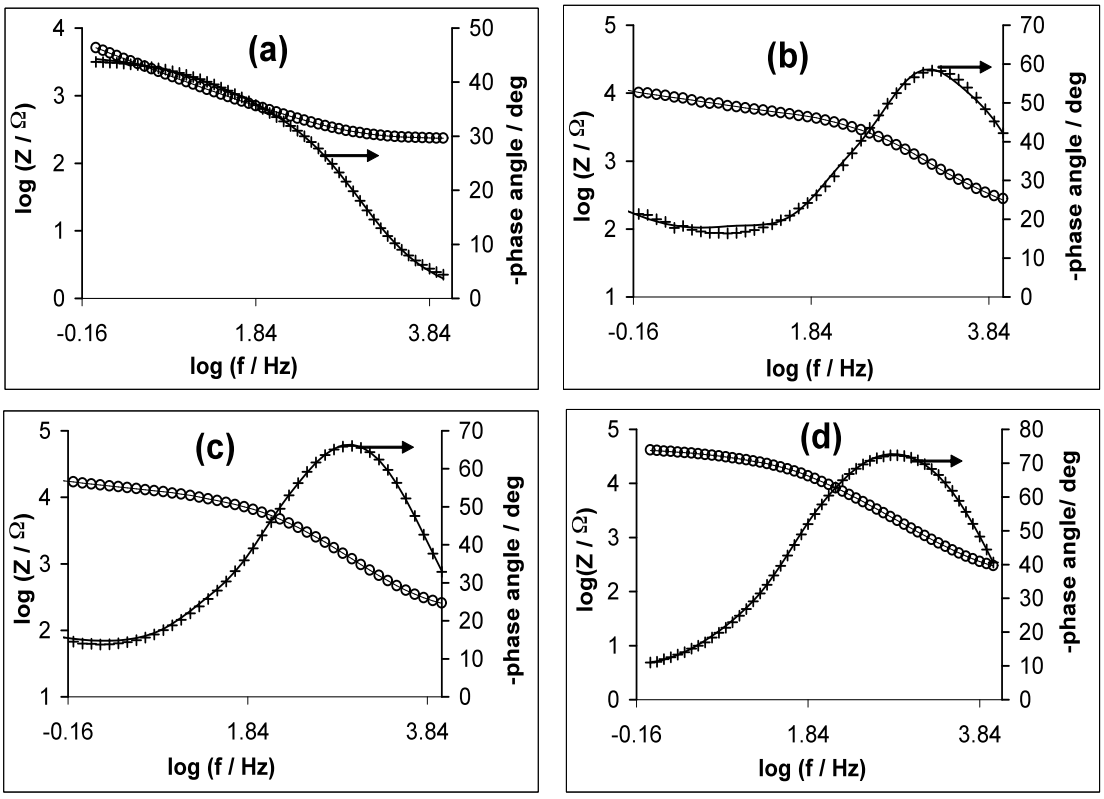

Figure 3.8: EIS Bode plots for the MA antigen immobilization. Shown are (a) bare Au, (b) Au-MEODA, (c) Au-MEODA-MA and (d) Au-MEODA-MA/SAP. The symbols represent the experimental data, while solid lines are fitted curves using equivalent circuits shown in Figure 3.7.

The following features shown by the comparative impedimetric data of the bare Au, Au-MEODA, Au-MEODA-MA and Au-MEODA-MA/SAP should be emphasized. First, every attempt to fit the other electrodes with the ideal or

modified Randles circuit or a simple one-reaction RC time constant circuit was unsuccessful as very large fitting error values were obtained. The non-ideal behaviour of each of the semi-circular arcs of the Au-MEODA and Au-MEODA-MA and Au-MEODA-MA/SAP (i.e., departure from a single arc centred on the real axis of Z') and the inability to fit these arcs by a single electrochemical reaction time constant, prompted the speculation that there was an occurrence of a variety of physico-electrochemical phenomena involving more than one RC time constants, notably, multiple or coupled reaction sequences, to roughening of the electrode, and to frequency-dependent ohmic resistances caused by non-uniform charging of the electrode/electrolyte double layer.

Table 3.1: Electrochemical impedance data obtained for the electrodes

EIS paramete c v n,m. m	**Electrode[1]**			
	Bare-Au	**Au-MEODA**	**Au-MEODA-MA**	**Au-MEODA-MA/SAP**
R_s/Ω	230.7 (0.25)	254.4 (2.86)	183 (1.98)	190.3 (1.03)
C_{dl1} /μF		2.154 (8.39)		
CPE /μF	3.27 (13.00)		0.24(3.75)	1.67 (9.91)
n	0.893 (1.48)		0.89 (0.51)	0.78 (1.00)
R_{ct1} / kΩ	0.229 (10.53)	0.716 (5.21)	5.82 (3.68)	24.35 (1.41)
Z_w / $\mu\Omega^{-1}$	77.6 (0.69)	83.5 (1.34)	85.5 (2.72)	74.3 (8.77)
R_{ct2} / kΩ		0.547 (5.37)	2.46 (11.42)	2.32 (16.13)
C_{dl2} /μF		0.383 (12.39)	113.4 (16.03)	0.439 (9.33)
R_{ct3} / kΩ		0.628 (4.80)	3.02 (6.47)	13.05 (3.92)
C_{dl3} /μF		0.0624 (2.59)	1.23 (11.63)	268.8 (4.68)
R_{ct4} / kΩ			2.57 (7.84)	12.64 (4.90)
C_{dl4} /μF			9.08 (17.92)	
k_{app} / cm^2 s^{-1}	(4.23±0.45) x 10^{-2}	(5.13±0.79) x10^{-3}	(7.01±1.9) x10^{-4}	(1.85±0.48) x10^{-4}

1. The value in parenthesis represents the relative percent error obtained from fitting the impedance spectrum using the proposed equivalent circuits (Fig 3.7).

As evident from the experimental impedance spectra (Nyquist (Figure 3.6) and Bode plots (Figure 3.8) of the Au-MEODA, Au-MEODA-MA and Au-MEODA-MA/SAP exhibited excellent fitting with equivalent electrical circuit models involving Voigt circuit of two or more RC elements in series with the Randles circuit, confirming that the impedance data are influenced by distributed-time-constant phenomena [17]. Simply stated, each of these semi-circular arcs comprised of overlapping arcs due to close proximity of time constants. These time constants are so close that it is even impossible to observe them as more than one peak in their respective Bode plots.

Second, impedance spectra are known to contain features that could be directly related to microstructures, with the grain boundary phases of microstructures having a dominant blocking effect on the impedance spectra [17, 18]. As seen from Table 3.1, the use of the "ideal" double layer (C) rather than CPE (which is an acceptable real practical situation) led to a more satisfactory fitting (signified by the fitted line and % relative errors). Since electron transport processes occurring via permeation of the redox probe through the spaces created by the assembled species is expected to be faster than that arising through the layers [19], One may therefore associate the Randles circuit component of the equivalent circuits to processes that occur through the spaces amongst the self-assembled molecular layer, while the Voigt elements (R_{ct2}/C_{dl2}, R_{ct3}/C_{dl3} and R_{ct4}/C_{dl4}) are attributed to the electron transfer and specific capacity of the interface

arising from the collapsed sites and/or the grain boundaries within the film structure. This is in agreement with the proposal by Finklea *et al*. [20] that there are sites at which the redox couple can approach the underlying electrode surface more closely but not able to come into contact with it.

Third, it is known that time-constant (or frequency) dispersion leading to CPE behaviour occurs as a result of distribution of time constants along either the area of the electrode surface (involving a 2-dimensional aspect of the electrode) or along the axis normal to the electrode surface (involving a 3-dimensional surface) [21]. One of the recognized sources of 2-D distribution is surface heterogeneities (such as grain boundaries, crystal faces of polycrystalline electrode, or other variations in surface properties), whereas 3-D distribution is usually associated with changes in the conductivity of oxide layer or from porosity or surface roughness [22]. Importantly, unlike a 3-D distribution, a 2-D distribution shows an ideal RC behaviour, meaning that impedance measurements are very useful in distinguishing whether the observed global CPE behaviour is due to a 2-D distribution, from a 3-D distribution, or from a combined 2-D and 3-D distributions [21]. One may therefore conclude that the observed impedimetric behaviour of the Au-MEODA is due mainly to 2-D distribution while that of the Au-MEODA-MA is a combination of 2-D and 3-D distributions. Note that despite the fitting of the spectra with ideal RC element, the phase angles seen on the Bode plots deviate from the ideal –

90^{o} expected of a pure RC, which further confirms that the presence of the 2-D distribution arise from CPE behaviour. The microstructure model is a complex model that has been a subject of extensive mathematical theories [18]. Some of the well known micro-structural systems that exhibit grain/grain boundary impedance spectra include oxides and liposomes. Thus, at the moment, it may be reasonable to speculate that the self-assembled MEODA, MEODA-MA and MEODA-MA/SAP species exhibit micro-structural behaviour with the relaxations (time-constants) corresponding to possible orientations of these microstructures.

3.4 Impedimetric assessment of structural disorder

Returning to the discussion on pinholes, an important parameter to probe the adsorption kinetics of monolayers by electrochemical method is the fractional coverage (θ). The presence of pinholes or defect sites on redox-inactive SAMs responsible for the diffusion or permeation of the solution species into the underlying electrodes, as in this work, is the consequence of disorderly-packed SAMs, and is best interrogated using EIS technique.

Assuming that electron-transfer processes occur only at the bare spots of the electrodes and that diffusion of the redox probe to these defect sites is planar, the apparent fractional coverage (θ_{app}) of the modifier was first estimated from equation 3.3 [23, 24]:

$$\theta_{app} = 1 - \left(\frac{R_{ct}^{Au}}{R_{ct}^{SAM}} \right) \qquad 3.3$$

Where θ_{app} is the fractional coverage of the surface, R_{ct}^{Au} and R_{ct}^{SAM} are the charge transfer resistance of the bare gold and the self assembled monolayer modified gold surface respectively. When equation 3.3 was used to calculate the coverage, the θ_{app} was found to be greater than 0.9. However, according to Amatore *et al*., [6] equation 3.3 is not appropriate for describing fractional coverage if θ_{app} > 0.9. In this case, another model that takes cognizance of radial diffusion or microelectrode array behaviour, radial size of the pore/pinhole and their distribution in the SAM was employed; equation 3.4 [25]:

$$\theta_{app} = 1 - \left(\frac{\sigma_W}{m - \sigma_W} \right) \qquad 3.4$$

where σ_W is the Warburg coefficient (225.3 $\Omega s^{-1} cm^2$) calculated for the clean bare gold electrode via the slope of the linear *Z'* vs $\omega^{-1/2}$ plot obtained in the low frequencies region (Fig 3.9), while *m* is the slope of the linear interval in the high frequency regions of the *Z'* vs $\omega^{-1/2}$ (Fig 3.10a-c) function obtained at the respective modified electrodes. Thus, using equation 3.4, the θ_{app} values for the Au-MEODA, Au-MEODA-MA and Au-MEODA-MA/SAP were essentially the same (*ca.* 0.97). The radius of the pinhole (r_a) was estimated using equation 3.5 [26]:

$$r_a^2 = \frac{D}{0.36q} \qquad 3.5$$

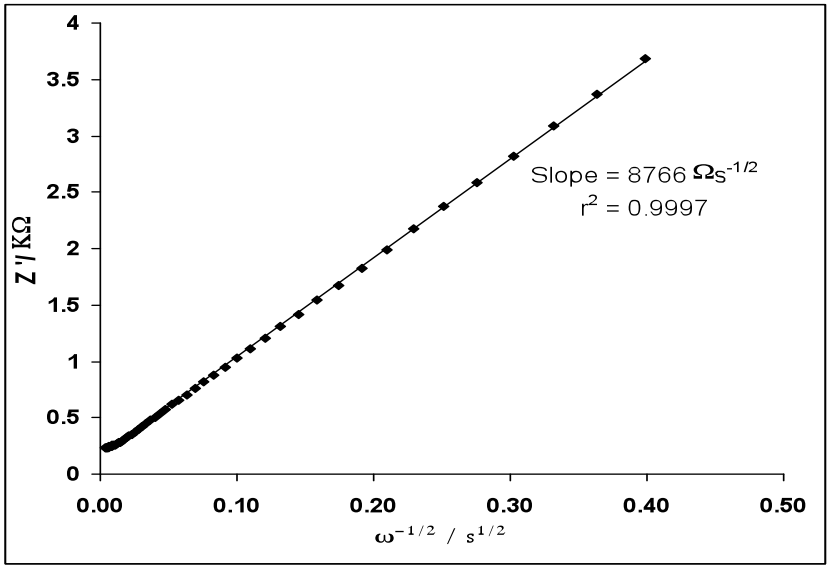

Figure 3.9: EIS plot of *Z′* vs ω-$^{1/2}$ for bare Au.

where *D* is the diffusion coefficient of the redox couple, assuming Do ≈ Dr ≈ 7.6 x 10^{-6} cm^{2}s^{-1} [27], and *q* is the so-called "transition radial frequency", corresponding to the turning point between the high- and low-frequency domains in the *Z′* vs ω -$^{1/2}$ plots, which can be determined from the maximum in the *Z″* vs ω -$^{1/2}$ plot of the respective modified bare Au electrodes (Figure 3.10a-c) using equation 3.6 [28]:

$$\omega = \frac{q}{2} \qquad 3.6$$

The radius of the inactive domain surrounding the microelectrode (r_b, i.e., half the distance between the centres of the neighbouring pinholes) is obtained from equation 3.7 as [25, 29]:

$$1 - \theta_{app} = \frac{r_a^2}{r_b^2} \qquad 3.7$$

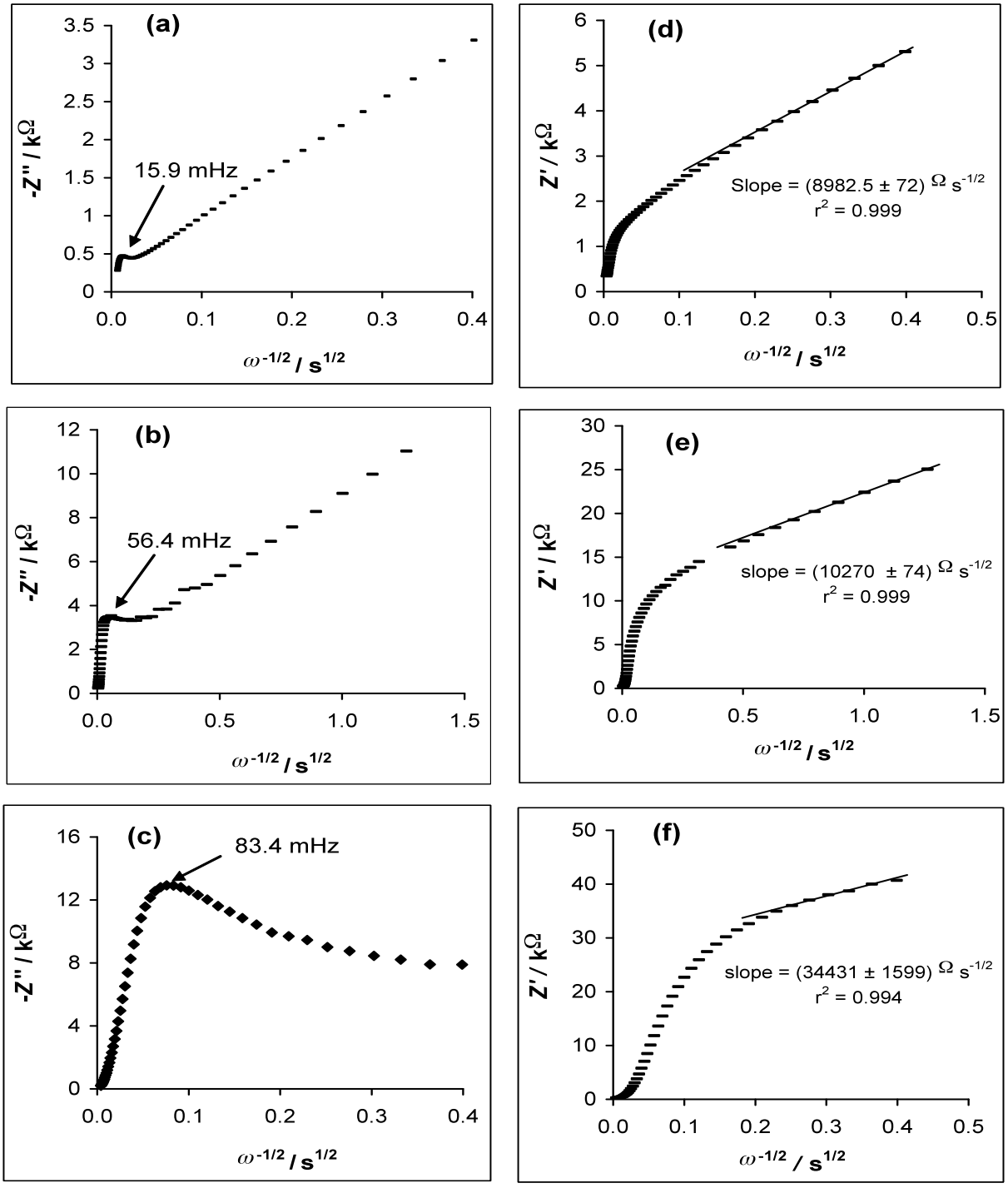

Figure 3.10: EIS plots of *Z* vs ω-$^{1/2}$ for MA antigen immobilization. *Z′* vs ω-$^{1/2}$ (left panel, a - c) and *Z″* vs ω-$^{1/2}$ (right panel, d- f) of the Au-MEODA (a, d), Au-MEODA-MA (b, e) and Au-MEODA-MA/SAP(c, f).

Figure 3.11 is a plot of the r_a and r_b versus the modified electrodes. The r_a values are almost independent of the modifier, they increased slightly from the Au-MEODA (0.84 μm) to Au-MEODA-MA (1.73 μm) and to the Au-MEODA-MA/SAP (3.50 μm) compared to their r_b counterparts that increased from Au-MEODA (4.68 μm) to Au-MEODA-MA (10.69 μm) and to the Au-MEODA-MA/SAP (41.98 μm). According to literature [25, 26, 30], such insignificant increase in the r_a values suggests transformation of some pinholes to collapsed sites, while the significant increase in the r_b values indicates the disappearance of some of the original pinholes. Simply stated, in the MEODA SAM, for instance, MA could bind to some pinhole defect sites of the MEODA and make them disappear, thereby increasing the pinhole separation.

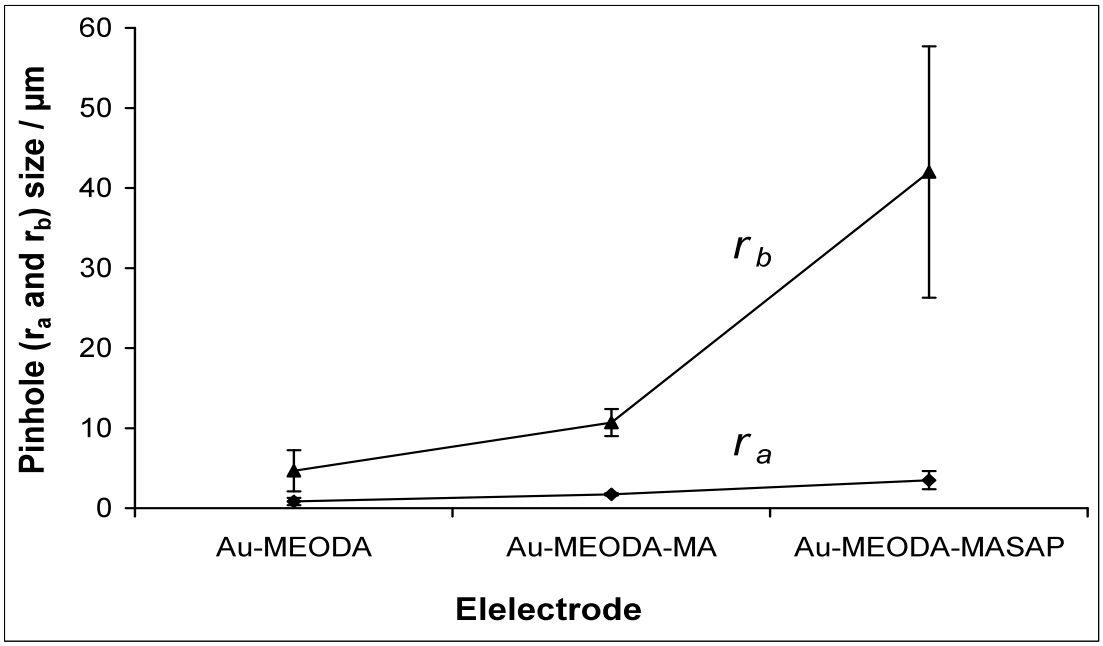

Figure 3.11: Comparative plots of the r_a and r_b of the Au-MEODA, (ii) Au-MEODA-MA and (iii) Au-MEODA-MA/SAP.

If electron-tunneling across an insulating barrier is involved in electron transfer process, then the redox current at any potential should decrease exponentially with the barrier thickness according to equation 3.8 [11,30]:

$$I = I_0 e^{-\beta d} \qquad 3.8$$

where I_o is the current obtained at the bare gold electrode, β is the electron-tunnelling coefficient (β = 1.05 per methylene group [31]), and d is the thickness of the monolayer film. Under equilibrium conditions, equation 3.8 may be expressed as equation 3.9 [11]:

$$k = k_0 e^{-\beta d} \qquad 3.9$$

where k_o and k are the standard electron transfer rate constants at the bare and film-modified gold electrodes, respectively. Given that equation 3.9 implies that electron transfer constant at thick film is much less than that across thin film, it is possible to compare the theoretical and experimental electron transfer rate constants to determine the existence of collapsed sites. If the apparent electron transfer rate constant (k_{app}) obtained from the Au-MEODA (experimental value) is much larger than the theoretical electron transfer rate constant, it can be concluded that collapsed sites do really exist in the MEODA, and most certainly in MEODA-MA and MEODA-MA/SAP. The k_{app} values were determined as before using equation 3.1. For an ideal Au-MEODA SAM (i.e., free of collapsed sites, all MEODA species standing upright), d is a 21-methylene group long (i.e., assuming a 2-methylene for the amide bond). If one assumes k_o = 0.031 cm s^{-1} for the $[Fe(CN)_6]^{3-/4-}$ redox system [7-9,30], and applying equation 10, k is calculated as 8.23 x 10^{-12} cm s^{-1}. Since this theoretical value is about 9 orders of magnitude lower than the k_{app} of 5.13 x 10^{-3} cm s^{-1} for Au-MEODA, it clearly confirms the existence of collapsed sites at the Au-MEODA and that, in addition to the direct permeation of the redox probe into the active sites of the bare gold electrode, electron tunneling through the films or collapsed, "down-lying" MEODA and MA molecules contribute to the observed Faradaic current.

3.5 Impedimetric assessment of the MA / anti-MA antibody interactions (Serum dilution used in this section, 1: 1000)

Scheme 3.3 is a representation of the interaction mechanism of the anti-MA antibody in TB positive serum with the MA-modified gold electrode. One of the main advantages of EIS as an electro-analytical tool is its sensitivity to structure, be that the structure of a solid or a liquid [22].

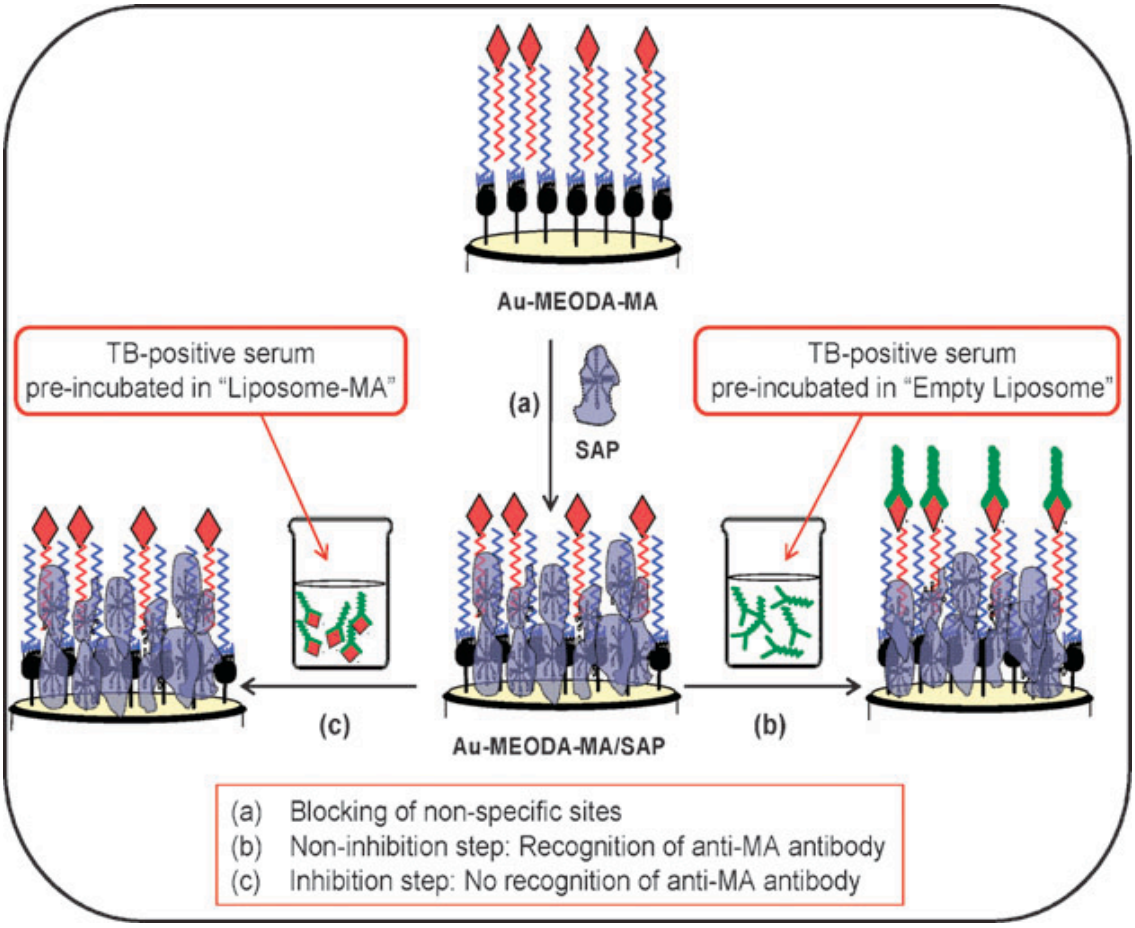

Scheme 3.3: Cartoon representation (not drawn to scale) of the modification of a Au–MEODA–MA electrode with a blocking agent (saponin, SAP) and subsequent interaction of the immobilized MA with anti-MA antibody in human TB-positive serum.

Figure 3.12a shows the EIS evolutions (Nyquist plots) obtained for the Au-MEODA-MA/SAP before (i) and after (iii) it was exposed to a TB positive patient serum dilution (1:1000) pre-incubated with empty liposomes. Plot (ii) is the control experiment of the same TB positive patient serum that was pre-incubated with MA containing liposomes. Figure 3.12b shows the same, but obtained with TB negative patient serum. As expected, the TB positive patient serum effects better blocking behaviour towards the Au-MEODA-MA/SAP electrode compared to the TB negative serum. Pre-incubation with the soluble MA antigen in liposomes reduced the blocking behaviour of the TB positive patient serum by preventing the antibodies from binding to the surface immobilized MA. This was much less prominent in the TB negative patient serum case, as expected.

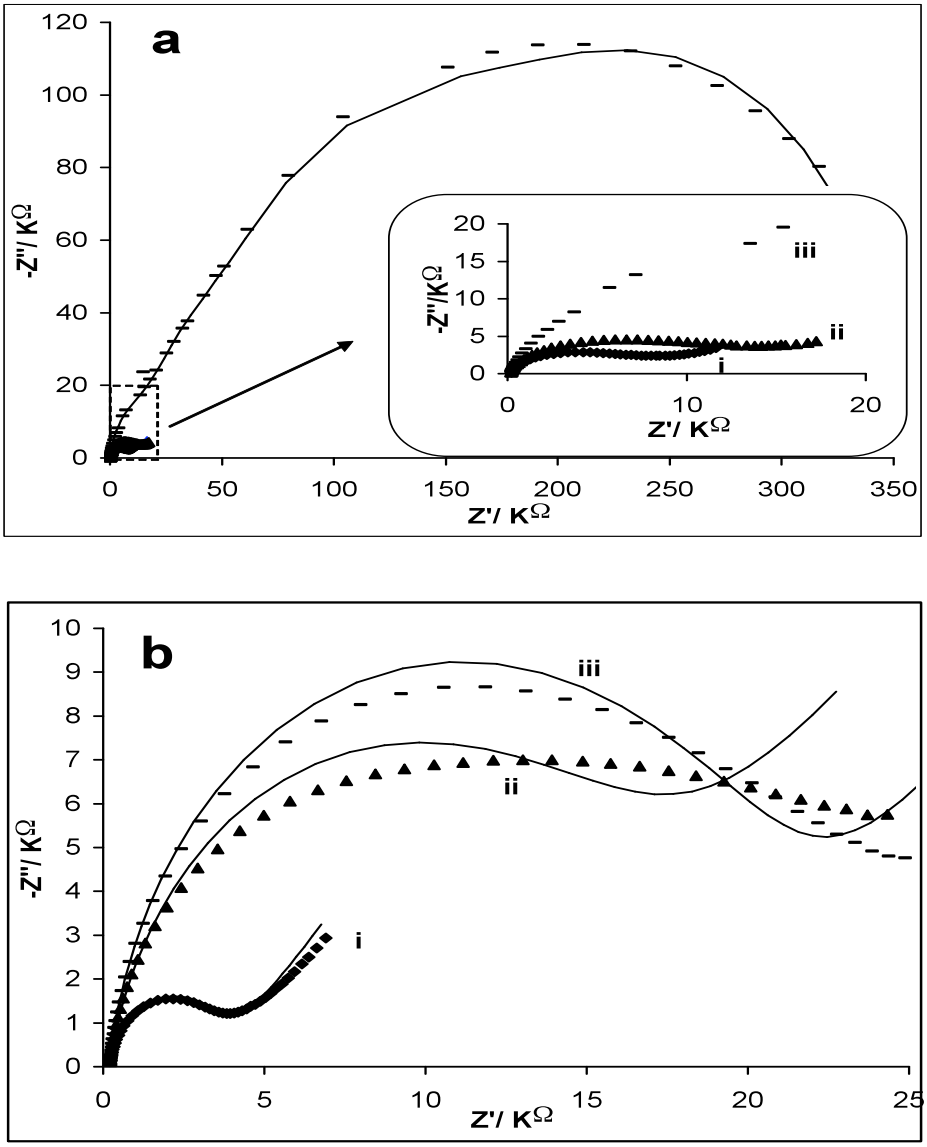

Figure 3.12: Nyquist plots for the Au-MEODA-MA/SAP before (i) and after (iii) exposure to human serum (1:1000 dilution) that was pre-incubated with empty liposomes. (ii) The control experiment of the same serum that was pre-incubated with liposomes containing MA. (a) The Nyquist plots for a human serum from a patient that was TB positive (b) The Nyquist plots for a human serum from a patient that was TB negative. The symbols represent the experimental data, while solid lines are fitted curves using equivalent circuits shown in Figure 3.7d (TB negative patient) and 3.13 (TB positive patient)

Upon interaction of the Au-MEODA-MAP/SAP with the $HIV^{+}TB^{+}$ serum, the spectrum was best fitted with a Voigt circuit model comprising four RC elements in series (Fig 3.13), which is characteristic of blocking/inhibition behaviour, with a solution resistance (R_s), confirming that the impedance data are influenced by distributed-time-constant phenomena.

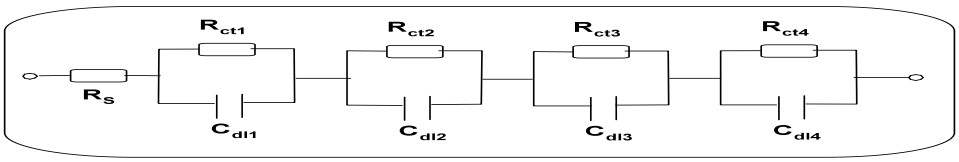

Figure 3.13: Voigt circuit model used to fit the impedance spectrum of Au-MEODA-MA/SAP with the $HIV^{+}TB^{+}$ serum.

In other words, the poorly resolved arc observed at the TB positive serum comprised overlapping arcs due to close proximity of time constants. This is further confirmed from the Bode plots (Fig 3.14ii and 3.14iv), where four peaks corresponding to four relaxation processes (72.9° at 1995 Hz, 72.8° at 316 Hz, 50.1° at 10 Hz and 35.4° at 0.63 Hz) are observed.

Although the double layer (C_{dl1} – C_{dl4}) was used in the fitting circuit, the phase angles were < 90°, meaning that the $C_{dl} \approx$ CPE [17]. It may thus

be concluded that the observed impedimetric behaviour of the $HIV^{+}TB^{+}$ serum arose mainly from a 2-D distribution.

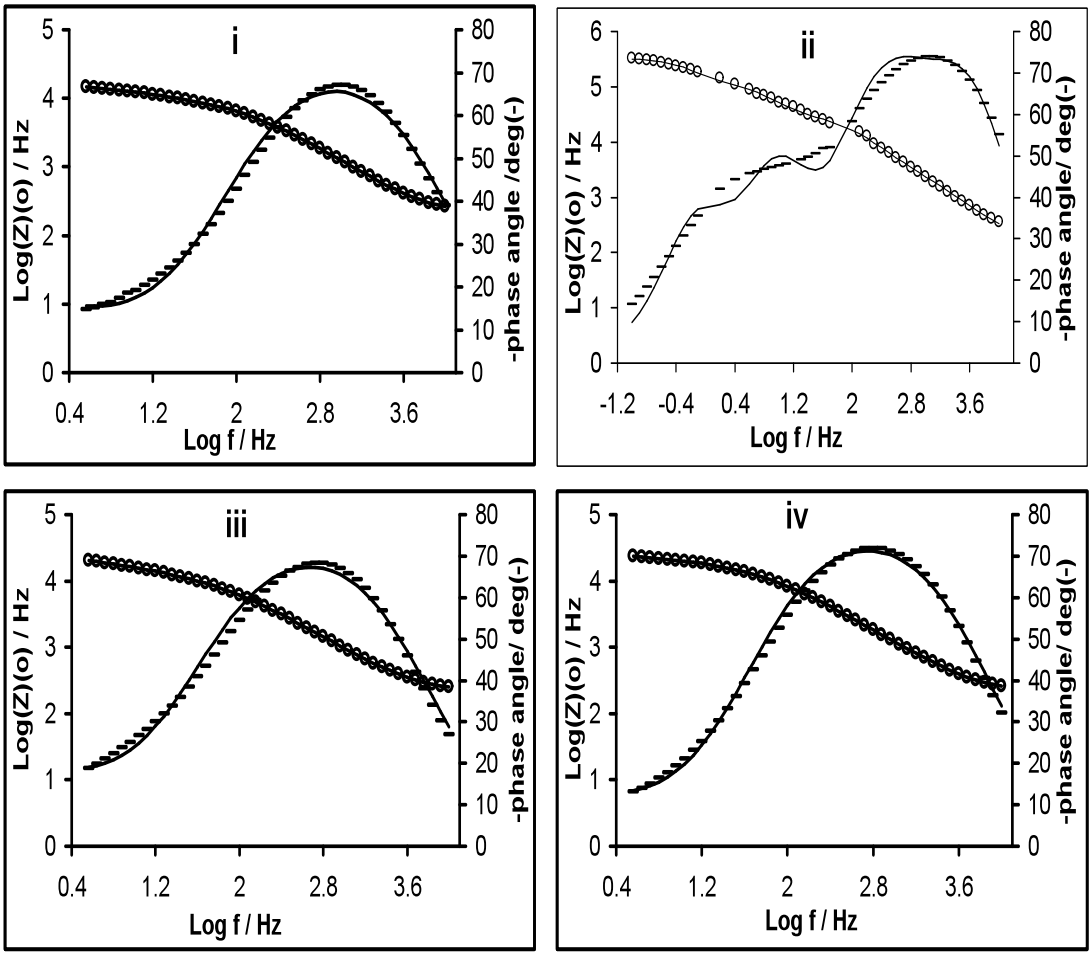

Figure 3.14: Bode plots for the same experiments shown as Nyquist plots in Figure 3.12 The symbols i and ii, Au-MEODA-SAP with $HIV^{+}TB^{+}$ serum pre-incubated with Mycolic acid liposomes and empty liposomes respectively; iii and iv, Au-MEODA-SAP with $HIV^{-}TB^{-}$ serum pre-incubated with Mycolic acid liposomes and empty liposomes respectively. The solid lines are fitted curves using equivalent circuits shown in Figure 3.13 for the Au-MEODA-SAP with $HIV^{+}TB^{+}$ serum pre-incubated in empty liposomes and 3.7d for the other electrodes.

Unlike the other electrodes, the relaxations are more discernible in the Bode plots (Fig 3.14). The EIS data are summarised in Table 3.2. The values of polarization resistances at the Au-MEODA-MA/SAP electrode incubated in TB positive serum (294 kΩ) is about 18 times higher than those of the electrodes incubated in the TB-negative sera (16 kΩ) or the electrodes that did not undergo any incubation in either of the TB-positive or negative serum (4 kΩ).

Table 3.2: Electrochemical impedance data obtained for the Au-MEODA-MA/SAP electrode upon interaction with TB+/HIV+ serum

EIS Paramete	**Au-MEODA-MA/SAP-serum**
R_s/Ω	198.2 (7.09)
CPE /nF	208 (11.9)
R_{ct1} / kΩ	0.761 (28.3)
R_{ct2} / kΩ	73.8 (6.75)
C_{dl} /nF	460 (6.61)
R_{ct3} / kΩ	19.42K (6.68)
C_{dl3} /μF	109 nF (5.28)
R_{ct4} / kΩ	230.9 (4.15)
C_{dl4} /μF	1.634 (8.97)

[1]Value in parenthesis represents the relative percent error obtained from fitting the impedance spectrum using the proposed equivalent circuit shown in figure 3.13.

This simply means that electron transfer between the redox probe and the gold substrate is most inhibited following interaction of the electrode with the anti-MA antibodies present in the TB positive serum. Note that the main difference between the equivalent electrical circuit used to fit the TB positive spectrum (Table 3.2) and others (Table 3.1) is the absence of the Warburg (Z_w) element, indicating an efficient blockage of diffusion of the redox probe ions. It also confirms the presence of anti-MA antibodies in the human serum and interaction of these antibodies with the immobilized MAs. This result suggests that the mechanism underlying the interaction of the MA-modified electrode with the TB positive serum is the modification of the electrode to act as an ionic insulator that is virtually defect-free, capable of strongly suppressing the penetration of the redox probe into the underlying gold electrode.

3.6 Serum concentration studies

Figure 3.15 shows typical impedance spectral data obtained after immersing the electrodes in different concentrations of the human sera for HIV^+TB^+ patient, fitted with equivalent circuits shown in Figure 3.13. The HIV^+TB^+ patient sera showed complete blockage of diffusion, indicating the binding of the anti-MA antibodies in the sera and the interaction of these antibodies with the immobilized MA.

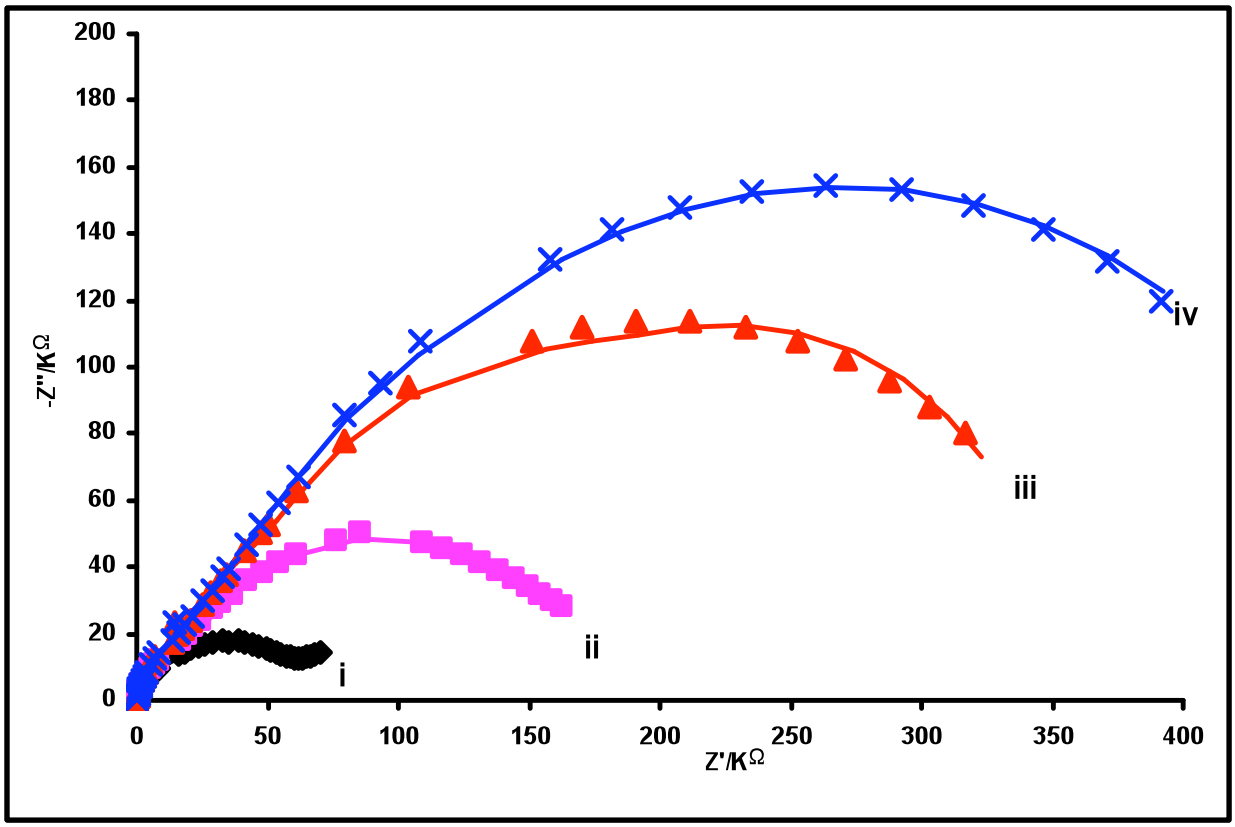

Figure 3.15: Typical serum concentration-dependent Nyquist plots of Au–MEODA–MA–SAP with HIV^+/TB^+ patient serum pre-incubated in empty liposomes. i, Au–MEODA–MA–SAP without HIV^+/TB^+ patient serum ii, 1 : 2000 (0.05% serum); iii, 1 : 1000 (0.10% serum) and iv, 1:500 (0.20% serum). The solid lines are fitted curves using equivalent circuits shown in Figure 3.13.

The impedance spectra for the HIV^-/TB^- patient serum (Fig 3.16) and its control experiments (not shown) showed diffusion of the redox probe demonstrated by the straight line at low frequencies (Zw)

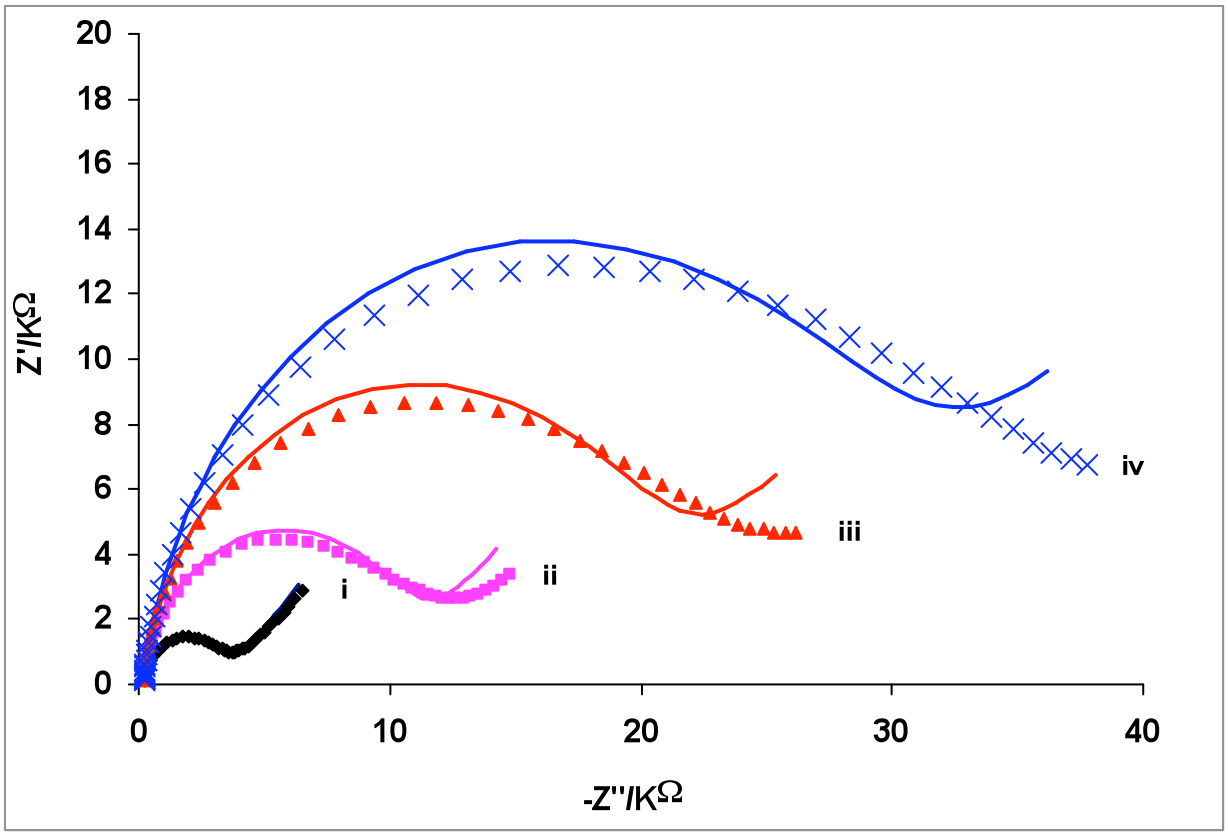

Figure 3.16: Typical serum concentration-dependent Nyquist plots of Au–MEODA–MA–SAP with HIV^-/TB^- patient serum pre-incubated in empty liposomes. i, Au–MEODA–MA–SAP without HIV^-/TB^- patient serum ii, 1 : 2000 (0.05% serum); iii, 1 : 1000 (0.10% serum) and iv, 1:500 (0.20% serum). The solid lines are fitted curves using equivalent circuits shown in Figure 3.7d.

The comparative results are represented as a bar chart for a range of serum dilutions (Figure 3.17). The change in the total charge transfer resistance ($\Delta R_{ct}/O$) for each concentration of the human sera was calculated from equation 3.10[32]:

$$\Delta R_{ct} = R_{Ag\text{-}Ab} - R_{Ag} \qquad 3.10$$

Where R_{Ag} is the electrode polarization resistance of the Au–MEODA–MA–SAP before incubation in the sera. This is easier understood from Scheme 3.3 of the modification of a Au–MEODA–MA electrode with a blocking agent (saponin, SAP) and subsequent interaction of the immobilized MA with anti-MA antibody in human TB-positive serum. $R_{Ag\text{-}Ab}$ is the value of the electrode polarization resistance after incubation of the Au–MEODA–MA–SAP in the liposome pre-incubated serum dilution.

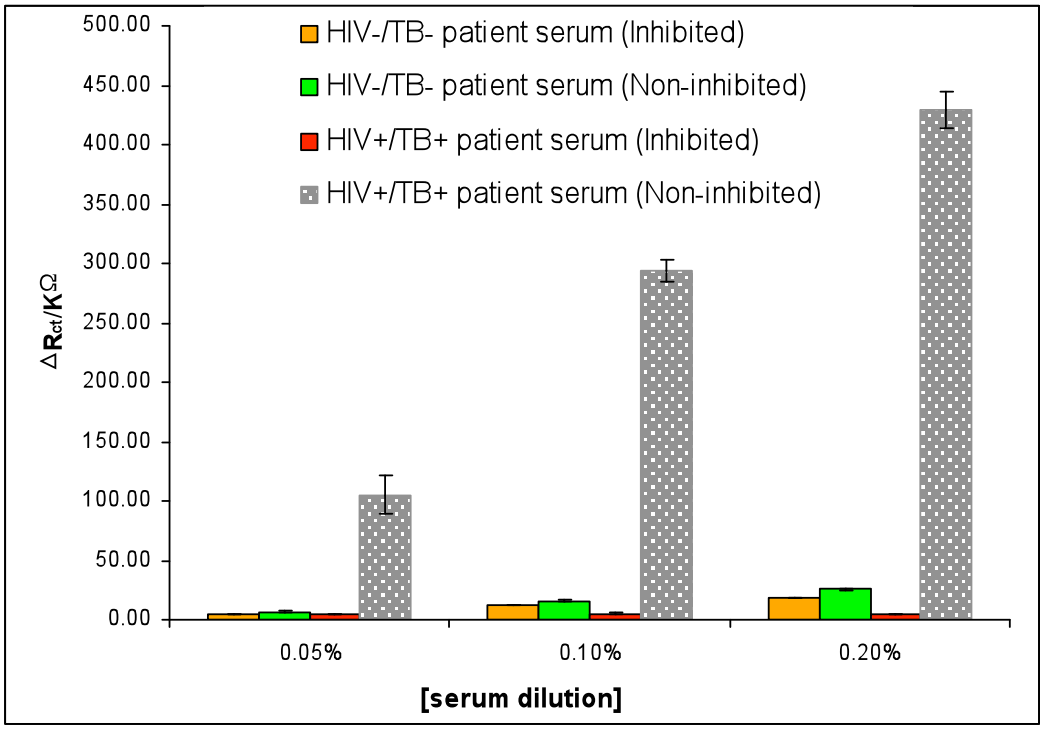

Figure 3.17: Comparative bar chart representation of the impedimetric detection signal obtained at the Au–MEODA–MA–SAP electrode for HIV+/TB+ and HIV-/TB- patient sera dilutions. 'Inhibited' means that the antibodies were inhibited from binding to the antigen on the electrode by pre-incubation of the serum with liposomes containing the MA antigen. 'Non-inhibited' means that the serum was pre-incubated with empty liposomes.

Remarkably, the change in electrode polarization resistances in HIV^+/TB^+ sera is approximately 10 times larger than that observed in the sera of the HIV^-/TB^- patient, proving that the electrode could satisfactorily discriminate between positive and negative TB sera.

3.7 References

1. G.E. Muilenberg (Ed.), Handbook of X-Ray Photoelectron Spectroscopy, Perkin-Elmer Corp., Eden Praire, Minnesota, 1979.
2. D. G. Castner, K. Hinds and D. W. Grainger, *Langmuir* 1996, 12,5083.
3. T. Hasegawa, J. Nishijo, M. Watanabe, *Langmuir* 2000, 16, 7325
4. T. Hasegawa, S. Amino, S. Kitamura, L. Matsumoto, S. Katada, J. Nisgijo, *Langmuir* 2003, 19, 105.
5. G. Sekanka, M. Baird, D. Minnikin, J. Grooten, *Expert. Opin. Therapeutic Patents* 2007, 17, 315.
6. C. Amatore, J.M. Saveant, D. Tessier, *J. Electroanal. Chem*. 1983, 147, 39.
7. T.J. Davies, R.G. Compton, *J. Electroanal. Chem*. 2005, 585, 63
8. T.J. Davies, C.E. Banks, R.G. Compton, *J. Solid State Electrochem*. 2005, 9, 797.
9. R. G. Compton, C.E. Banks, *Understanding Voltammetry*, World Scientific Publishing Co., Singapore, 2007.
10. X. Cui, D. Jiang, P. Diao, J. Li, R. Tong, X. Wang, *J. Electroanal. Chem*. 1999, 48, 243.
11. P. Diao, D. Jiang, X. Cui, D. Gu, R. Tng, B. Zhong, *J. Electroanal. Chem*. 1999, 464, 61.

12. T. Wilkop, D. Xu, Q. Cheng, *Langmuir* 2007,23, 1403-1409.
13. E. Sabatini, H.O. Finklea, *J. Phys. Chem*. 1987, 91, 6663.
14. H.O. Finklea, S. Avery, M. Lynch, T. Furtsch, *Langmuir* 1987, 3, 409.
15. K. Tokuda, T. Gueshi, H. Matsuda, *J. Electroanal. Chem*. 1971, 102, 41.
16. T.C. Girija, M.V. Sangaranarayanan, *J. Appl. Electrochem*. 2006, 36, 531.
17. M.E. Orazem, B. Tribollet, *Electrochemical Impedance Spectroscopy*; John Wiley & Sons Inc: Hoboken, NJ., 2008.
18. E. Barsoukov, J.R Macdonald (Eds), *Impedance Spectroscopy: Theory Experiment, and Applications*; 2nd ed.; Wiley: Hoboken, New Jersey, 2005; chapters 1 – 4.
19. J-Y. Park, Y-S. Lee, B. H. Kim, S-M. Park,, *Anal. Chem.* 2008, 80, 4986.
20. H.O. Finklea, S. Avery, M. Lynch, T. Furtsch, *Langmuir* 1987, 3, 409.
21. M.E. Orazem, B. Tribollet, *Electrochemical Impedance Spectroscopy*; John Wiley & Sons Inc: Hoboken, NJ., 2008; Chapter 13.
22. N. Bonanos, B.C.L. Steele, E.P. Butler, in: E. Barsoukov, J.R. Macdonald (Eds.), *Impedance Spectroscopy: Theory Experiment,*

and Applications; 2nd ed.; Wiley: Hoboken, New Jersey, 2005; chapter 4.

23. L.V. Protsailo, W.R. Fawcett, *Electrochim. Acta* 2000, 45, 3497.
24. H.O. Finklea, D.A. Snider, J. Fedyk, E. Sabatani, Y. Gafni, I. Rubinstein, *Langmuir* 1993, 9, 3660.
25. S. Campuzano, M. Pedrero, C. Montemayor, E. Fatas, J.M. Pingarron, *J. Electroanal. Chem*. 2006, 586, 112.
26. D. Garcia-Raya, R. Madueno, J. M. Sevilla, M Blazquez, T. Pineda, *Electrochim*. Acta 2008, 53, 8026.
27. R. G. Compton, C.E. Banks, *Understanding Voltammetry*, World Scientific Publishing Co., Singapore, 2007.
28. K. Tokuda, T. Gueshi, H. Matsuda, *J. Electroanal. Chem*. 1971, 102, 41.
29. H.O. Finklea, S. Avery, M. Lynch, T. Furtsch, *Langmuir* 1987, 3, 409.
30. P. Diao, M. Guo, R. Tong, *J. Electroanal. Chem*. 2001, 495, 98.
31. V. Marecek, Z. Samec, J. Weber*, J. Electroanal. Chem*. 1978, 94, 169.
32. R. Maalouf, C. Fournier-Wirth, J. Coste, H. Chebib, Y. Saı¨kali, O. Vittori, A. Errachid, J.-P. Cloarec, C. Martelet and N. Jaffrezic-Renault, *Anal. Chem*., 2007, 79, 4879.

Chapter 4: Conclusion and future perspectives

The integrity and properties of the mycolic acids integrated into N-(2-mercaptoethyl)octadecanamide (MEODA) monolayer have been evaluated and compared using X-ray photo-electron spectroscopy, atomic force microscopy, cyclic voltammetry and electrochemical impedance spectroscopy. Results showed that MA-modified gold substrate behaves as a microelectrode array which permits electron transport between a redox-active probe in solution and the underlying gold surface.

Three remarkable findings in the EIS study that should be emphasized are;

i. The MEODA and MA modified electrodes as well as the interaction between the immobilized MA and anti-MA antibody in TB positive serum typified the behaviour of micro-structural systems with grain/grain boundary phases.
ii. The immobilised MA and its anti-MA antibody interaction exhibited time-constant dispersion behaviour and
iii. The distribution of these time-constants occurred mainly along the area of the electrode (i.e., 2-D distributions arising from surface

heterogeneities such as the grain boundaries) with some contributions from the axis normal to the plane of the electrode surface (i.e., 3-D distribution (arising from porosity of the electrode).

These results confirm for the first time the ability of an impedimetric immunosensor to discriminate between a positive and a negative TB patient serum. It is noteworthy that a dilution of 1: 20 is the highest dilution where a significant binding to the antigens on the ELISA plates could be observed with most sera in ELISA by our groups. ELISA experiments were conducted with these two sera by Prof Verschoor's group at the 1: 20 dilution with a signal response ratio of HIV+–TB+ to HIV_–TB_ being 2: 1. It is interesting to observe that this impedimetric immunosensor could detect very low dilution (1: 2000) of antibodies in HIV+–TB+ sera, which suggests that this could probably be a very sensitive immunosensor for active TB.

The crucial physico-electrochemical insights into the behaviour of surface-confined MA, provided in this work, should form a useful basis for the design and development of potential impedimetric immunosensing platforms, not only for the investigated molecular species, but other molecules as well. This work has laid some foundation and opened up new questions to be further investigated. Such future studies should include the exploration of the impact of different immobilization strategies and organothiolate SAM species as viable hydrophobic supports for MA; impact of

different redox probes; employment of different human TB positive sera and controls; and applicability of cost-effective and easy-to-use disposable electrodes for monitoring progress in TB treatment, especially the drug-resistant TB. All these are now feasible and should be followed up in future investigation.

APPENDIX A; Publications in peer-reviewed journals that resulted from this Thesis

1. **Nsovo S. Mathebula,** Jeseelan Pillay, Gianna Toschi, Jan A. Verschoor and Kenneth I. Ozoemena, "Recognition of anti-mycolic acid antibody at self-assembled mycolic acid antigens on a gold electrode: a potential impedimetric immunosensing platform for active tuberculosis" *Chem. Commun*. 2009, 3345-3347.
2. Kenneth I. Ozoemena, **Nsovo S. Mathebula,** Jeseelan Pillay, Gianna Toschi, and Jan A. Verschoor, "Electron transfer dynamics across self-aasembled N-(2-mercaptoethyl) octadecanamide / mycolic acid layers: Impedimetric insights into the structural integrity and interaction with anti-mycolic acid antibodies" *Phys. Chem. Chem. Phys.* 2010, 12, 345.

APPENDIX B: List of conference presentations from this Thesis

1. "Mycolic acid antigen immobilisation for TB sero-diagnosis by biosensor". [1]**Samuel N. Mathebula**, [1]Kenneth I. Ozoemena, [1] Gianna Sekanka, [1] L. Pilcher and [2]Jan A. Verschoor, The South African TB conference – "Working as one": Hosted at the Durban International Convention Center; From 1-4 July 2008 (Oral presentation).

2. "Interrogating Self-Assembled Mycolic Acid Towards Impedimetric Immunodiagnosis of Tuberculosis". Kenneth I. Ozoemena**, Nsovo S. Mathebula**, and Jan A. Verschoor, Immunodiagnosis of Tuberculosis conference: Held in the United States of America, Virginia; From 21-24 September 2008 (Poster presentation).

APPENDIX C1: Multiplex X-ray photoelectron spectrum for the expanded C1s region.

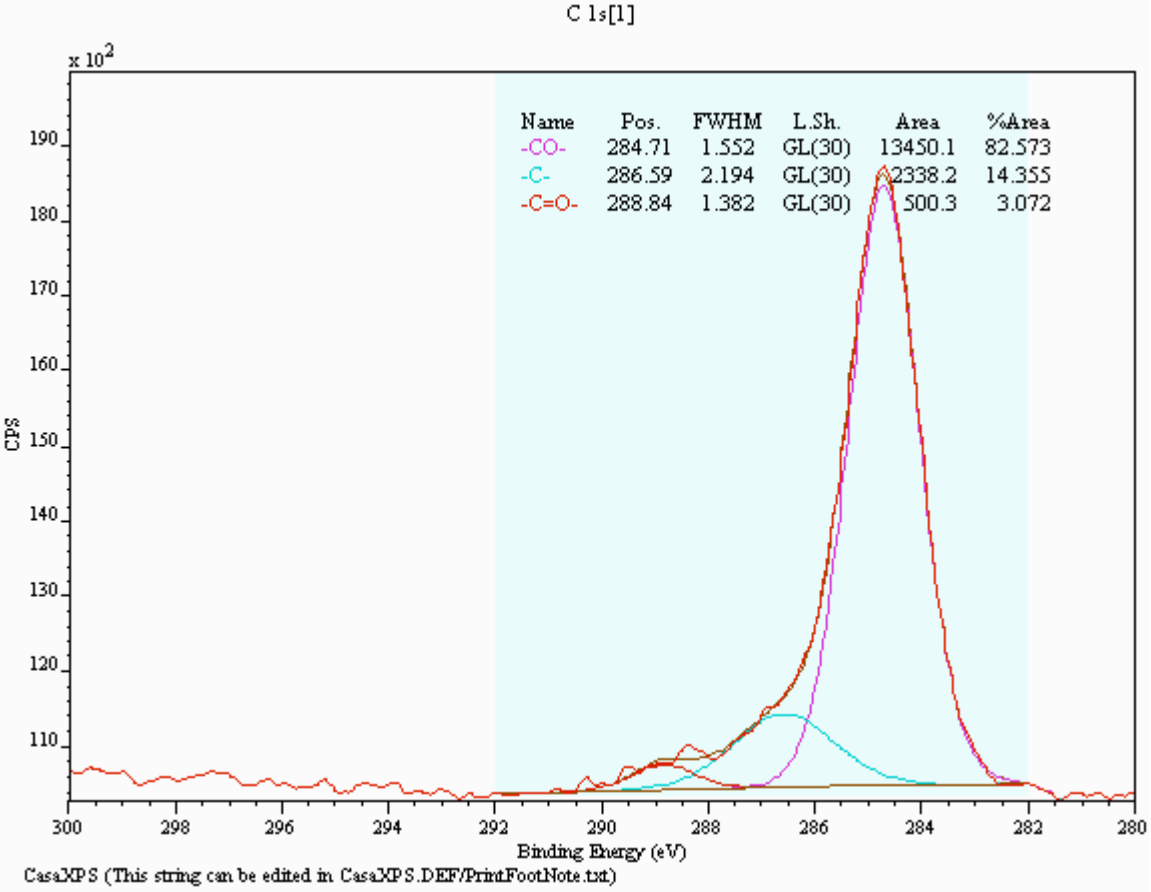

APPENDIX C2: Multiplex X-ray photoelectron spectrum for the expanded C1s region.